NASA Contractor Report 185217

Investigation of Advanced Counterrotation Blade Configuration Concepts for High Speed Turboprop Systems

Task 1 - Ducted Propfan Analysis
Final Report

Edward J. Hall, Robert A. Delaney, and James L. Bettner
Allison Gas Turbine Division of General Motors
Indianapolis, Indiana

April 1990

Prepared for
Lewis Research Center
Under Contract NAS3-25270

NASA
National Aeronautics and
Space Administration

Errata for NASA Contract NAS3-25270
Investigation of Advanced Counterrotation Blade Configuration Concepts for High Speed Turboprop Systems
Task1-Ducted Propfan Analysis
Final Report

Page 29: Second line from the bottom should read - ρ_{ref} is determined from the freestream total density

Page 78: Figure title should read - Axisymmetric plane projection of 160x41x15 H-grid for Kruger ....

Preface

This manual was prepared by E. J. Hall and R. A. Delaney of the Advanced Turbomachinery Department, Allison Gas Turbine Division, General Motors Corporation, Indianapolis, IN. The work was performed under NASA Contract NAS3-25270 from September, 1988 to January, 1990. The grid generation and flow code theory and programming modifications necessary for the analysis of ducted propfans were performed by E. J. Hall based on existing NASA software. The Allison program manager for this contract was J. L. Bettner.

Acknowledgements

The authors would like to express their appreciation to the following NASA personnel who contributed to this program:

M. Celestina, K. Curtley, and T. Beach for their helpful suggestions during the early phases of this program;

Dr. J. J. Adamczyk for the many helpful technical discussions concerning the development of the computer codes, and for providing the initial 3D Euler solver.

Dr. C. H. Miller and Dr. L. Bober for their suggestions and critical review of the program.

The services of the NASA Numerical Aerodynamic Simulation (NAS) facilities and personnel are gratefully acknowledged.

TABLE OF CONTENTS

LIST OF FIGURES

LIST OF TABLES

NOTATION

A list of the symbols used throughout this document and their definitions is provided below for convenience.

Roman Symbols

a ... speed of sound

c_p ... specific heat at constant pressure

c_v ... specific heat at constant volume

e ... internal energy

i ... z index of numerical solution

j ... r index of numerical solution

k ... θ index of numerical solution

n ... time step index of numerical solution or rotational speed (rpm)

$\vec{n}$ ... outward unit normal vector

p ... pressure

r ... radius or radial coordinate

t ... time

v ... velocity

z ... axial coordinate

A... surface area

C_p... pressure coefficient ($C_p = p - p_\infty / 2\rho_\infty u_\infty^2$)

C_p... power coefficient ($C_p = P/\rho n^3 D^5$)

C_t... thrust coefficient ($C_t = T/\rho n^2 D^4$)

CFL... Courant-Freidrichs-Levy

D... dissipation flux vector or diameter

$DELT$... adjacent cell grid spacing

$DELTLE$... adjacent cell grid spacing at leading edge

$DELTTE$... adjacent cell grid spacing at trailing edge

F... flux vector in z direction

G... flux vector in r direction

H... flux vector in θ direction

H_t... total enthalpy

J... advance ratio ($J = U/nD$)

K... source term flux vector

L... length

N... number of propeller blades

O... orthogonality

P... point distribution function or power

Q... vector of dependent variables

R... gas constant or residual or maximum radius

RAT... maximum ratio of adjacent cell grid spacings

S... arc length or pertaining to surface area normal

T... temperature or torque

U... flight velocity

V... volume

Greek Symbols

α... time-stepping factor

β... 3/4 radius propfan blade setting angle

ϵ^2... modified second-order damping coefficient

ϵ^4... modified fourth-order damping coefficient

ρ... density

κ^2... second order damping coefficient

κ^4... fourth order damping coefficient

γ... specific heat ratio

δ... spatial second-order central difference operator

λ... blockage factor

η... radial transformed variable for C-grid generation

ξ... axial transformed variable for C-grid generation

ν... damping factor

Υ... relative pressure gradient coefficient

Δ... increment of change

Special Symbols

∇... spatial vector gradient operator

$\triangle$... spatial forward difference operator

∇ ... spatial backward difference operator

Superscripts

$[\overline{\ }]$ ... averaged variable

$[\tilde{\ }]$ ... dimensional variable

$[\hat{\ }]$ ... implicitly smoothed variable

$[\vec{\ }]$ ... vector variable

$[\ ]^*$ ... intermediate variable

$[\ ]^n$ ... time step index of variable

Subscripts

$[\ ]_{i,j}$ ... grid point index of variable

$[\ ]_{max}$ ... maximum value

$[\ ]_{min}$ ... minimum value

$[\ ]_p$ ... related to pressure

$[\ ]_{ps}$ ... pressure (high pressure) surface

$[\ ]_{ss}$ ... suction (low pressure) surface

$[\ ]_t$ ... total quantity

$[\ ]_z$ ... derivative or value with respect to z

$[\ ]_r$ ... derivative or value with respect to r

$[\ ]_\theta$ ... derivative or value with respect to θ

$[\ ]_\infty$ ... freestream value

$[\ ]_{ref}$ ... reference value

1. SUMMARY

The time-dependent three-dimensional Euler equations of gas dynamics have been solved numerically to study the steady compressible transonic flow about ducted propfan propulsion systems. Aerodynamic calculations were based on a four-stage Runge-Kutta time-marching finite volume solution technique with added numerical dissipation. An implicit residual smoothing operator was used to aid convergence. Two calculation grids were employed in this study. The first grid utilized an H-type mesh network with a branch cut opening to represent the axisymmetric cowl. The second grid utilized a multiple-block mesh system with a C-type grid about the cowl. The individual blocks were numerically coupled in the Euler solver. Grid systems were generated by a combined algebraic/elliptic algorithm developed specifically for ducted propfans. Numerical calculations were initially performed for unducted propfans to verify the accuracy of the three-dimensional Euler formulation. The Euler analyses were then applied for the calculation of ducted propfan flows, and predicted results were compared with experimental data for two cases. The three-dimensional Euler analyses displayed exceptional accuracy, although certain parameters were observed to be very sensitive to geometric deflections. Both solution schemes were found to be very robust and demonstrated nearly equal efficiency and accuracy, although it was observed that the multiple-block C-grid formulation provided somewhat better

resolution of the cowl leading edge region.

2. INTRODUCTION

Modern turbopropeller (propfan) aircraft propulsion systems have demonstrated the potential for significant fuel savings over existing high bypass turbofan engines. By incorporating innovative airfoil design concepts utilizing a high degree of blade lean, sweep, and twist, propfans can perform effectively at relative Mach numbers extending well into the transonic regime. A number of aerodynamic phenomena common in propfan installations are illustrated on Fig. 2.1. The process of designing advanced propfans requires a complicated iterative interaction between the disciplines of aerodynamics, structural analysis, and aeroacoustics. Reliable attainment of performance goals necessitates the use of proven aerodynamic analyses for the highly three-dimensional blades. In this respect, the realization of the performance improvements available in advanced propfan designs is directly related to advances in computational fluid dynamics.

Several researchers have recently published advanced numerical analyses for propfan flows. Barton et al. [1] and Usab et al. [2] presented results from several three-dimensional Euler codes for single-rotation propellers which were verified through comparison with experimental data. Celestina et al. [3] performed a time-averaged solution of three-dimensional counter-rotating propeller flowfields using an average-passage system of equations. Whitfield et al. [4] performed calculations for unsteady

three-dimensional single-rotation and counter-rotation propfans using a multiple-block grid formulation. Saito et al. [5], Matsuo et al. [6], and Kobayawa and Hatano [7] have all demonstrated the application of the three-dimensional Navier-Stokes equations for the analysis of high speed propfan designs. Many of the aerodynamic features relevant to propfan flowfields have been successfully captured by these and other analyses, including blade leading edge and tip vortices, transonic/shock flow phenomena, and counter-rotating blade row unsteady interaction.

In light of the desire to optimize propfan designs, the concept of a ducted propfan configuration (very high bypass fan, see Fig. 2.2) has recently been explored. By ducting the propulsor, a significant increase in thrust and efficiency can be obtained, particularly at static, or low forward flight velocities. This thrust improvement could significantly impact future designs by permitting reduced diameters and underwing installation. Ducted propellers may also have advantages related to community noise levels and enhanced public acceptance. The concept of a ducted propeller has existed for more than fifty years, although research was initially directed at low-speed applications due to the drag penalty associated with the cowl at higher flight velocities. Early tests of ducted propellers are given in a review by Sacks and Burnell [8]. A more recent discussion on the technical issues relating to ducted propfans was given by Groeneweg and Bober [9]. In order to assess the relative aerodynamic merits of advanced ducted propfan design configurations, detailed computational analyses similar to those described above for unducted propulsors are required.

This document contains the Final Report and User's Manual for the 3D Euler Ducted Propfan Analysis codes developed by the Allison Gas Turbine Division

PROPFAN AERODYNAMIC CHARACTERISTICS

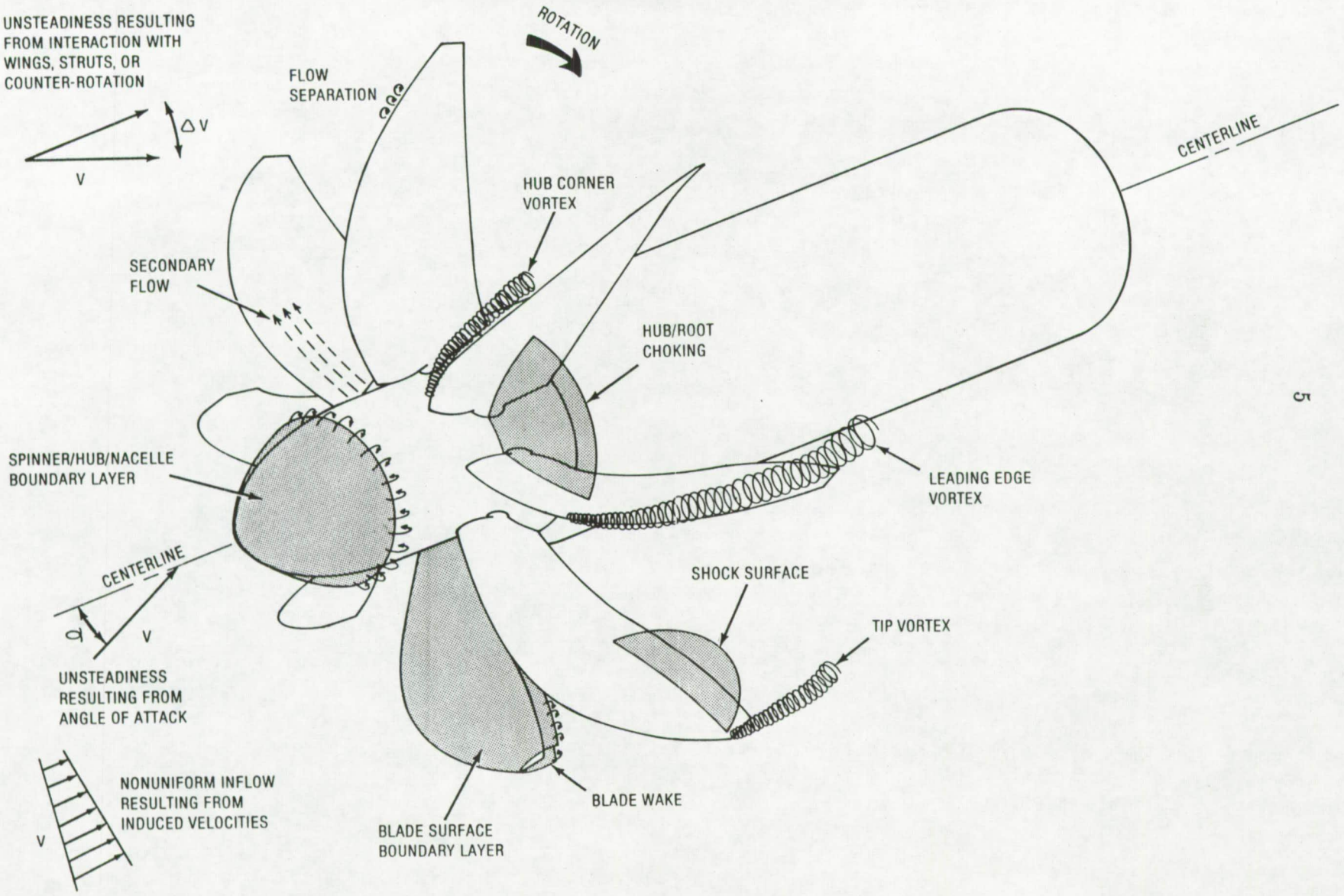

Figure 2.1: Propfan aerodynamic characteristics

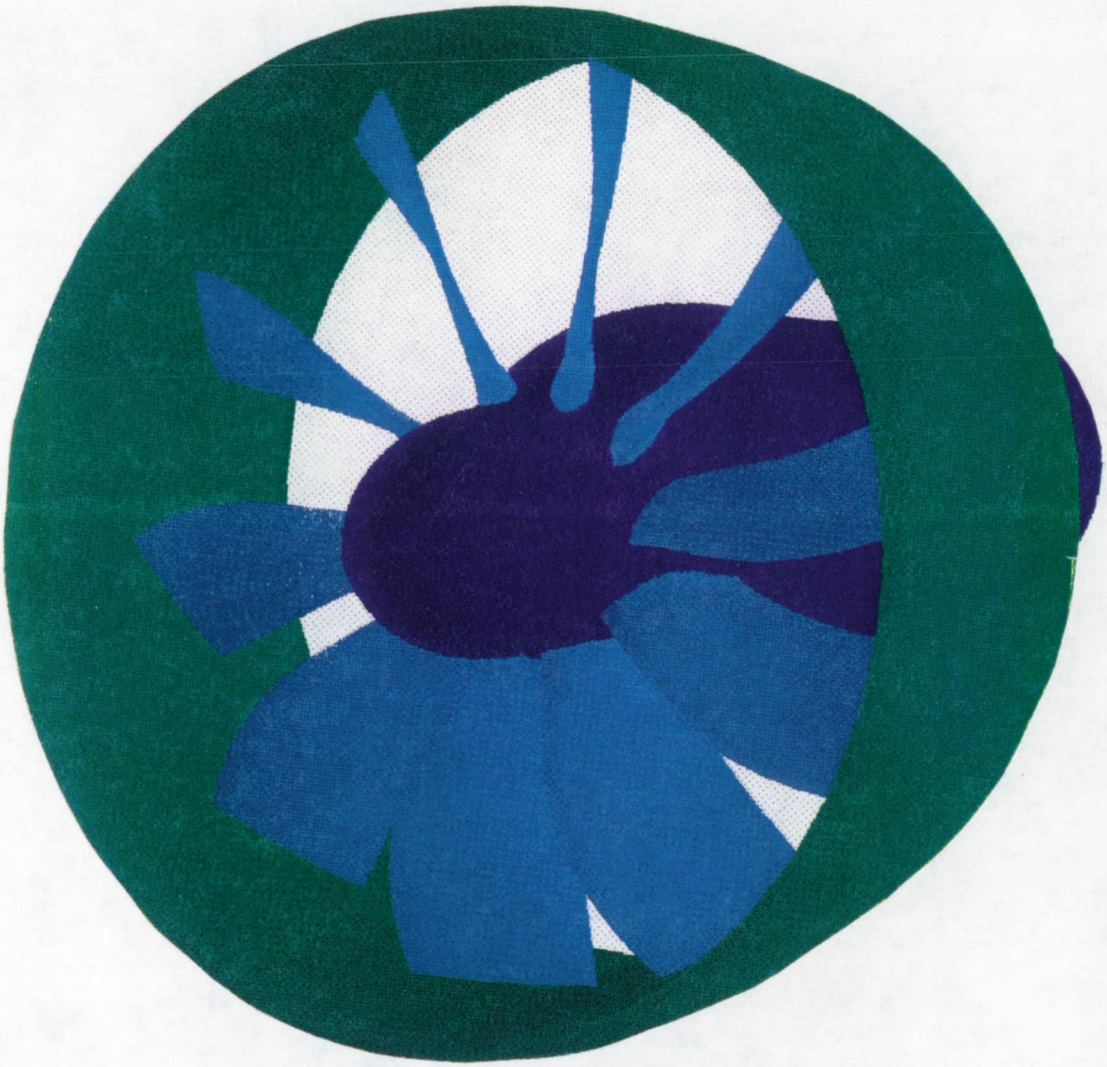

Figure 2.2: Ducted propfan (very high bypass fan) geometry

of the General Motors Corporation under Task 1 of NASA Contract NAS3-25270. This study was directed at the development of a three-dimensional Euler analysis for high-speed ducted propfans. A finite volume multiple-block four-stage Runge-Kutta numerical algorithm was utilized to predict the aerodynamics of ducted fan flows. Of particular interest was the ability to accurately predict the aerodynamics of the cowl. Two different grid arrangements were tested. The first system involved a sheared H-type grid which utilized a branch cut opening for the cowl. The second system was based on a numerically coupled multiple-block grid arrangement with a body-centered C-type grid about the cowl. Predicted results using both grid systems were compared with experimental data for two cases: a single-rotation low speed ducted propeller, and a high-speed 1.15 pressure ratio fan (both single-rotation and counter-rotation arrangements). This program is considered the initial step in developing a complete aerodynamic model of the flowfield through a ducted fan and the external flow over the engine nacelle and fan cowl.

To predict the flow about a ducted propfan using the analyses described in this document, the necessary sequence is:

1. Generate a numerical grid for the domain of interest.

2. Run the Euler code to predict the steady aerodynamics.

3. Process the results as needed.

Separate sections are provided in the chapters which follow to describe the basis and operation of the codes used in the first two steps. A theoretical development of the grid generation algorithms for both the H-grid and C-grid architectures is given in

Chapter 2. The 3D time-marching Euler analysis is detailed in Chapter 3. In Chapter 4, a summary of the predicted results and verification studies performed to validate the accuracy of the analysis is presented. A summary of the conclusion of this study is given in Chapter 5. A user's manual for the grid generation code is provided in Appendix A. The operation of both the H-grid and multiple-block C-grid 3D Euler computer codes is outlined in Appendix B.

It is worthwhile mentioning that most of the plotting and graphical postprocessing of the solutions are performed on graphics workstations. Presently, the PLOT3D [10] graphics software developed at NASA Ames Research Center is being extensively used for this purpose, and plot output has been tailored for this software.

3. GRID GENERATION ALGORITHM

In this chapter, the numerical algorithm forming the basis of the ducted propfan analysis grid generation schemes is described. The geometry and computational domain are briefly described in the first section below. During the course of this study, two types of grids were tested for the numerical calculations. The grid systems are divided into two categories: H-grid, and multiple-block C-grid. Separate sections are provided to describe each category.

3.1 Computational Domain

The problem of interest is a ducted propfan geometry in steady operation as shown in Fig 2.2. Geometric parameters are expressed in a cylindrical coordinate system. The axial coordinate lies along the propeller axis of rotation, the radial coordinate is perpendicular to the axis of rotation, and the circumferential coordinate sweeps in the counter-clockwise direction when viewed down the axis of rotation. This coordinate system is illustrated in Fig. 3.1. The hub and duct contours are assumed to be axisymmetric surfaces (no circumferential variation). It is further assumed that the airfoil tips are fully enclosed within the duct (although this limitation could be easily relaxed). For any number of blades, under the assumptions of steady flow and

a periodic geometry, the computational domain may be reduced to a single blade passage, circumferentially, as shown in Fig. 3.1. For counter-rotating configurations, a single blade passage is used for each blade row, and the multiple passages are then numerically coupled in the flow solver. The problem is further simplified by fixing the computational domain to the rotating blade elements. The resulting flow predictions are therefore based on the steady flow relative to the rotating blade.

In order to implement a finite volume numerical solution of the steady aerodynamics for this computational domain, the region of interest must be subdivided into a finite number of smaller elements within the overall region of interest. To enhance the quality of the numerical solution, we further specify that these subdivisions be constructed in a relatively smooth and orderly manner with some arbitrary limitation on both the relative spacing between cells and the total number of cells in the computational domain. Each of these subdivisions will be used to define an elemental computational cell which will form the geometric basis of the finite volume aerodynamic solver to be described in a later chapter.

In this study, two methods for constructing the computational cells were developed. The first method, referred to as the H-grid, is based on a single-block array of computational cells ordered in an H-type fashion. The second method, referred to as the multiple-block C-grid, utilizes a coupled system of five blocks each containing an array of computational cells. The five-block system is constructed by first subdividing the overall computational domain into five subregions, then further subdividing the individual subregions. The multiple-block arrangement permits the use of a special C-type grid wrapped about the leading edge of the duct to enhance the accuracy of

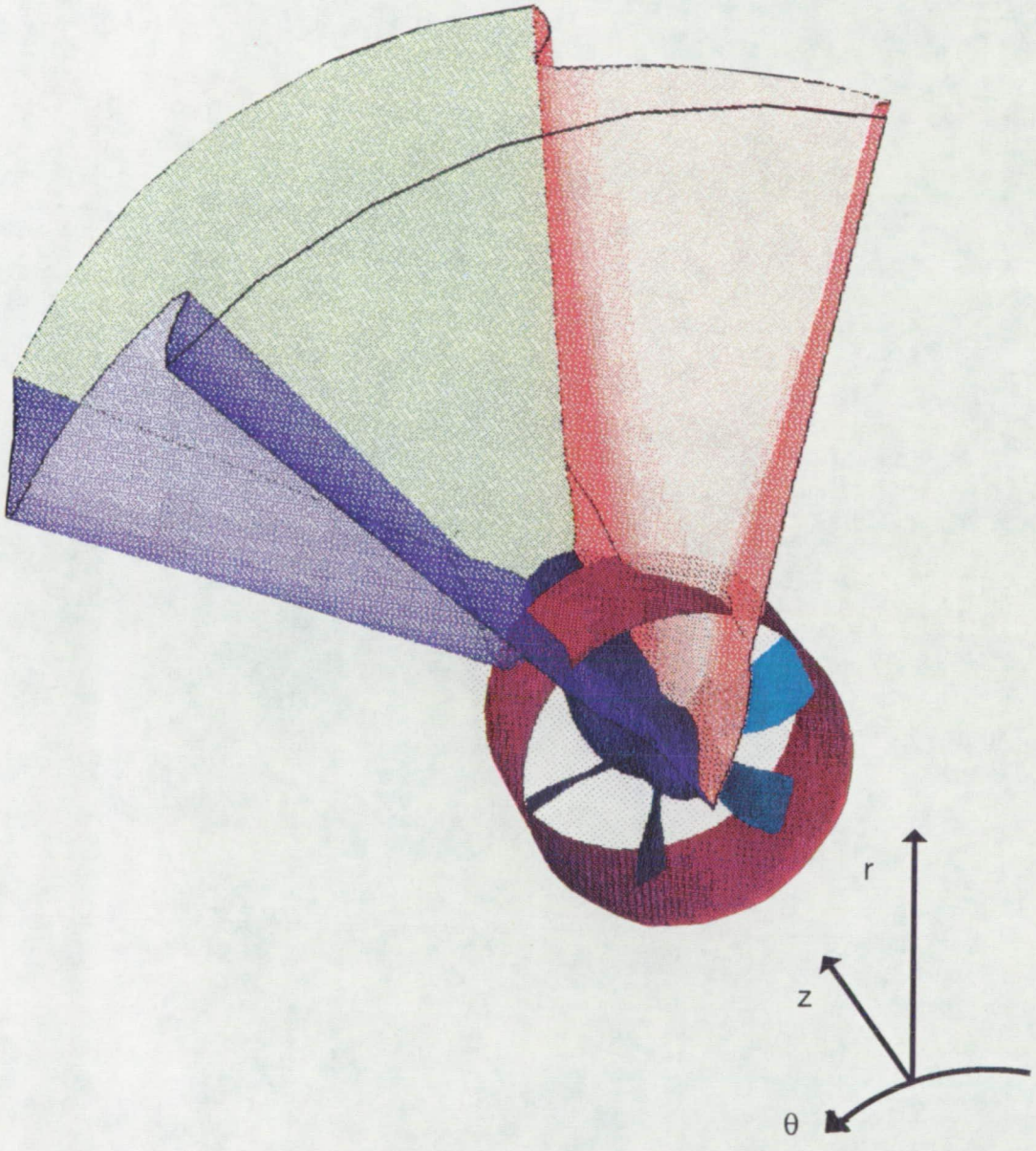

Figure 3.1: Ducted propfan analysis computational domain

the aerodynamic calculations in this critical region.

Both the H-grid and C-grid algorithms are described in the sections below.

3.2 H-Grid Algorithm

The H-grid generation scheme is based on a procedure originally developed by Mulac [11] for multiple blade row flow calculations using the average-passage [12] system of equations. In solving the average-passage system of equations, it is a requirement that the individual blade row grids have identical axisymmetric projections. This same technique was also applied in this study. The grid generation technique applies equally to single-rotation or multiple-rotation geometries. The approach here is to first construct a two-dimensional axisymmetric mesh in the z, r plane, followed by separate constructions for each of the individual blade rows in the circumferential direction to determine the final three-dimensional meshes.

The two-dimensional meshes are constructed by dividing the axisymmetric plane into several subregions as shown in Fig. 3.2 for an unducted propfan and Fig. 3.3 for a ducted propfan. The regions of interest include the inlet, mid-inlet, blade, mid-exit, exit, between blade, tip gap, and outer flow regions. The mid-inlet and mid-exit regions result from the assumption that the blade leading and trailing edges are fully contained within the axial span of the duct. These regions are individually gridded in the two-dimensional plane to satisfy the conditions of common grid points along region interface boundaries, and a suitable distribution of points within each region.

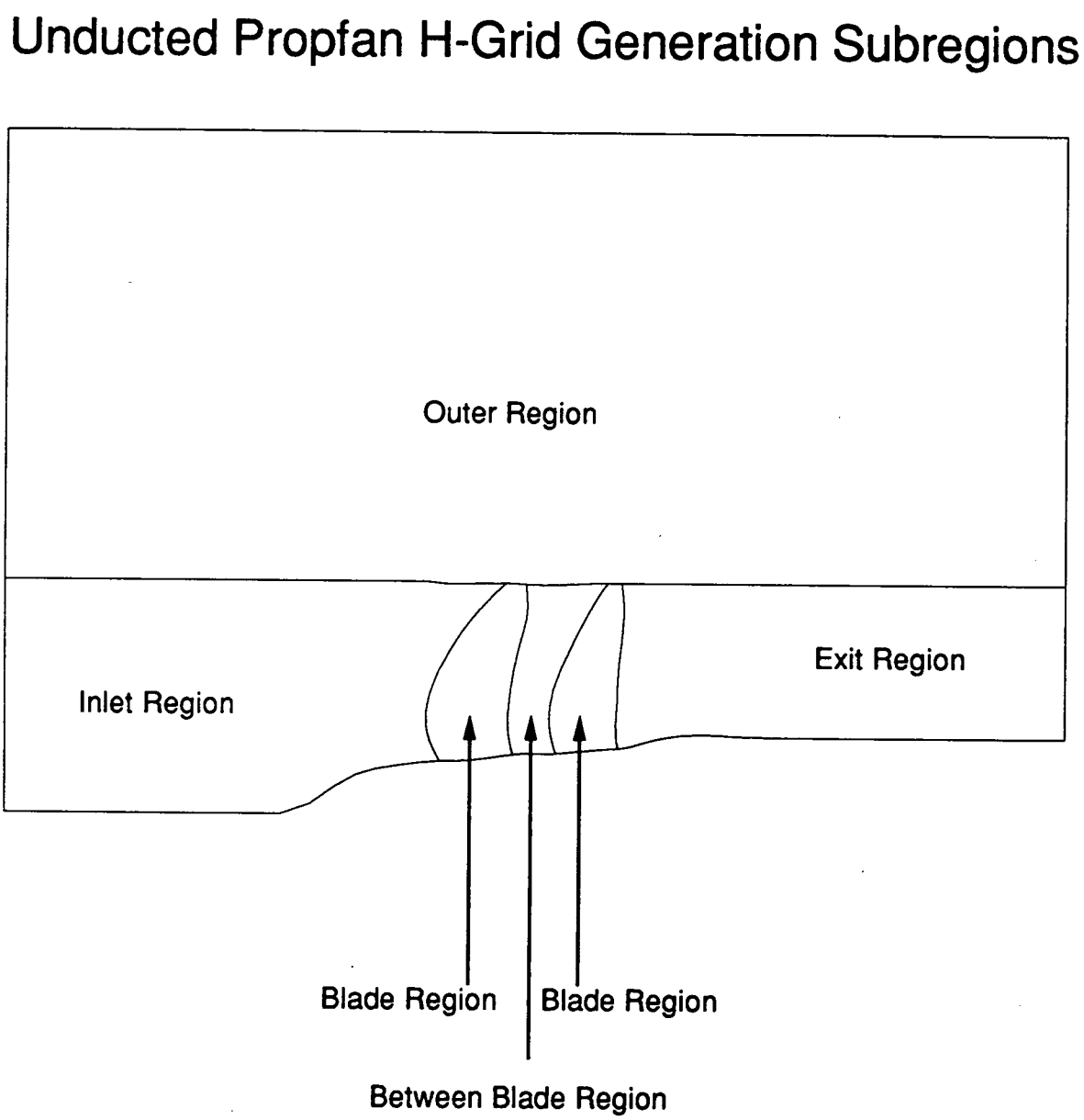

Figure 3.2: Axisymmetric plane projection grid generation subregions for an unducted propeller

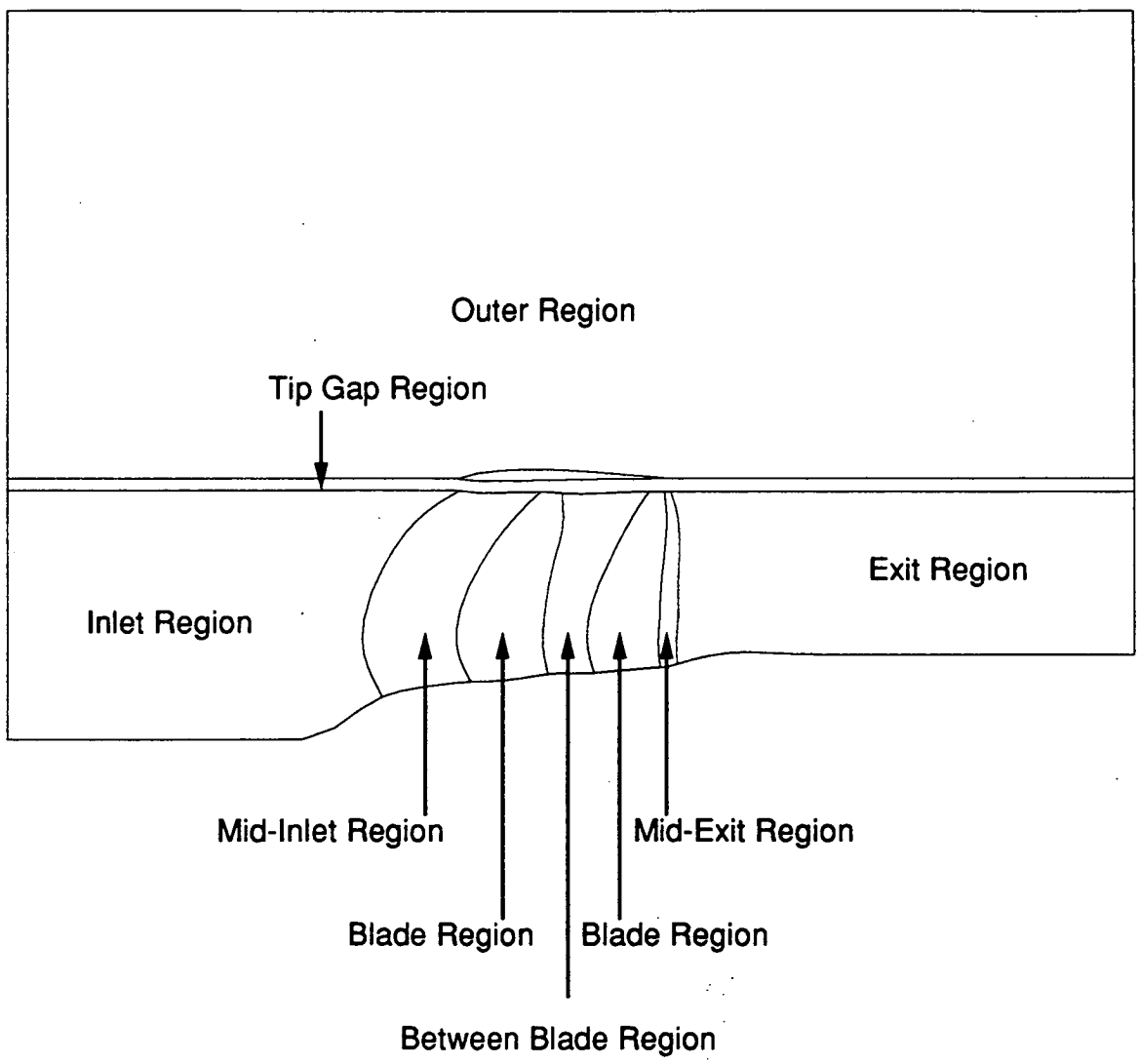

Figure 3.3: Axisymmetric plane projection grid generation subregions for a ducted propeller

The various regions differed in their individual construction. The distribution of points in any region is given axially and radially by one of three point distribution routines. These routines are described in the paragraphs below. All interpolations of coordinates were performed using a cubic spline interpolation routine.

The distribution of the points on the axisymmetric blade plane in both the radial and axial direction is determined by a simple geometric progression radiating from a symmetric centerline referred to as packing algorithm #1 described below.

Packing algorithm #1

Given:

D total projected length of cubic spline curve

RAT maximum ratio of adjacent cell projected lengths

M number of points distributed across D (must be odd)

the initial cell length of the progression is calculated as

$$DELT = \frac{\frac{D}{2}}{\sum_{i=1}^{(M/2)+1}(RAT)^i} \tag{3.1}$$

The point distribution is then given by

$$P(i) = \sum_{j=1}^{i}(DELT)(RAT)^j; \quad i = 1,(M/2)+1 \tag{3.2}$$

Packing algorithm #2

The second construction utilizes a slightly different packing algorithm. In this case, D, RAT, and $DELT$ are specified along with N, the total number of parallel

spline curves, leaving M to be determined. The value of M is calculated iteratively until the the following conditions are satisfied:

$$\left(\frac{D}{DELT}\right)_{max} = \sum_{i=1}^{M} (RAT)^i$$

$$\left(\frac{D}{DELT}\right)_{min} = \sum_{i=1}^{M} (RAT)^{-i}$$

where

$$\left(\frac{D}{DELT}\right)_{max} = max\left(\frac{D}{DELT}\right)_{j=1,N}$$

$$\left(\frac{D}{DELT}\right)_{min} = min\left(\frac{D}{DELT}\right)_{j=1,N} \tag{3.3}$$

These conditions guarantee that neither the adjacent cell ratios, nor their inverses, exceed RAT. The resulting point distribution is then given by

$$P(i) = \sum_{j=1}^{i} (DELT)(RAT)^j, i = 1, M \tag{3.4}$$

This approach is used axially in the inlet and exit regions, and radially in the outer boundary region.

Packing algorithm #3

The third packing algorithm is used to determine the axial point distribution between blade rows.

Given:

D total projected length of cubic spline curve

RAT maximum ratio of adjacent cell projected lengths

$DELTTE$ initial cell width (forward blade row trailing edge)

$DELTLE$ initial cell width (aft blade row leading edge)

N total number of parallel cubic spline curves

the following values are then calculated:

$$DTE = \left(\frac{DELTTE}{DELTTE + DELTLE}\right)(D) \tag{3.5}$$

$$DLE = \left(\frac{DELTLE}{DELTTE + DELTLE}\right)(D) \tag{3.6}$$

The value of M is determined iteratively until the following conditions are satisfied:

$$\left(\frac{D}{DELT}\right)_{max} \leq \sum_{i=1}^{M} RAT^{i} \tag{3.7}$$

$$\left(\frac{D}{DELT}\right)_{min} \leq \sum_{i=1}^{M} RAT^{-i} \tag{3.8}$$

where:

$$\left(\frac{D}{DELT}\right)_{max} = max\left(\frac{DTE}{DELTTE}\right)\left(\frac{DLE}{DELTLE}\right), j = 1, N \tag{3.9}$$

$$\left(\frac{D}{DELT}\right)_{min} = min\left(\frac{DTE}{DELTTE}\right)\left(\frac{DLE}{DELTLE}\right), j = 1, N \tag{3.10}$$

Again, this ensures that neither the adjacent cell ratios, nor their inverses exceed RAT. The point distribution is then given by:

$$P(i) = \sum_{j=1}^{i} (DELTTE)(RAT)^{j}, \quad i = 1, M \tag{3.11}$$

$$P(i) = \sum_{j=1}^{i} (DELTLE)(RAT)^{j}, \quad i = 1, M \tag{3.12}$$

The blade region is generated initially. This region is defined by the axisymmetric projection of the blade hub and tip boundaries, and the blade leading and trailing edges. The number of points defining the blade region axially and radially is specified.

The point distributions are determined by packing algorithm #1. Once the blade points are determined, the full inlet region pictured in Fig. 3.2 is computed next using packing algorithm #2, regardless of whether a ducted or unducted configuration is being generated. Once this region has been discretized, a simple linear interpolation is performed to determine the coordinates of the radial grid line which exactly intersects the duct leading edge. This grid line then determines the boundary between the mid-inlet region and the inlet region in Fig. 3.3. Once this boundary is determined, the upper boundary of the mid-inlet region is constructed by extrapolating the blade tip grid line axially, and maintaining the known tip gap spacing. Packing algorithm #1 is then used to distribute points axially in exactly the same manner in the mid-inlet region as the blade region, with the additional constraint that the grid lines must match at the region interface. Once this region is constructed, the inlet region can be constructed using packing algorithm #2. The point distributions for additional blade rows (if necessary) are then determined using packing algorithm #1. For multiple blade rows, the next step is to calculate the region between blades using packing algorithm #3. The mid-exit and exit regions are constructed in the same manner as the mid-inlet and inlet regions by locating the grid line which exactly intersects the cowl trailing edge. The tip gap region is constructed algebraically with a specified number of equally spaced points in the radial direction between the blade tip grid line and the cowl lower surface. Upstream and downstream of the cowl, the cowl surface grid line is extended axially from the leading and trailing edges. It should be noted that this may impose some limitation on the maximum diameter of the hub upstream and downstream of the cowl. Finally, the radial distribution of points in

the outer region is determined from packing algorithm #2. The grid lines which form the upper and lower surface of the cowl overlap upstream and downstream of the cowl. A duplicate grid line is placed on top of the cowl lower surface grid line to provide a natural storage location for the phantom points used in the application of the cowl surface boundary conditions (see Section 4.6). Once the axisymmetric plane grid has been calculated, the full three-dimensional grid is constructed individually for each blade row. The blade twist and thickness distributions are used to determine the circumferential coordinates for the blade regions. The remaining circumferential coordinates are based on utilizing packing algorithm #1 in the blade-to-blade plane. The circumferential variation of grid points upstream and downstream of the blade regions is adjusted to provide a smooth transition such that the grid lines become parallel to the axis of rotation away from the blade region.

A sample H-grid for a ducted propfan based on this grid generation technique is given in Fig. 3.4. The tip gap has been enlarged for this geometry in order to illustrate the tip gap grid. The emphasis in this development, as in Mulac [11], was to maintain a reasonable grid quality, rather than a specific number of grid points. Due to the algebraic nature of the scheme, the construction is performed relatively easily and inexpensively. Unfortunately, this approach can have drawbacks under certain conditions. The cubic spline interpolation routine is subject to errors when a boundary or grid line has a discontinuous or sudden change in slope (particularly troublesome spots are the spinner or cowl leading edges). In addition, blades or cowls with a large thickness or blunt leading edge may not be well represented by this scheme when a relatively low number of grid points is used. Finally, the construction

may occasionally have limits based on the number of grid points in a particular region due to the inability to satisfy one or more of the adjacent cell ratio constraints in the packing algorithms.

3.3 C-Grid Algorithm

The C-grid generation scheme utilizes a number of concepts developed for the H-grid scheme. Again, the mesh is generated by first constructing a two-dimensional grid in the axisymmetric plane. In this case, a slightly different subdivision approach is utilized. The individual subregions and the five-block structure for the C-grid approach are listed and displayed in Fig. 3.5. Several of the subdomains are similar to those used in the H-grid construction, so the extension of the algorithm to the C-grid is obvious. In the case of the H-grid, the individual subregions are eventually combined into a single grid for use with the 3D H-grid Euler analysis. In the multiple-block C-grid generation, the subdomains are left divided and the individual flow solutions are numerically coupled. The blade, mid-inlet, inlet, mid-exit, exit, and outer regions are all constructed in basically the same manner for the C-grid as they were for the H-grid. In this case, the axial locations of the upstream boundary of the mid-inlet and the downstream boundary of the mid-exit regions are specified as a fraction of the cowl axial chord upstream and downstream of the cowl leading and trailing edges, respectively. The tip gap is extended upstream and downstream of the cowl, so there are no overlapping grid lines (resulting in the need for blocks 2 and 4), and the outer boundary extends radially from a grid line which is displaced from the cowl outer surface by a distance equal to the inner surface tip gap spacing. The near-

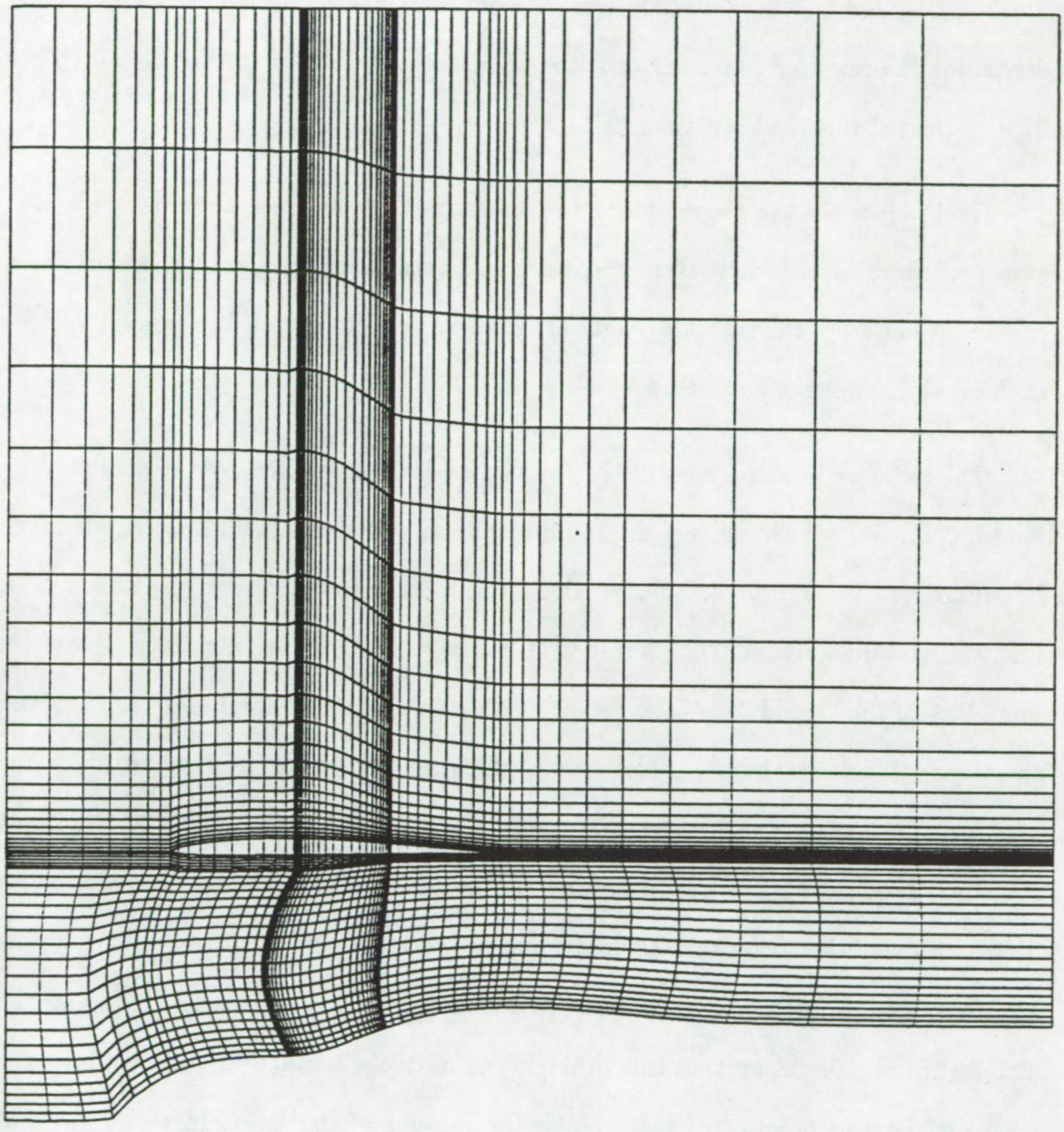

Figure 3.4: Sample H-grid for a ducted propfan

cowl region is then discretized by the C-grid as shown in Fig. 3.5. The construction of blocks 1,2,4, and 5 follows directly from the development of the H-grid, so no further discussion is presented here. Instead, the underlying algorithm for the C-grid (block 3) is presented in the paragraphs below.

Grid points for the C-grid block surrounding the cowl are determined in a two-step procedure. In the first step, the inner and outer boundary points are specified. In the second step, the interior points are determined. Each step has several options each of which is described below.

The exterior boundary points of the C-grid are determined by the surrounding four blocks. This is based on the requirement of coincident points along all block boundaries. The number of points along the inlet plane is directly specified, and must be an odd number. The number of points from the cowl surface to the outer boundary of the C-grid must also be specified, which fixes the number of points along the C-grid block exit plane. The cowl surface points are determined through one of two procedures. The first method performs a simple interpolation of the input coordinates based on arc length around the airfoil such that the relative arc length distributions of the airfoil surface points and the corresponding outer boundary points are the same. Unfortunately, this can often lead to highly skewed mesh lines near the airfoil surface. To circumvent this problem, an option was provided which allows the cowl surface grid points to "float" along the contour of the airfoil in a manner that would impose orthogonality at the cowl surface from a line extending from the cowl point to the corresponding outer boundary point. The movement of the airfoil grid points is controlled by a secant iteration procedure which optimizes the orthogonality

Ducted Propfan Multiple-Block C-Grid Subregions

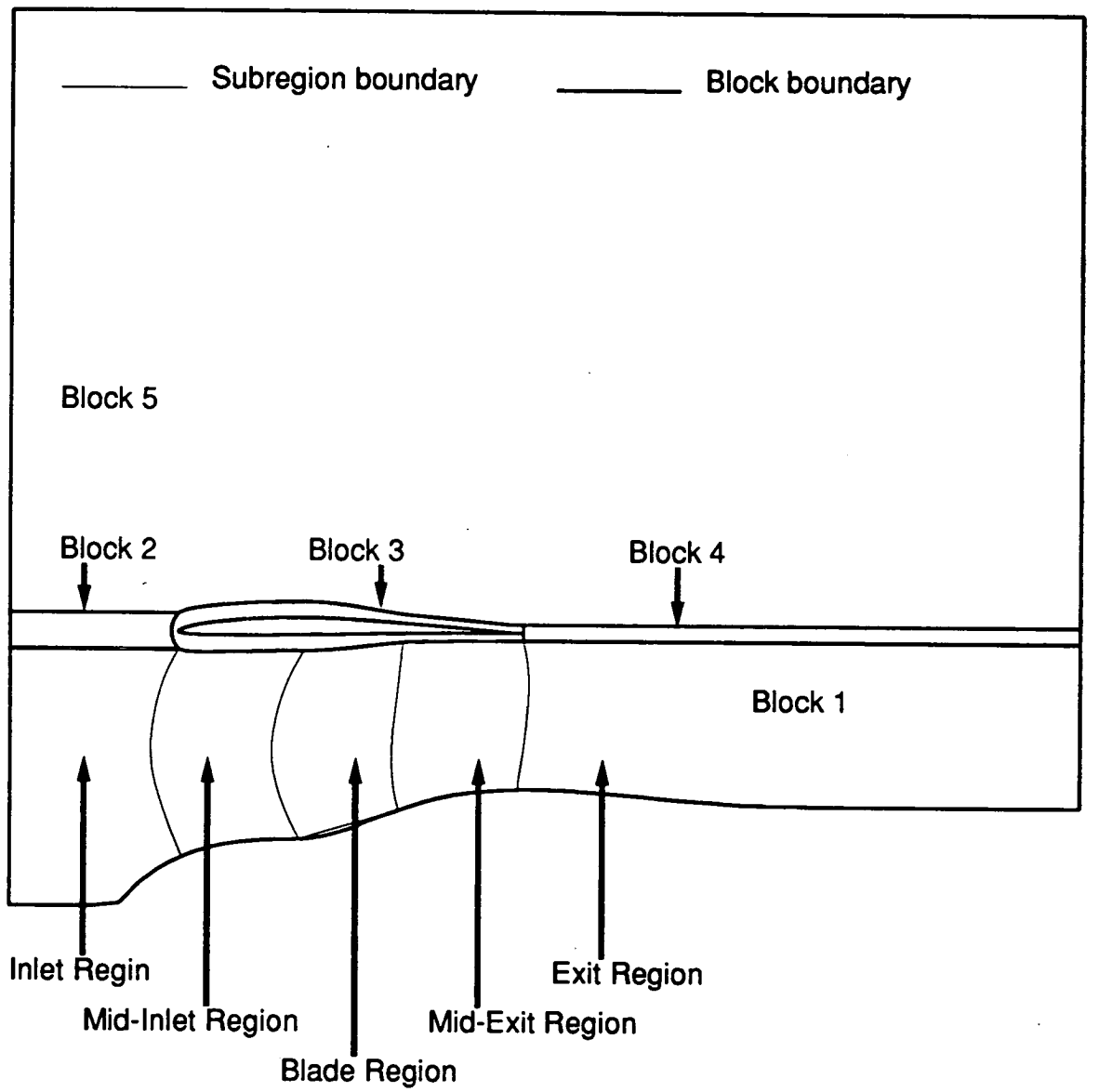

Figure 3.5: Axisymmetric plane projection subregions for multiple-block C-grid generation

of the surface grid point location as a function of arc length along the airfoil while maintaining a smooth transition through neighboring surface grid points. The new airfoil coordinates are determined from the updated value of arc length through a linear interpolation of the arc length and airfoil coordinates originally specified. The resulting grid thus possesses more desirable orthogonality characteristics along the airfoil contour, which is desirable in terms of solution accuracy.

The secant iteration procedure described above for the cowl surface grid points is expressed as:

$$S_i^{k+1} = S_i^k + \frac{(0.0 - O_i^k)(S_i^k - S_i^{k-1})}{(O_i^k - O_i^{k-1})} \tag{3.13}$$

where S_i is arc length measured clockwise around the cowl from a fixed reference location (1) to the point (i), k is the secant iteration count, and O_i is the measure of nonorthogonality. The orthogonality measure was based on the change of arc length S_{grid} between the outer point and the corresponding inner point. The optimized point occurs when $O_i = dS_{grid}/dS^k = 0$.

The starting values for the secant iteration are determined by using an initial point distribution obtained from the relative arc length cowl surface grid point interpolation routine (method one, above).

In order to avoid overlapping grid lines and to maintain stability, the new surface grid point locations were never allowed to migrate more than one third of the distance between the previous surface location and that of the neighboring grid points.

Interior grid points are determined through one of two methods. The first method is a simple algebraic interpolation of coordinates between the inner and outer C-grid boundary point distributions. In the second method, the interior points are generated

through the numerical solution of a set of elliptic equations controlling a weighted distribution of grid smoothness, orthogonality, and grid point density based on a variational formulation originally developed by Brackbill and Saltzman [13]. A brief description of this scheme is given below.

For a two-dimensional grid, the following integral expressions may be derived to evaluate critical aspects of the overall grid quality in physical space:

Grid smoothness:

$$I_s = \int\int [(\nabla\xi)^2 + (\nabla\eta)^2] dzdr \tag{3.14}$$

Grid orthogonality:

$$I_o = \int\int [(\nabla\xi)\cdot(\nabla\eta)] dzdr \tag{3.15}$$

Grid point density:

$$I_w = \int\int w(z,r) J dzdr \tag{3.16}$$

where:

$$\xi = \xi(z,r) \quad \eta = \eta(z,r) \tag{3.17}$$

$$J = \frac{\partial(\xi,\eta)}{\partial(z,r)} \tag{3.18}$$

and where ∇ is the Cartesian gradient vector operator. The term $w(z,r)$ is a user-specified function the magnitude of which is proportional to the desired grid point density in physical space.

Obviously, the smoothest possible grid is obtained when I_s is minimized, the most orthogonal grid is obtained when I_o is minimized, and the grid with the most desirable point density is obtained when I_w is minimized. By minimizing a weighted sum of these terms, i.e:

$$I = I_s + C_o I_o + C_w I_w \tag{3.19}$$

the constants C_o, C_w may be used to control the relative importance of orthogonality and point density, respectively, in the overall grid point distribution. By exchanging dependent and independent variables, and applying the concepts of variational calculus for minimizing functions using the Euler-Lagrange equations, the following nonlinear coupled set of equations results:

$$b_1 z_{\xi\xi} + b_2 z_{\xi\eta} + b_3 z_{\eta\eta} + a_1 r_{\xi\xi} + a_2 r_{\xi\eta} + a_3 r_{\eta\eta} = -J^2 \frac{1}{2w} \frac{\partial w}{\partial z} \tag{3.20}$$

$$a_1 z_{\xi\xi} + a_2 z_{\xi\eta} + a_3 z_{\eta\eta} + c_1 r_{\xi\xi} + c_2 r_{\xi\eta} + c_3 r_{\eta\eta} = -J^2 \frac{1}{2w} \frac{\partial w}{\partial r} \tag{3.21}$$

where the coefficients $(a_i, b_i, c_i, i = 1,3)$ are all functions of the coordinate derivatives as:

$$a_1 = a_{s1} + C_o a_{o1} + C_w a_{v1} \quad a_2 = a_{s2} + C_o a_{o2} + C_w a_{v2} \quad a_3 = a_{s3} + C_o a_{o3} + C_w a_{v3}$$

$$b_1 = b_{s1} + C_o b_{o1} + C_w b_{v1} \quad b_2 = b_{s2} + C_o b_{o2} + C_w b_{v2} \quad b_3 = b_{s3} + C_o b_{o3} + C_w b_{v3}$$

$$c_1 = c_{s1} + C_o c_{o1} + C_w c_{v1} \quad c_2 = c_{s2} + C_o c_{o2} + C_w c_{v2} \quad c_3 = c_{s3} + C_o c_{o3} + C_w c_{v3} \tag{3.22}$$

where:

$$a_{s1} = -(aa)\alpha \quad a_{s2} = 2(aa)\beta \quad a_{s3} = -(aa)\gamma$$

$$b_{s1} = (bb)\alpha \quad b_{s2} = -2(bb)\beta \quad b_{s3} = (bb)\gamma$$

$$c_{s1} = (cc)\alpha \quad c_{s2} = -2(cc)\beta \quad c_{s3} = -(cc)\gamma$$

$$a_{o1} = z_\eta r_\eta \quad a_{o2} = z_\xi r_\eta + z_\eta r_\xi \quad a_{o3} = z_\xi r_\xi$$

$$b_{o1} = z_\eta^2 \quad b_{o2} = 2(2 z_\xi z_\eta + r_\xi r_\eta) \quad b_{o3} = z_\xi^2$$

$$c_{o1} = r_\eta^2 \quad c_{o2} = 2(z_\xi z_\eta + 2 r_\xi r_\eta) \quad c_{o3} = r_\xi^2$$

$$a_{v1} = -z_\eta r_\eta \quad a_{v2} = z_\xi r_\eta + z_\eta r_\xi \quad a_{v3} = -z_\xi r_\xi$$

$$b_{v1} = r_\eta^2 \quad b_{v2} = -2 r_\xi r_\eta \quad b_{v3} = r_\xi^2$$

$$c_{v1} = z_\eta^2 \quad c_{v2} = -2 z_\xi s_\eta \quad c_{v3} = z_\xi^2$$

$$(aa) = z_\xi r_\xi + z_\eta r_\eta \quad (bb) = r_\xi^2 + r_\eta^2 \quad (cc) = z_\xi^2 + z_\eta^2$$

$$\alpha = (x_\eta^2 + y_\eta^2)/J^3 \quad \beta = (x_\xi x_\eta + y_\xi y_\eta)/J^2 \quad \gamma = (x_\xi^2 + y_\xi^2)/J^3 \tag{3.23}$$

When $C_o = 0$ and $C_w = 0$ the more standard Laplace or Poisson grid generation schemes result. This system is more complex than the usual Poisson-based grid generation schemes [14], but is still solvable using standard relaxation techniques. In this case, an iterative successive overrelaxation Gauss-Seidel solution technique is applied to solve the finite-difference equations resulting from a second-order central-difference approximation of the resulting equations. For example:

$$x_{\xi\xi} \approx \frac{x_{i+1,j} - 2x_{i,j} + x_{i-1,j}}{(\Delta\xi)^2} \tag{3.24}$$

$$x_{\xi\eta} \approx \frac{x_{i+1,j+1} - x_{i+1,j-1} + x_{i-1,j-1} - x_{i-1,j+1}}{(\Delta\xi\Delta\eta)} \tag{3.25}$$

A sample C-grid mesh network is given in Fig. 3.6 for a ducted propfan geometry. While this arrangement is not remarkably different from the H-grid network, the elimination of the highly skewed grid lines from the cowl leading edge region is certainly a desirable quality.

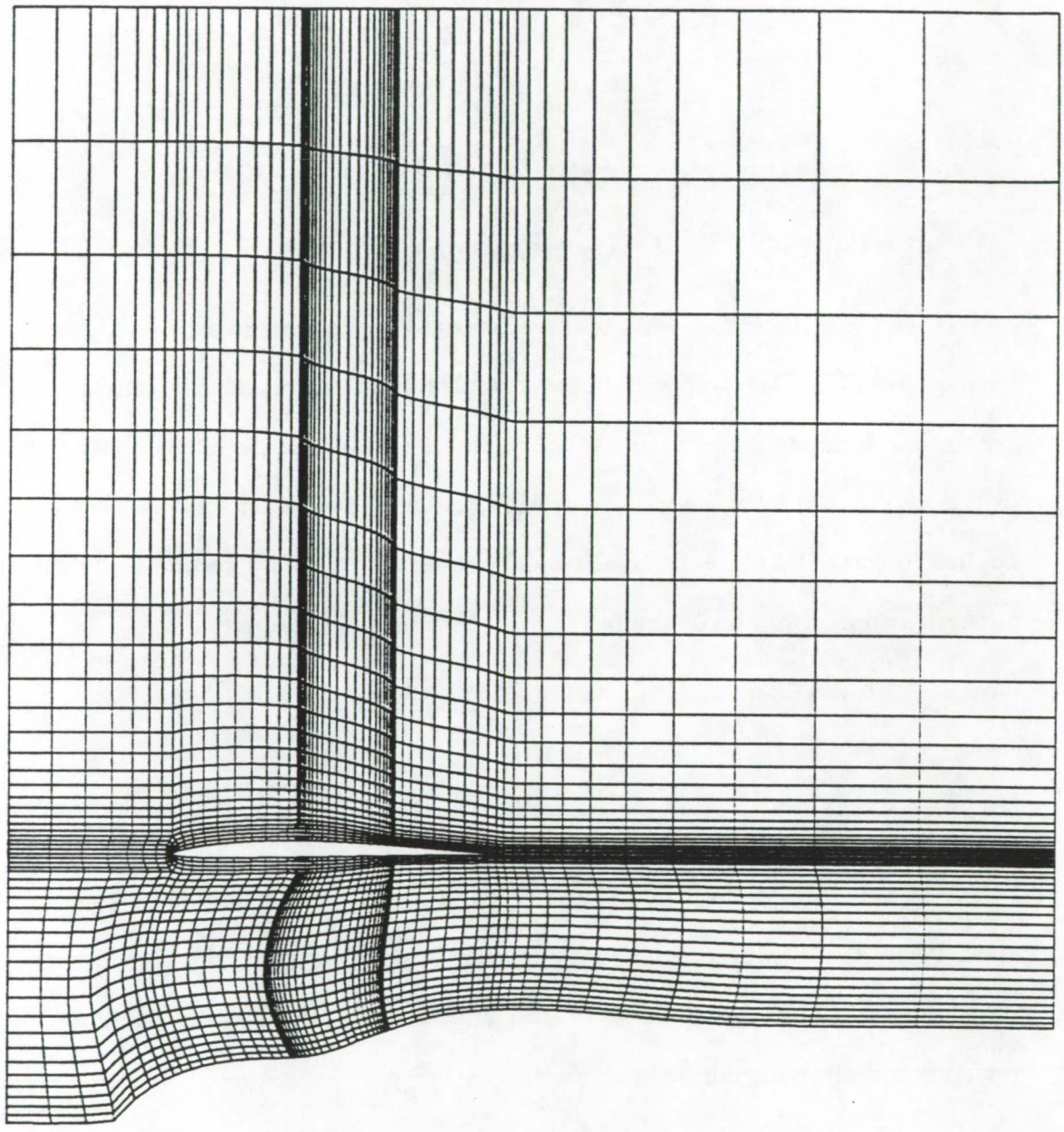

Figure 3.6: Sample multiple-block C-grid for a ducted propfan

4. 3D EULER NUMERICAL ALGORITHM

In this chapter, the numerical algorithm forming the basis of the ducted prop-fan aerodynamic analysis is described. Separate sections are presented for nondimensionalization, governing equations, boundary conditions, and discretization and time-integration schemes.

4.1 Nondimensionalization

To simplify the numerical treatment, all variables in the numerical solution are nondimensionalized by reference values as follows:

$$z = \frac{\tilde{z}}{L_{ref}} \quad r = \frac{\tilde{r}}{L_{ref}} \quad v_z = \frac{\tilde{v}_z}{v_{ref}} \quad v_r = \frac{\tilde{v}_r}{v_{ref}} \quad v_\theta = \frac{\tilde{v}_\theta}{v_{ref}}$$

$$p = \frac{\tilde{p}}{p_{ref}} \quad \rho = \frac{\tilde{\rho}}{\rho_{ref}} \quad \omega = \frac{\tilde{\omega} L_{ref}}{V_{ref}} \tag{4.1}$$

The reference quantities are defined as follows:

L_{ref} is determined from the maximum diameter of all the blade rows

p_{ref} is determined from the freestream total pressure

p_{ref} is determined from the freestream total density

a_{ref} is determined from the freestream conditions

$$= \sqrt{\gamma p_{ref}/\rho_{ref}}$$

v_{ref} is determined from the freestream acoustic velocity as

$$v_{ref} = \frac{a_{ref}}{\sqrt{\gamma}}$$

4.2 Governing Equations

The Euler equations of gas dynamics form the basis for the numerical solution procedure. In cylindrical coordinates, the strong conservation form of the inviscid equations of gas dynamics may be expressed in a reference frame rotating with the propeller as:

$$\int \frac{\partial}{\partial t}(\lambda Q)dV + \int_{dA} \left[\lambda \bar{F} dA_z + \lambda \bar{G} dA_r + \lambda(\bar{H} - r\omega\bar{Q})dA_\theta\right] = \int \lambda S dV + \int \lambda K dV \tag{4.2}$$

where:

$$Q = \begin{bmatrix} \rho \\ \rho v_z \\ \rho v_r \\ r\rho v_\theta \\ \rho e_t \end{bmatrix} \tag{4.3}$$

$$F = \begin{bmatrix} \rho v_z \\ \rho v_z^2 + p \\ \rho v_z v_r \\ r\rho v_z v_\theta \\ \rho v_z H \end{bmatrix} \quad G = \begin{bmatrix} \rho v_r \\ \rho v_z v_r \\ \rho v_r^2 + p \\ r\rho v_r v_\theta \\ \rho v_r H \end{bmatrix} \quad H = \begin{bmatrix} \rho v_\theta \\ \rho v_z v_\theta \\ \rho v_r v_\theta \\ r(\rho v_\theta^2 + p) \\ \rho v_\theta H \end{bmatrix} \tag{4.4}$$

$$\bar{F} = F(\bar{Q}) \quad \bar{G} = G(\bar{Q}) \quad \bar{H} = H(\bar{Q}) \tag{4.5}$$

$$K = \begin{bmatrix} 0 \\ 0 \\ \frac{\rho v_\theta^2 + p}{r} \\ 0 \\ 0 \end{bmatrix} \qquad \lambda = \begin{cases} 1.0, & \text{outside blade row;} \\ 1 + \frac{(\theta_{ss} - \theta_{ps})N}{2\pi} & \text{inside blade row} \end{cases} \tag{4.6}$$

Here, v_z, v_r, v_θ represent the velocity components in the axial, radial, and circumferential directions, respectively. The total energy function, e, is defined as:

$$e_t = \frac{p}{(\gamma - 1)\rho} + \frac{1}{2}(v_z^2 + v_r^2 + v_\theta^2) \tag{4.7}$$

The total enthalpy, H, is related to the total energy by:

$$H = e_t + \frac{p}{\rho} \tag{4.8}$$

These equations are based on the average-passage system of equations developed by Adamczyk [15] for the prediction of time-averaged flows in counter-rotating and multiple blade row machines. The system of equations is closed through the specification of the blockage (λ) and source terms (S). The closure model developed by Adamczyk [16] was utilized in this study to define these terms. Further details are given in the references cited.

The governing equations are applied to a generalized finite volume in physical space as shown in Fig. 4.1. The cell surface areas dA_z, dA_r, and dA_θ are calculated using the cross product of the diagonals of a cell face, and the cell volume is determined by a procedure outlined by Hung and Kordulla [17] for generalized nonorthogonal cells.

For convenience, a special operator $L(Q)$ is defined as:

$$L(\bar{Q}) = -\left(\int_{dA}\left[\lambda \bar{F} dA_z + \lambda \bar{G} dA_r + \lambda(\bar{H} - r\omega\bar{Q})dA_\theta\right]\right) + \int \lambda S dV + \int \lambda K dV \tag{4.9}$$

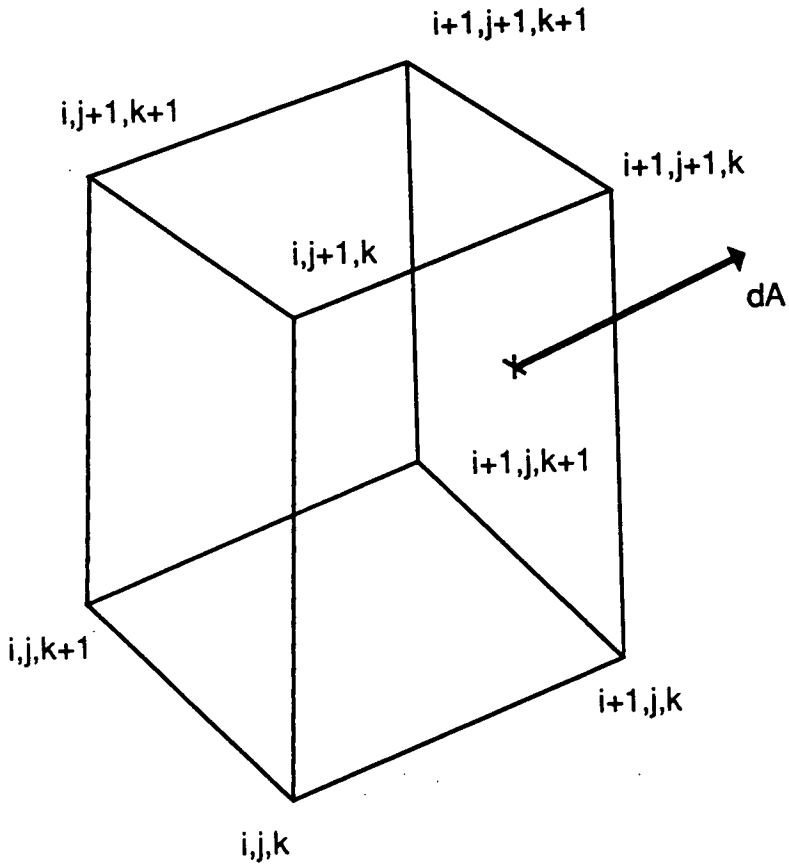

Figure 4.1: Three-dimensional finite volume cell

The flux variables $\bar{F}, \bar{G}$, and $\bar{H}$ are determined at each grid cell interface by averaging the cell-centered dependent variables from the individual finite volumes adjoining the interface. The L operator represents the summation of fluxes of mass, momentum, and energy for the control volume V under the influence of blockage and source terms.

4.3 Runge-Kutta Time Integration

The time-stepping scheme used to advance the discretized equations is a four-stage Runge-Kutta integration. The solution proceeds as:

$$Q_1 = Q^n - \alpha_1 \Delta t[L(Q^n) + D(Q^n)]$$

$$Q_2 = Q^n - \alpha_2 \Delta t[L(Q_1) + D(Q^n)]$$

$$Q_3 = Q^n - \alpha_3 \Delta t[L(Q_2) + D(Q^n)]$$

$$Q_4 = Q^n - \alpha_4 \Delta t[L(Q_3) + D(Q^n)]$$

$$Q^{n+1} = Q_4 \tag{4.10}$$

where:

$$\alpha_1 = \frac{1}{8} \quad \alpha_2 = \frac{1}{4} \quad \alpha_3 = \frac{1}{2} \quad \alpha_4 = 1 \tag{4.11}$$

An artificial dissipation operator (D) has been added to control oscillations in the numerical solution. A further discussion on this term is given in the following section. Jameson [18] determined that this scheme is stable for all time steps satisfying the CFL-related time step limitation

$$CFL \leq 2\sqrt{2} \tag{4.12}$$

An acceleration technique known as local time stepping is used to enhance convergence to the steady-state solution. Local time stepping utilizes the maximum allowable time increment at each point during the course of the solution. While this destroys the physical nature of the transient solution, the steady-state solution is unaffected and can be obtained more efficiently.

4.4 Artificial Dissipation

The Runge-Kutta algorithm described above utilizes an artificial numerical dissipation term $D(Q)$ to suppress the odd-even point decoupling often observed for central-difference formulations. This problem is especially prevalent near shock waves, and it has been observed that the formulation of the dissipative term can have a significant influence on the final numerical solution. Jameson [18] demonstrated that a dissipative system combining second and fourth difference smoothing terms can effectively eliminate undesirable numerical oscillations without destroying the accuracy of the solution. This dissipation operator is constructed in the following manner:

$$D_z(Q) = d_{i+\frac{1}{2},j,k} - d_{i-\frac{1}{2},j,k} \tag{4.13}$$

$$d_{i+\frac{1}{2},j,k} = \frac{V_{i+\frac{1}{2},j,k}}{(\Delta t)_{i+\frac{1}{2},j,k}} \left[\epsilon^2_{i+\frac{1}{2},j,k} \Delta_z Q_{i+\frac{1}{2},j,k} - \epsilon^4_{i+\frac{1}{2},j,k} \Delta_z^3 Q_{i+\frac{1}{2},j,k} \right] \tag{4.14}$$

where:

$$\epsilon^2_{i+\frac{1}{2},j,k} = \kappa^2 max(\nu_{i+1,j,k}, \nu_{i,j,k}) \tag{4.15}$$

$$\epsilon^4_{i+\frac{1}{2},j,k} = max(0, \kappa^4 - \epsilon^2_{i+\frac{1}{2},j,k}) \tag{4.16}$$

$$\nu_{i,j,k} = \frac{|p_{i+1,j,k} - 2p_{i,j,k} + p_{i-1,j,k}|}{|p_{i+1,j,k} + 2p_{i,j,k} + p_{i-1,j,k}|} \tag{4.17}$$

Typical values for the second and fourth difference damping constants are:

$$\kappa^2 = \frac{1}{4} \qquad \kappa^4 = \frac{1}{64} \tag{4.18}$$

The complete dissipation operator $D_{i,j,k}$ is constructed as the sum of the dissipation operators in each of the respective coordinate directions as:

$$D_{i,j,k} = (D_z)_{i,j,k} + (D_r)_{i,j,k} + (D_\theta)_{i,j,k} \tag{4.19}$$

4.5 Implicit Residual Smoothing

An effective technique for extending the stability limit of many explicit schemes is implicit residual smoothing. Residual smoothing attempts to accelerate the propagation of changes in the dependent variables by filtering the residuals of the calculation (which may also be interpreted as the local time derivative of the computational solution) at each time step. By enhancing the transfer of information between grid points, calculation time steps much larger than the stability-limited values may be utilized. Residual smoothing was originally introduced by Lerat (see e.g. Hollanders, et al. [19]) for use with the Lax-Wendroff scheme and later applied to Runge-Kutta schemes by Jameson and Baker [20] as a technique to acclerate convergence for steady-state calculations. Jorgenson and Chima [21] applied this technique for unsteady flows and obtained a speedup of about 5 for their calculations without any change in the unsteady solution.

Since the time rate of change of the dependent variables $\partial Q/\partial t$ is in essence controlled by a residual operator $R(Q) = L(Q) - D(Q)$, it would follow that any measure which accelerates the propagation of changes in the residual throughout the domain would ultimately enhance convergence. The implicit residual smoothing operator used in this study can be written as:

$$(1 - \epsilon_z \delta_{zz})(1 - \epsilon_r \delta_{rr})(1 - i\epsilon_\theta \delta_{\theta\theta})\hat{R}_{i,j,k} = R_{i,j,k} \tag{4.20}$$

where the differencing operator δ is expressed as:

$$\delta_{zz} R_{i,j,k} = R_{i+1,j,k} - 2R_{i,j,k} + R_{i-1,j,k} \tag{4.21}$$

A value of $\epsilon_{zz} = \epsilon_{rr} = \epsilon_{\theta\theta} = 2$ is typically used.

The reduction is applied along each coordinate direction separately as:

$$R^*_{i,j,k} = (1 - \epsilon_z \delta_{zz})^{-1} R_{i,j,k} \tag{4.22}$$

$$R^{**}_{i,j,k} = (1 - \epsilon_z \delta_{rr})^{-1} R^*_{i,j,k} \tag{4.23}$$

$$R^{***}_{i,j,k} = (1 - \epsilon_z \delta_{\theta\theta})^{-1} R^{**}_{i,j,k} \tag{4.24}$$

$$\hat{R}_{i,j,k} = R^{***}_{i,j,k} \tag{4.25}$$

where each of the first three steps above requires the inversion of a scalar tridiagonal matrix. The residual smoothing operator is applied at the first and third stage during the four-stage Runge-Kutta algorithm. The time-marching scheme then becomes:

$$Q_1 = Q^n - \alpha_1 \hat{R}(Q^n)$$

$$Q_2 = Q^n - \alpha_2 R(Q_1)$$

$$Q_3 = Q^n - \alpha_3 \hat{R}(Q_2)$$

$$Q_4 = Q^n - \alpha_4 R(Q_3)$$

$$Q^{n+1} = Q_4 \tag{4.26}$$

The implicit residual smoothing operator applied in this context can increase the effective time step by a factor of 3 or more, and can result in a 50% reduction in overall CPU time.

4.6 Boundary Conditions

Inflow and exit boundary conditions are applied numerically using characteristic theory. A one-dimensional isentropic system of equations is utilized to derive the following characteristic equations at an axial inflow/outflow boundary:

$$\frac{\partial C^-}{\partial t} - (v_z - a)\frac{\partial C^-}{\partial z} = 0 \tag{4.27}$$

$$\frac{\partial C^+}{\partial t} + (v_z + a)\frac{\partial C^+}{\partial z} = 0 \tag{4.28}$$

where:

$$C^- = v_z - \frac{2a}{\gamma - 1} \qquad C^+ = v_z + \frac{2a}{\gamma - 1} \tag{4.29}$$

In order to efficiently process boundary information in the numerical solution, phantom cells are located just outside the computational domain to permit the unmodified application of the interior point scheme at near boundary cells. Boundary condition information is effectively introduced into the solution by properly controlling the dependent variables in the phantom cells while permitting the application of the standard interior point scheme at near boundary cells.

For subsonic normal inflow, the upstream running invariant C^- is extrapolated to the inlet, and along with the equation of state, specified total pressure, total temperature, and flow angle, the flow variables at the boundary may be determined. A second boundary condition was available as an option which specifies the mass flow through the inlet, although this option is not recommended. At the exit, a static pressure is specified at the hub for internal flows, and at the outer boundary for external flows. The remaining pressures along the outflow boundary are calculated by integrating the radial momentum equation:

$$\frac{\partial p}{\partial r} = \frac{\rho v_\theta^2}{r} \tag{4.30}$$

In this case, the downstream running invariant C^+ is used to update the phantom cells at the exit boundary. Far-field boundaries also use this characteristic technique based on whether the local flow normal to the boundary passes into or out of the domain. The solid surfaces (hub, cowl, airfoils) must satisfy flow tangency:

$$\vec{V} \cdot \vec{n} = 0 \tag{4.31}$$

In this case, we specify no convective flux through the boundary (an impermeable surface), and hence, only pressure is needed at the phantom cell. The pressure may be extrapolated, or updated using a variant of the normal momentum equation. In this case, extrapolation was found to be the most effective technique based on rapid convergence and adequate results.

4.7 Multiple-Block Coupling

For the multiple-block C-grid scheme, the Euler solution is performed on a single grid block at a time. Special boundary conditions along block boundaries are therefore required to provide some transport of information between blocks. This transport is provided through a simple procedure which relies on the fact that the grid block boundaries have coincident grid points. Since the standard interior point scheme is performed at the first grid cell off the block boundary, all that is required is to determine the fluxes along the block boundaries themselves. Phantom points are provided along each side of a block boundary to accommodate the flux calculation at the block boundary cell face. The flow variables in the phantom cells are provided by interrogating the corresponding cell in the adjacent block when a particular value is required. After each stage of the Runge-Kutta integration for each block, the block boundary phantom cells are updated by utilizing the new dependent variable values from the adjacent blocks. This direct specification technique was compared to a characteristic-based method similar to the inlet and exit boundary condition routines, and was found to provide enhanced convergence behavior.

Artificial damping is applied at the block boundaries by neglecting the fourth order derivative term. Implicit residual smoothing is applied at the block boundary by imposing a zero residual gradient (i.e. $(dR/dz) = 0.0$) condition at the boundary.

4.8 Solution Procedure

The numerical solution is performed in an identical manner for both the H-grid and multiple-block C-grid Euler analyses. Assuming that the numerical grid and flow parameters are known, the time-marching procedure may begin from some set of initial data. This initial data is initially specified as a uniform flow, or may be implied from a previous solution. The time-marching procedure is applied iteratively to update the flow variables as the solution proceeds. The solution is deemed converged when the average residual R has been reduced by a factor of 10^{-3}.

In the case of a counter-rotation calculation, the overall process of obtaining a converged solution is applied iteratively for each blade row as the source terms for the adjacent blade rows are updated. Thus, the time-marching loop is contained in an overall cycle which updates these source terms. The counter-rotation solutions were deemed converged when the differences in residuals between cycles were less than 10^{-2}.

5. RESULTS

Several numerical results from the 3D Euler analyses described in Chapter 3 are presented in the sections which follow. Initial results are given to verify the accuracy of the 3D Euler formulation for steady flow about unducted propfans. Calculations are presented for both the 8-bladed SR7 propfan geometry, and a 2-bladed SR7 propfan for which experimental airfoil surface static pressure distribution data were available. Several calculations for ducted propfans are presented. The numerics of the ducted propfan Euler analyses are first verified through comparisons with a two-dimensional numerical prediction of a circular arc cowl about a zero thickness nonrotating propeller aligned with the incoming flow. A second demonstration of the analyses is then performed for a fictitious ducted SR7 propfan. Predicted results are compared with numerical data obtained from a frequency domain panel method analysis for ducted propellers. A third set of calculations is given for a low speed ducted propeller. The predicted cowl surface pressure coefficient distribution is compared with experimental data for this geometry. Finally, the analyses are extensively compared with high speed experimental data for a 1.15 pressure ratio ducted fan configuration. Each case is discussed separately in the sections which follow.

5.1 SR7 8-Bladed Propfan

In order to verify the numerics of the 3D Euler solver, several initial calculations were performed for steady flows about unducted propfans. A number of experimental studies have been performed for the unducted SR7 propfan geometry ranging from scaled wind tunnel tests to in-flight measurements. The SR7 propfan utilizes 8 blades with 41 degrees of sweep at the tip. A special hub contour is employed to eliminate flow choking at the hub. A description of the SR7 design parameters is given in Fig. 5.1. A particularly useful set of experimentally determined performance data for the SR7 was given by Stefko et al. [22]. In this study, a 2/9 scale model of the SR7 propfan was tested in a wind tunnel over a wide range of blade setting angles and operating conditions. A 70x35x15 (axial x radial x circumferential) numerical H-grid (as shown in Fig. 5.2) was generated to simulate this flow. Calculations were performed over a wide range of advance ratios and blade setting angles for flight Mach numbers of 0.7 and 0.8. All of the calculations for the unducted propfans described below were performed using the 3D H-grid Euler analysis operating in the unducted mode (no cowl boundary conditions are applied).

A comparison of the predicted and experimental power coefficient map for the SR7 propfan at a flight Mach number of 0.8 is given in Fig. 5.3. During the investigation of the SR7 geometry, it was immediately observed that the predicted results were extremely sensitive to the blade setting angle and required an accurate assessment of the deflected blade shape. Since no reasonable means was available to adjust the blade shape for each run, the blade angle was adjusted in a manner which permitted the predicted power coefficient to match the experimental power coefficient at the

design operating conditions. All other runs were made relative to this blade setting angle. The predicted power coefficient map illustrated in Fig. 5.3 is in fairly good agreement with the experimental curves for each blade setting angle. The comparison appears to worsen for larger blade setting angles as the power coefficient was consistently underpredicted by about 10%. This may be due to the inviscid flow assumption in the present analysis.

A plot of the predicted propfan surface static/total pressure ratio contours for a Mach number of 0.8, 3/4 blade setting angle of 60.2 degrees, and an advance ratio of 3.06 is given in Fig. 5.4. This contour plot clearly illustrates the spinner and blade root stagnation regions, and a shock which extends along the suction surface of the propfan blade.

A similar series of calculations was performed at a flight Mach number of 0.7. In this case, an examination of the blade spanwise loading profiles was performed. A comparison of the predicted spanwise blade elemental power coefficient distributions with experimental data is given for several loading factors for $M = 0.7$ for the 8-bladed SR7 propfan in Fig. 5.5. The predicted power loading factors were somewhat different from the experimentally measured values; however, it is obvious that the experimental data brackets the predicted spanwise distributions for each power loading value.

5.2 SR7 2-Bladed Propfan Modane Tests

A second, more extensive comparison of predicted results for steady unducted propfan flows was performed based on the test of the SR7 airfoil at the Modane wind tunnel test facility reported by Bushnell [23]. In this case, the propfan driver did

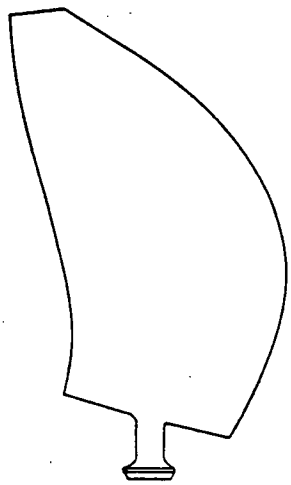

Characteristic	SR7
Number of blades	8
Tip sweep angle, degrees	41
Tip Speed (m/s)	243.8
Power loading (kW/m**2)	256.85
Activiy factor	227
Integrated design lift coefficient	0.202
Airfoils	NACA 16 and 65/CA
Ratio of nacelle maximum diameter to propeller diameter	0.35
Cruise design Mach number	0.8
Cruise design advance ratio	3.06
Cruise design power coefficient	1.45

Figure 5.1: SR7 propfan design characteristics

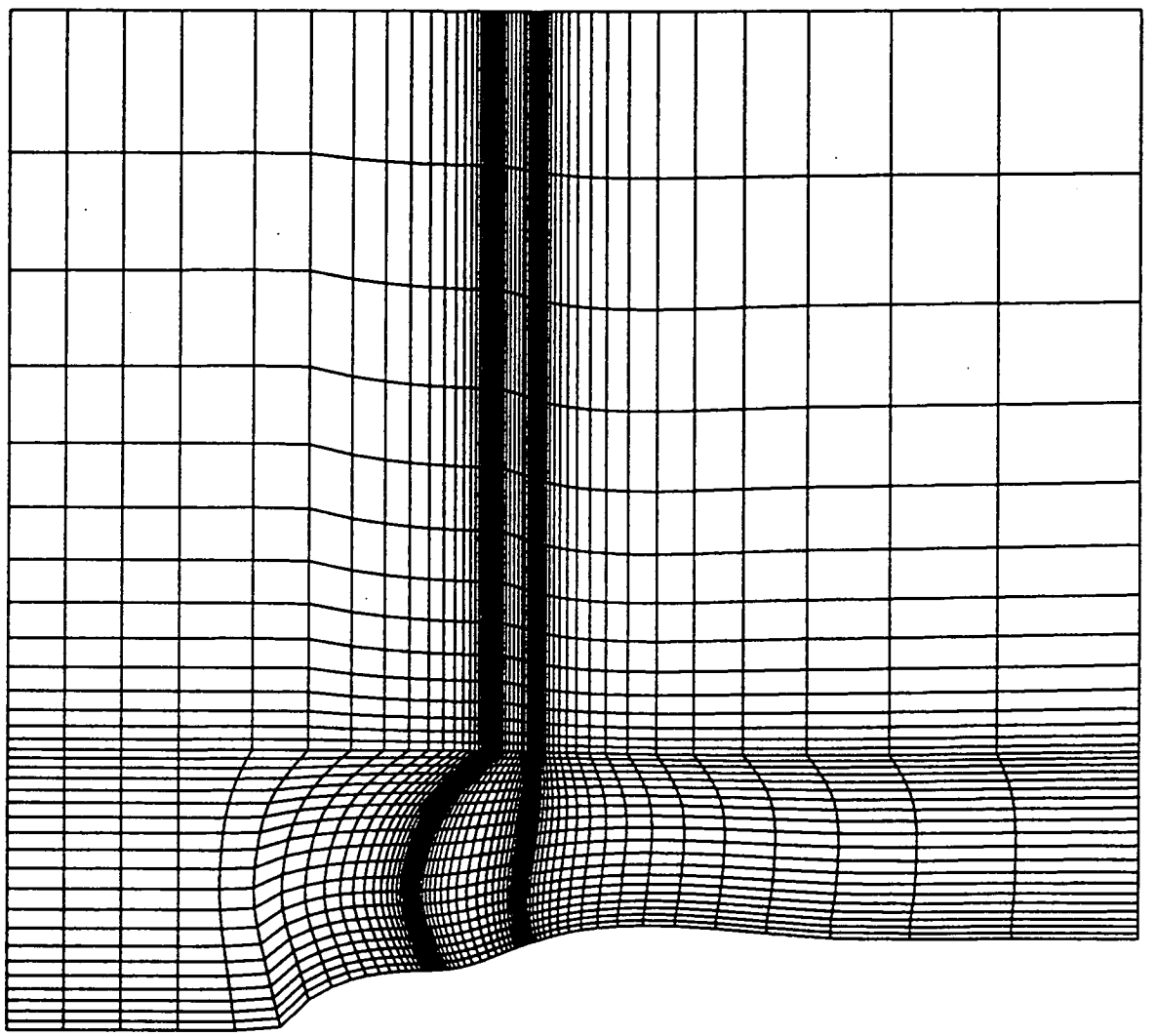

Figure 5.2: Axisymmetric plane projection of 70x35x15 SR7 grid

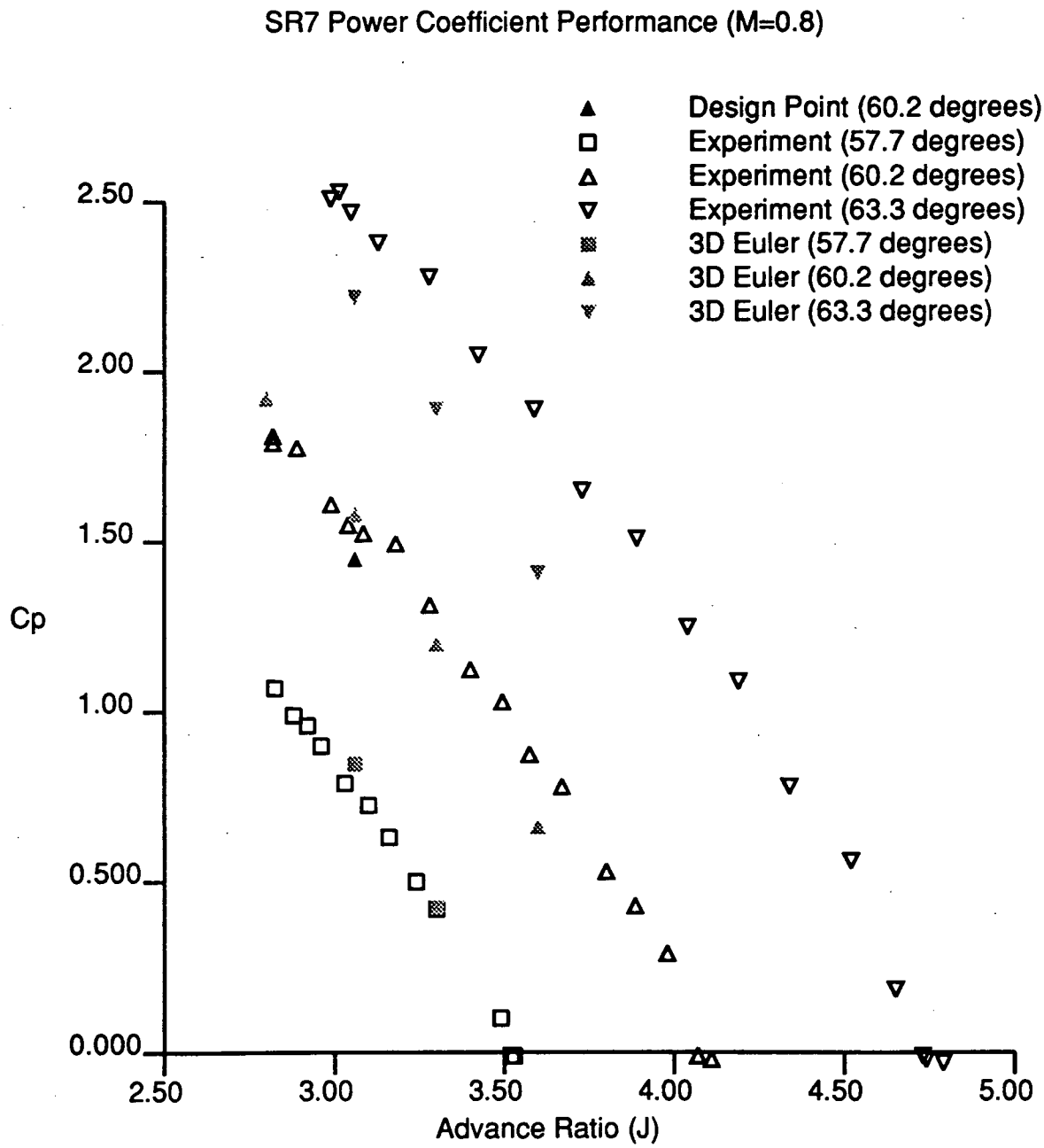

Figure 5.3: Comparison of predicted, experimental, and design power coefficient distributions for 8-bladed SR7 propfan (M=0.8)

Figure 5.4: Predicted propfan surface static/total pressure ratio contours for 8-bladed SR7 propfan (M=0.8)

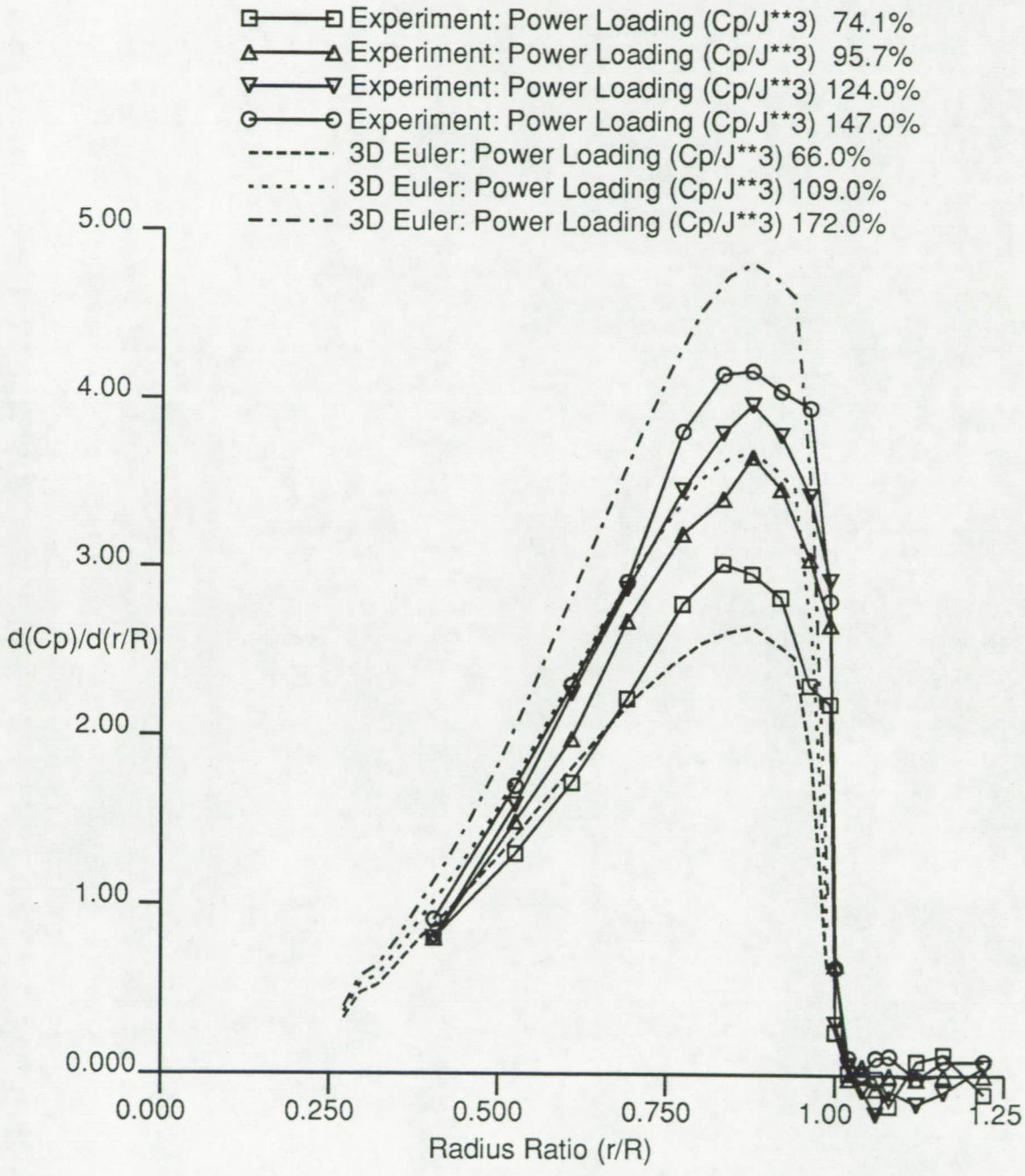

Figure 5.5: Comparison of predicted and experimental blade spanwise elemental power coefficient loading distributions for the 8-bladed SR7 propfan (M=0.7)

not have enough power to drive the 8-bladed configuration, so a 2-bladed version was tested instead. The airfoil surfaces were instrumented to permit the measurement of steady airfoil surface static pressures. The geometry and 120x45x25 H-grid used for these calculations are given in Fig. 5.6. This grid system utilized 49 points axially and 21 points radially on the airfoil surface, which should be considered near minimum to accurately predict airfoil surface pressure distributions.

Predictions were compared for a 3/4 radius blade setting angle of 30.58 degrees. The freestream Mach number was 0.2, with an advance ratio of 0.881. Predicted airfoil surface static pressure coefficient distributions are compared with experimental data at spanwise locations of 9.9%, 55.6%, and 94.4% (r/R) in Figs. 5.7-5.9, respectively. The agreement between experiment and prediction is generally very good, with some small disagreement near the leading edge of each cross section. This discrepancy may be due to several factors. As in the 8-bladed SR7 calculations, the exact deflected airfoil shape and blade setting angle are unknown (experimental uncertainty is on the order of 1 degree), which introduces a significant source of error in the calculation. In addition, this particular flow condition gives rise to a leading edge vortex which bends across the suction surface of the blade. This feature is evident in both the experimental data and the calculation.

In order to qualitatively compare the predicted airfoil surface pressure distributions, a comparison of the predicted and experimental airfoil surface static pressure contours is given in Figs. 5.10-5.11 for the pressure (face) and suction (camber) surfaces, respectively. The pressure surface shows little variation; however, the suction surface displays a noticable region of high pressure (presumably a result of the leading

edge vortex) which bends across the airfoil surface near the leading edge from roughly 50%-100% span. This feature is also evident in the experimental static pressure contours, and illustrates the remarkable similarity between prediction and experiment.

5.3 Symmetric Circular Arc Cowl Test Case

In order to verify the accuracy of the Euler formulation for a ducted propfan geometry, a numerical test case was initiated based on a symmetric double circular arc airfoil cowl about a zero thickness, nonrotating propeller with a large hub diameter. A single passage of this geometry is given in Fig. 5.12. The propeller blades are aligned with the incoming flow and are therefore "invisible" to the inviscid numerical solution. These aspects, combined with the large hub diameter and large number of propeller airfoils (320) essentially reduce the aerodynamics to two dimensions. Therefore, the 3D Euler results were compared with an extensively verified 2D Euler code based on the hopscotch [24] time-marching technique for a similar two-dimensional geometry. A comparison with numerical, rather than experimental, data should be more enlightening in this instance since discrepancies between experimental data and calculations may not necessarily be due to boundary condition errors (i.e., viscous effects, grid induced errors, unsteadiness, etc.).

The 3D H-grid calculations were performed on a 91x41x5 grid, while the 2D calculations were performed on a 91x21 grid. A comparison of the 2D grid and the 3D grid axisymmetric projection is given in Fig. 5.13. Since the 2D problem is perfectly symmetric, only half of the flowfield was computed. Each grid utilized 31

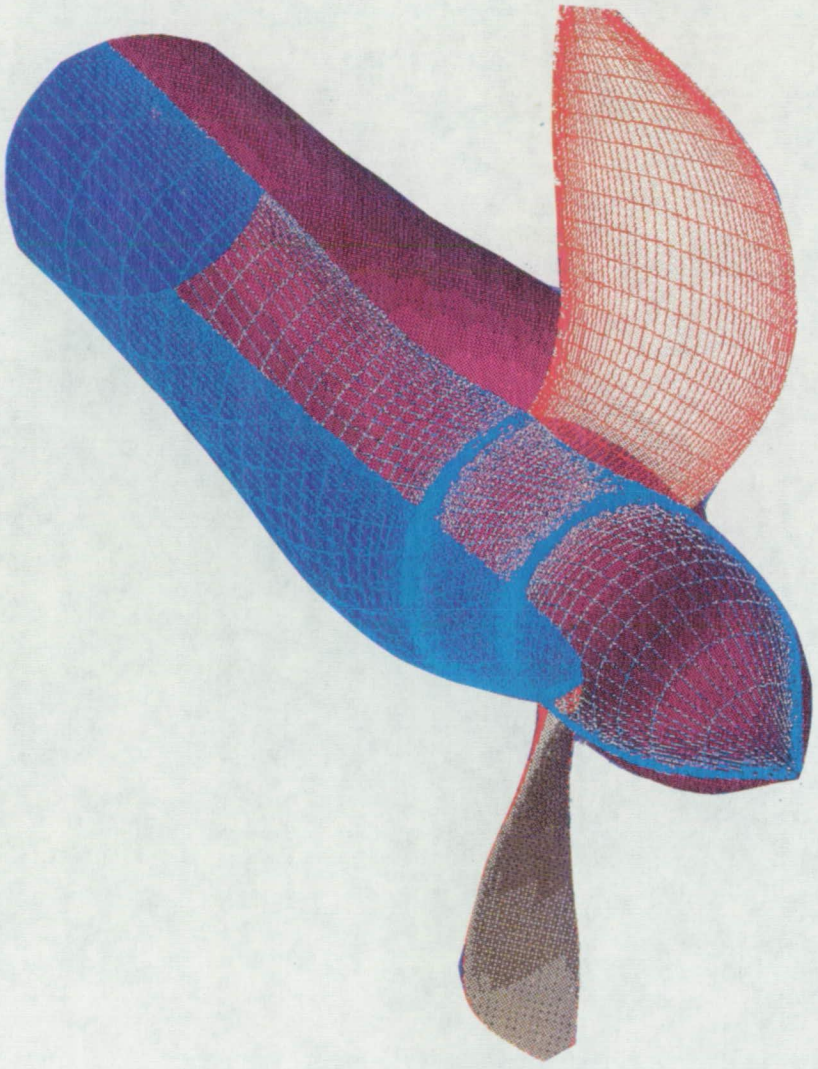

Figure 5.6: 2-bladed SR7 propfan geometry and 120x45x25 grid for Modane test comparison

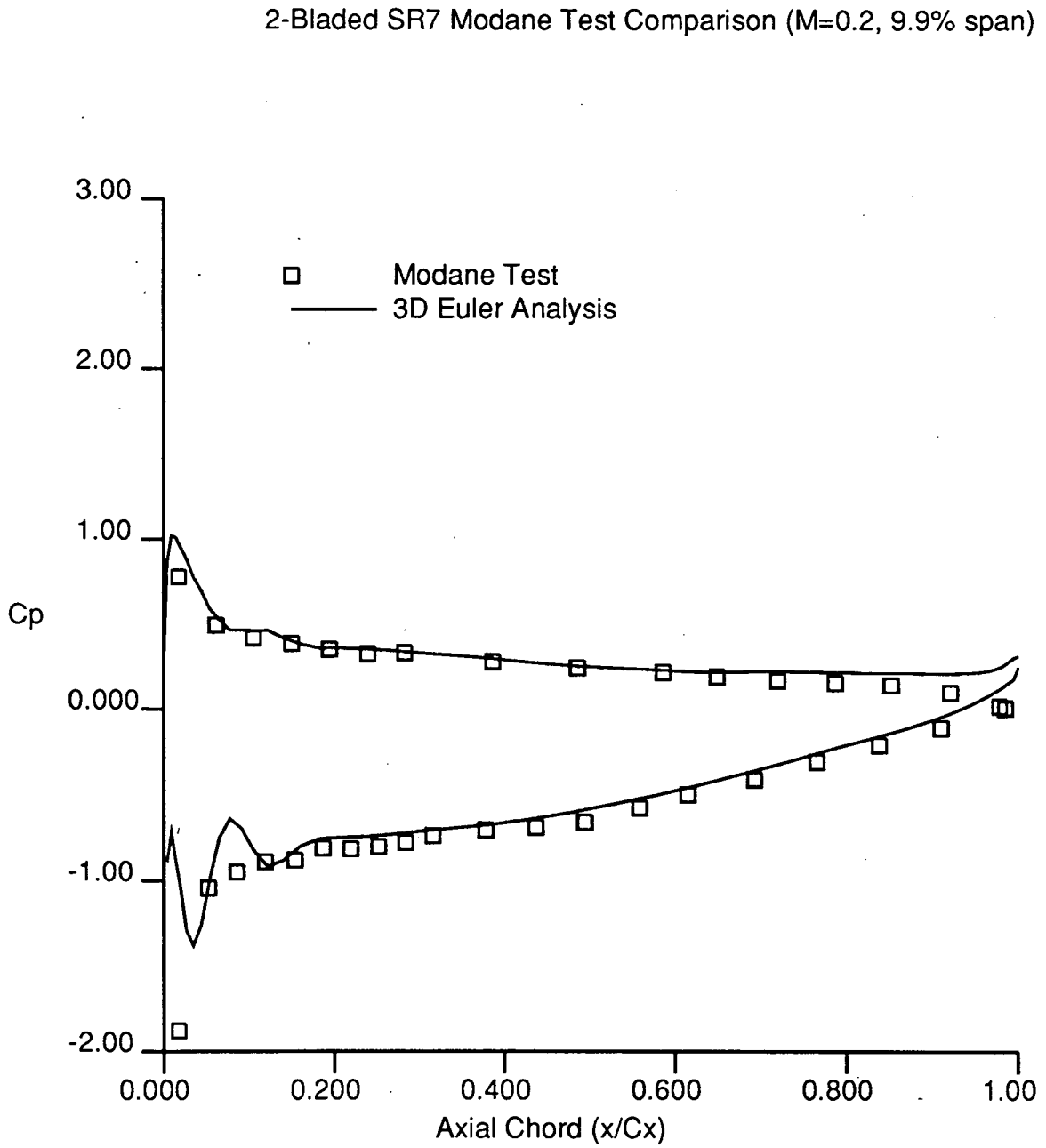

Figure 5.7: Comparison of predicted and experimental airfoil surface static pressure coefficient distributions for 2-bladed SR7 propfan Modane test (9.9% span)

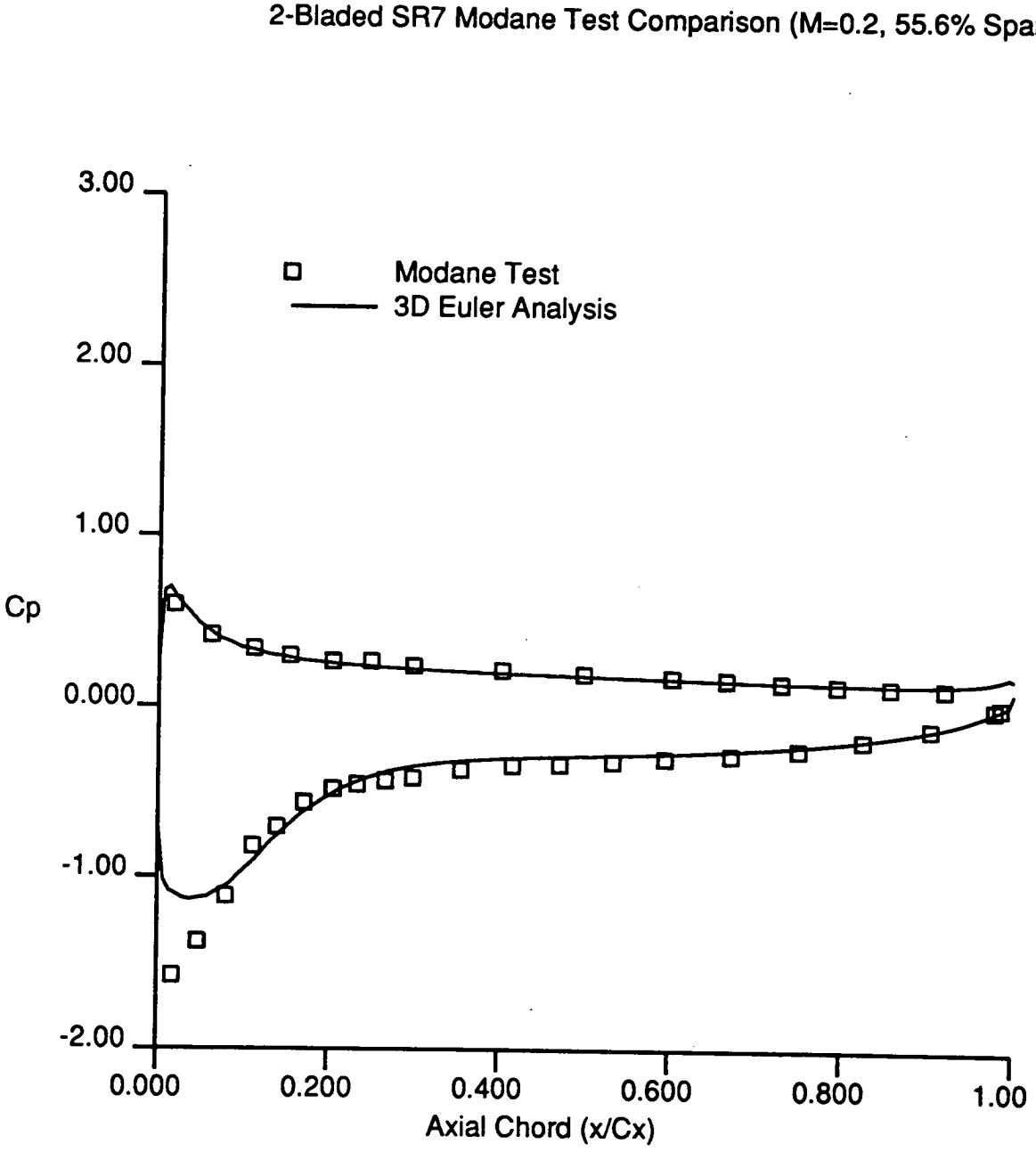

Figure 5.8: Comparison of predicted and experimental airfoil surface static pressure coefficient distributions for 2-bladed SR7 propfan Modane test (55.6% span)

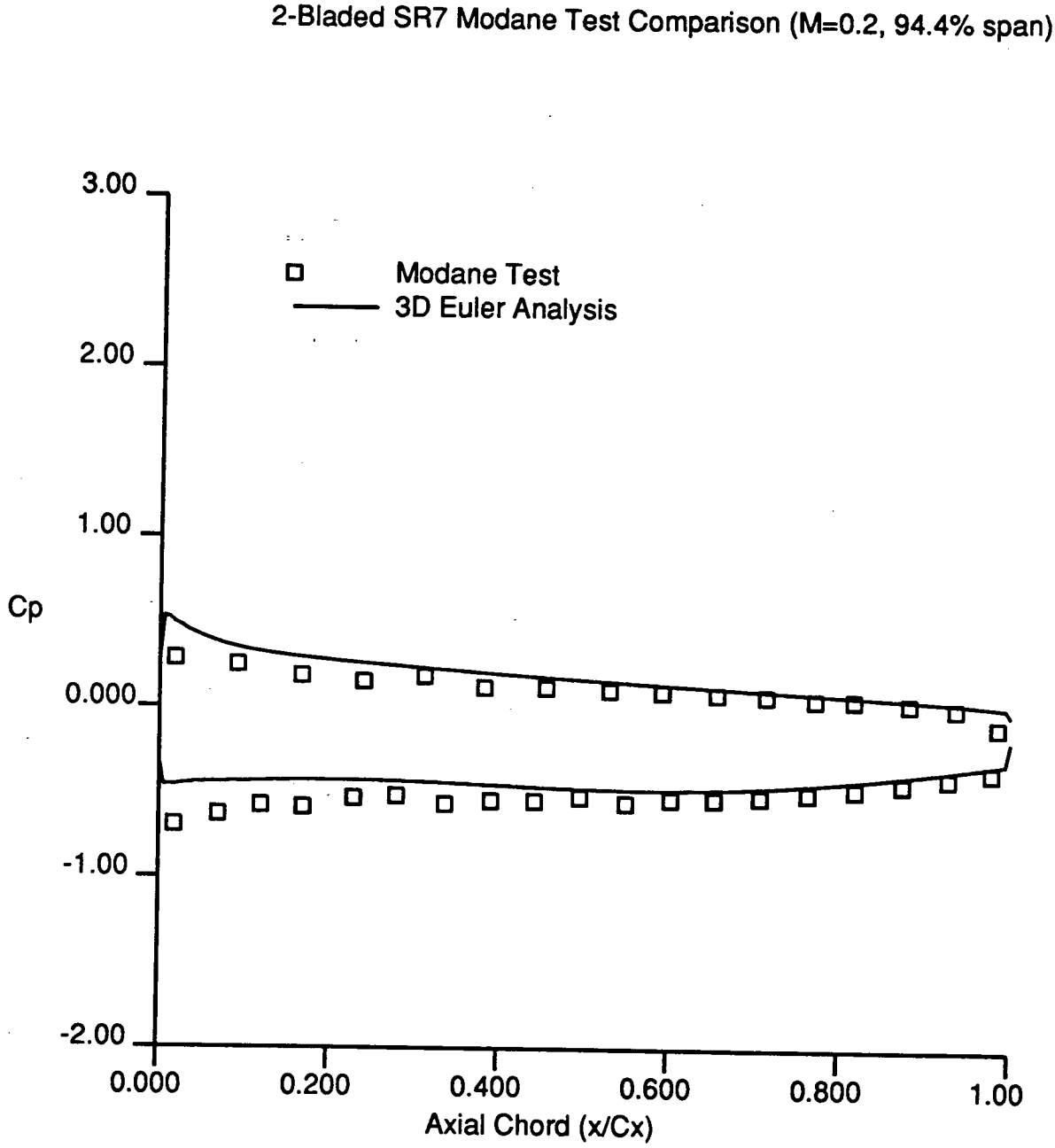

Figure 5.9: Comparison of predicted and experimental airfoil surface static pressure coefficient distributions for 2-bladed SR7 propfan Modane test (94.4% span)

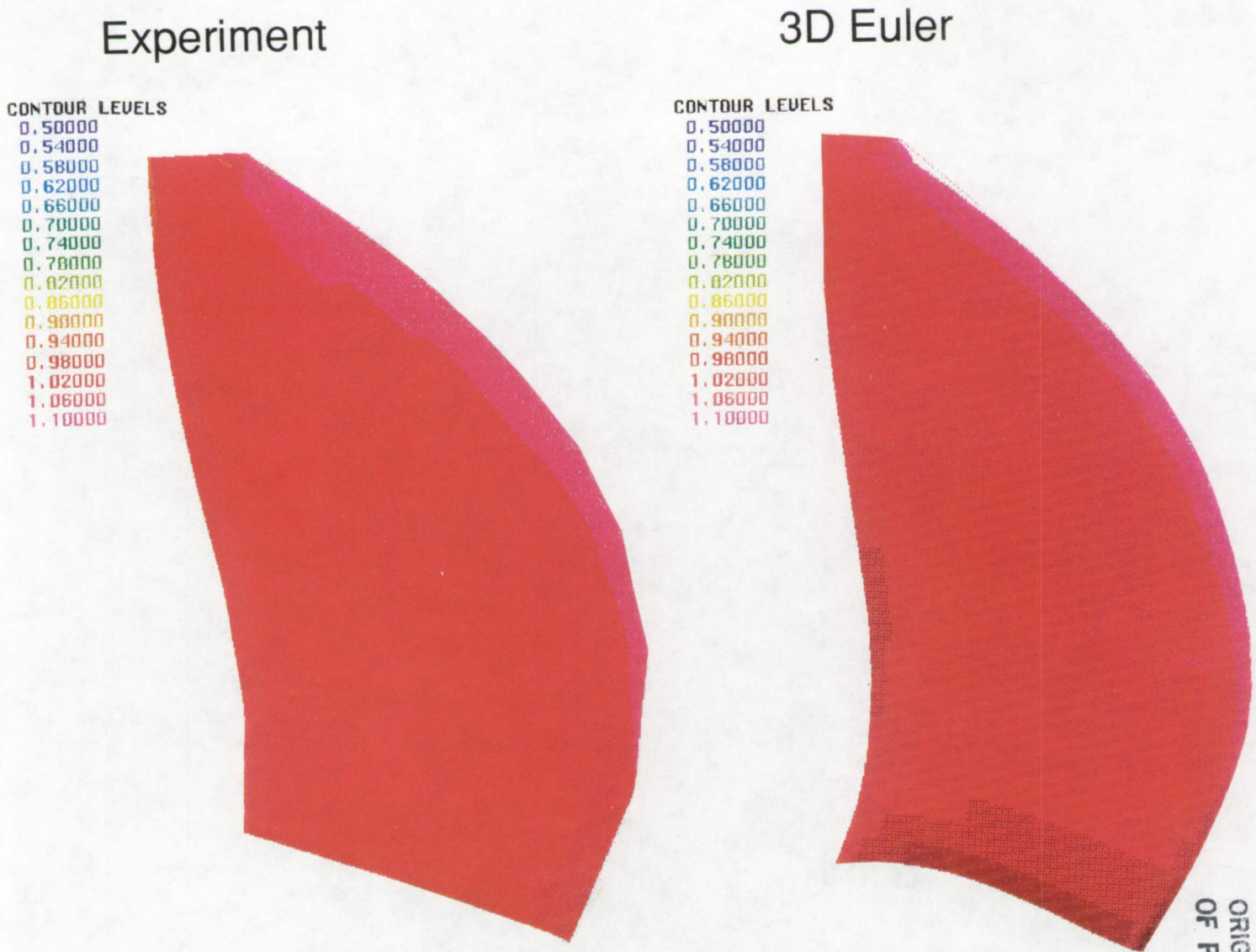

Figure 5.10: Comparison of predicted and experimental airfoil pressure surface static/total pressure ratio contours for 2-bladed SR7 propfan

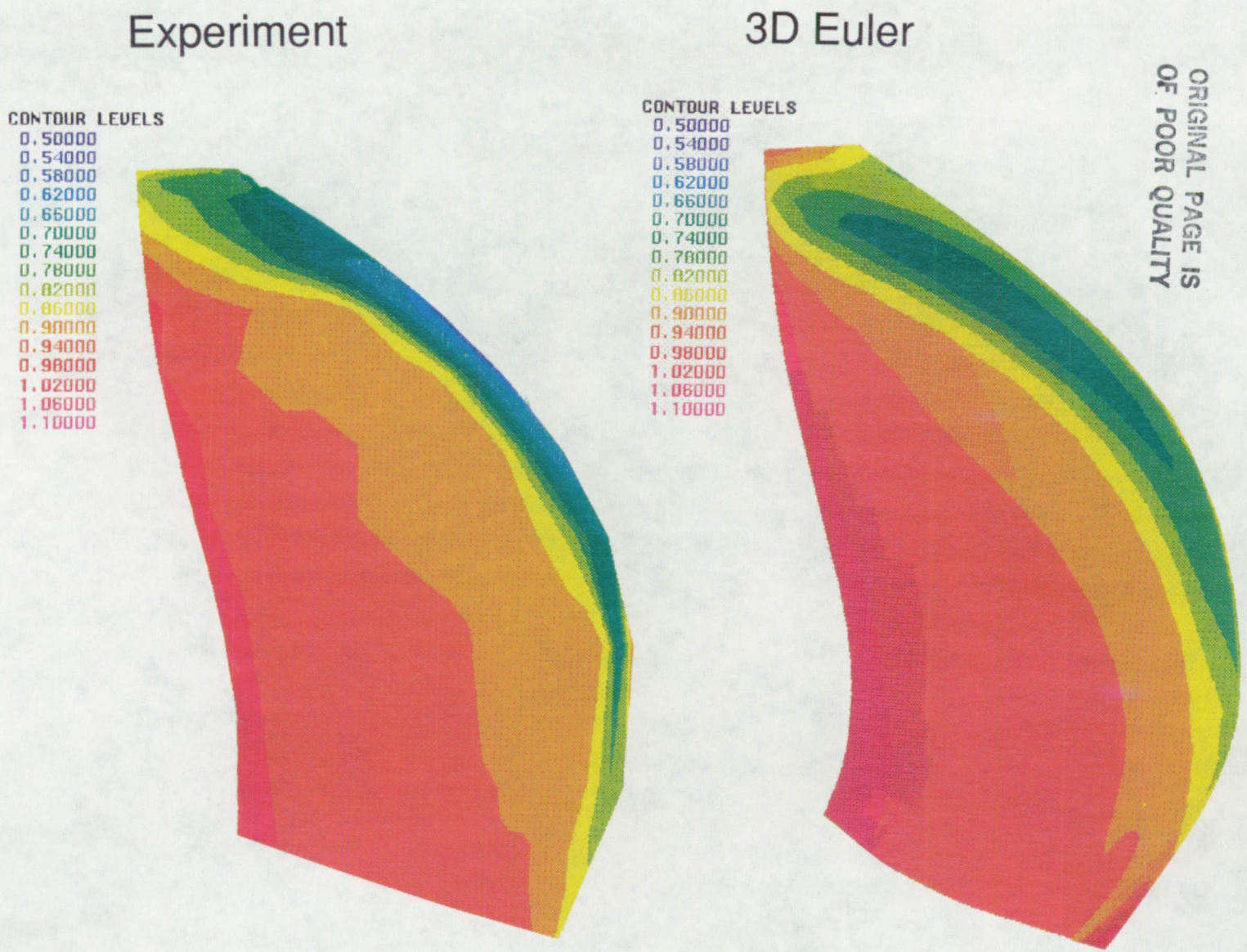

Figure 5.11: Comparison of predicted and experimental airfoil suction surface static/total pressure ratio contours for 2-bladed SR7 propfan

points to define the cowl upper and lower surfaces.

Calculations were compared for inflow Mach numbers of 0.5 and 0.7. A comparison of the predicted cowl surface grid line Mach number distributions is given in Fig. 5.14. The 3D Euler results for both the inner and outer cowl surfaces display excellent agreement with the 2D Euler code results. A similar comparison is given in Fig. 5.15 for the 0.7 Mach number case. For this case, a strong symmetric shock wave pattern forms on the cowl surface, affording an examination of the shock-capturing characteristics of the cowl boundary algorithm. In this case, small discrepancies exist between the 2D solution, and the upper and lower surfaces of the 3D solution, although the agreement is still generally very good. The rapid decrease in Mach number across the shock wave is evident in each calculation. The small discrepancies between the solutions, and between the upper and lower surfaces of the 3D Euler solution, are easily explained by the differences in the mesh spacing near the cowl.

A similar comparison was performed for the multiple-block C-grid Euler solver. In this case, the five-block grid arrangement shown in Fig. 5.16 was generated for the numerical predictions. Again, the 91x21 2D grid is also displayed for comparison. The total number of grid points is roughly similar to the H-grid calculations with individual block sizes of (65x13x5), (16x13x5), (81x7x5), (16x13x5), and (65x14x5). A comparison of the predicted cowl surface grid line Mach number distribution from the 3D multiple-block C-grid Euler analysis and the 2D solution for an inflow Mach number of 0.5 is given in Fig. 5.17. Again, good agreement is observed between the 3D and 2D results. A second comparison of results is given for an inflow Mach number of 0.7 in Fig. 5.18. Again, the predicted Mach number distributions are in

good agreement, and the effect of the shock which results from the higher inflow Mach number is clearly displayed. Static pressure contour plots for the axisymmetric plane projection of the 3D H-grid and multiple-block C-grid Euler results for the 0.7 inflow Mach number case are given in Fig. 5.19. The individual block boundaries are outlined in this case to demonstrate the smooth transition of contour lines across the block interfaces. The H-grid and multiple-block C-grid results are very similar in spite of the differences in the solution technique. The asymmetry of the contour lines is a result of the differences in boundary conditions at the hub and outer boundaries. This figure serves to validate the accuracy of the block coupling procedure and indicates that no nonphysical behavior is introduced by this procedure.

5.4 Ducted SR7 Demonstration

An interesting comparison of results was based on the calculation of the flowfield about a fictitious ducted 8-bladed SR7 propfan. In spite of the fact that there are no experimental data for this configuration, these calculations were useful for preliminary debugging of the analysis for ducted configurations, and also provided an opportunity to compare the predicted Euler results with an existing frequency domain panel method also developed for ducted propfan flows.

The geometry was based on the original 8-bladed SR7 geometry given in Section 4.1 with a thin profile duct about the propeller. A relatively large tip gap (2% of the duct diameter) was imposed to permit an examination of the tip flow.

The geometry and grid surfaces are shown in Fig. 5.20. The axisymmetric projection of the 69x45x15 H-grid generated for this case is illustrated in Fig. 5.21. The

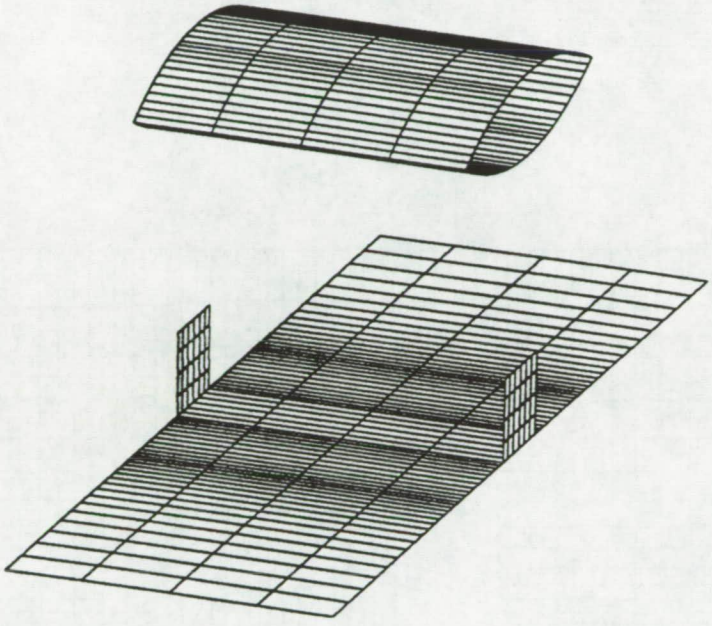

Figure 5.12: Symmetric double circular arc cowl ducted propeller test case geometry

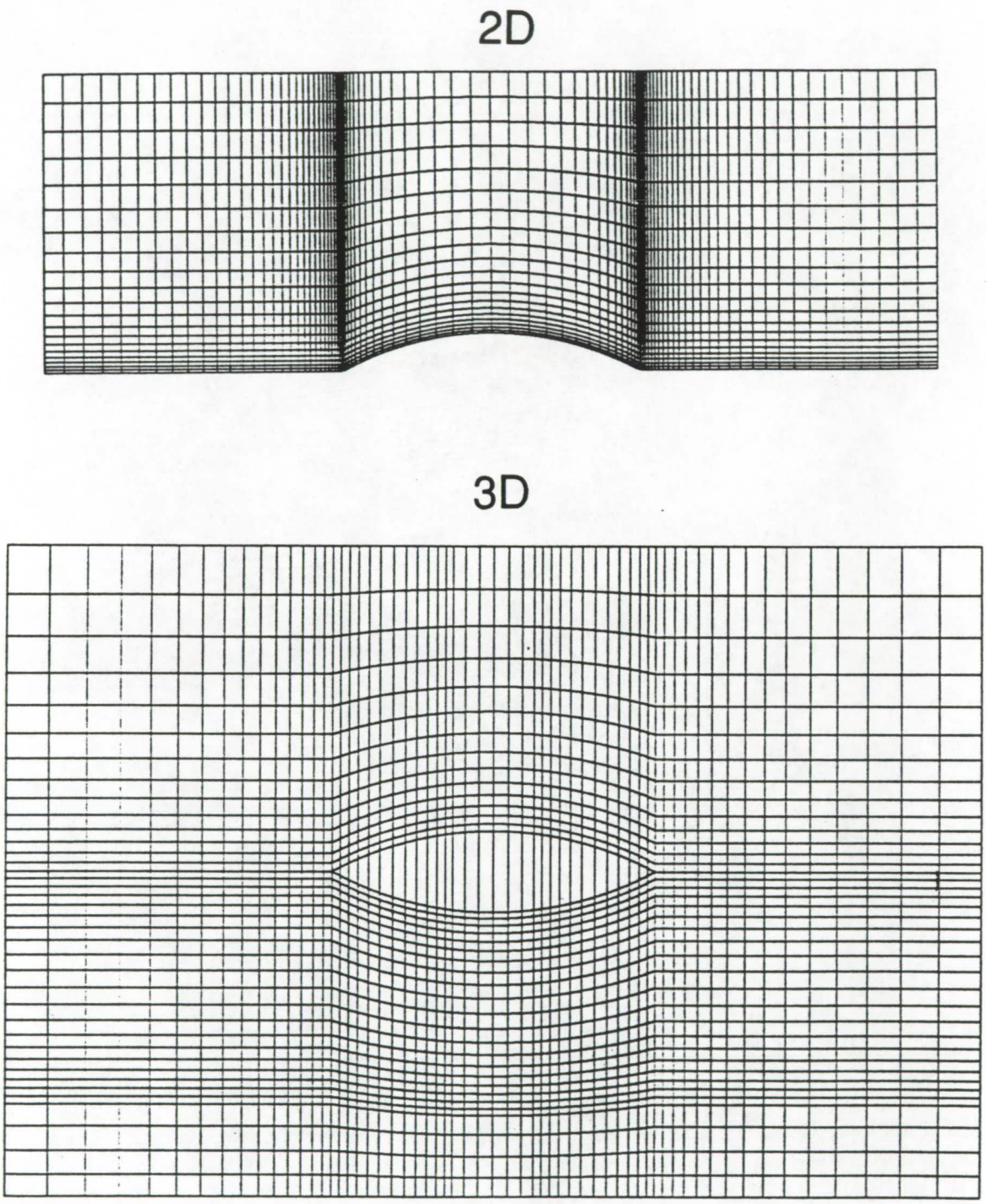

Figure 5.13: Comparison of 91x21 2D grid and axisymmetric plane projection of 91x42x5 3D H-grid for the symmetric double circular arc cowl test case

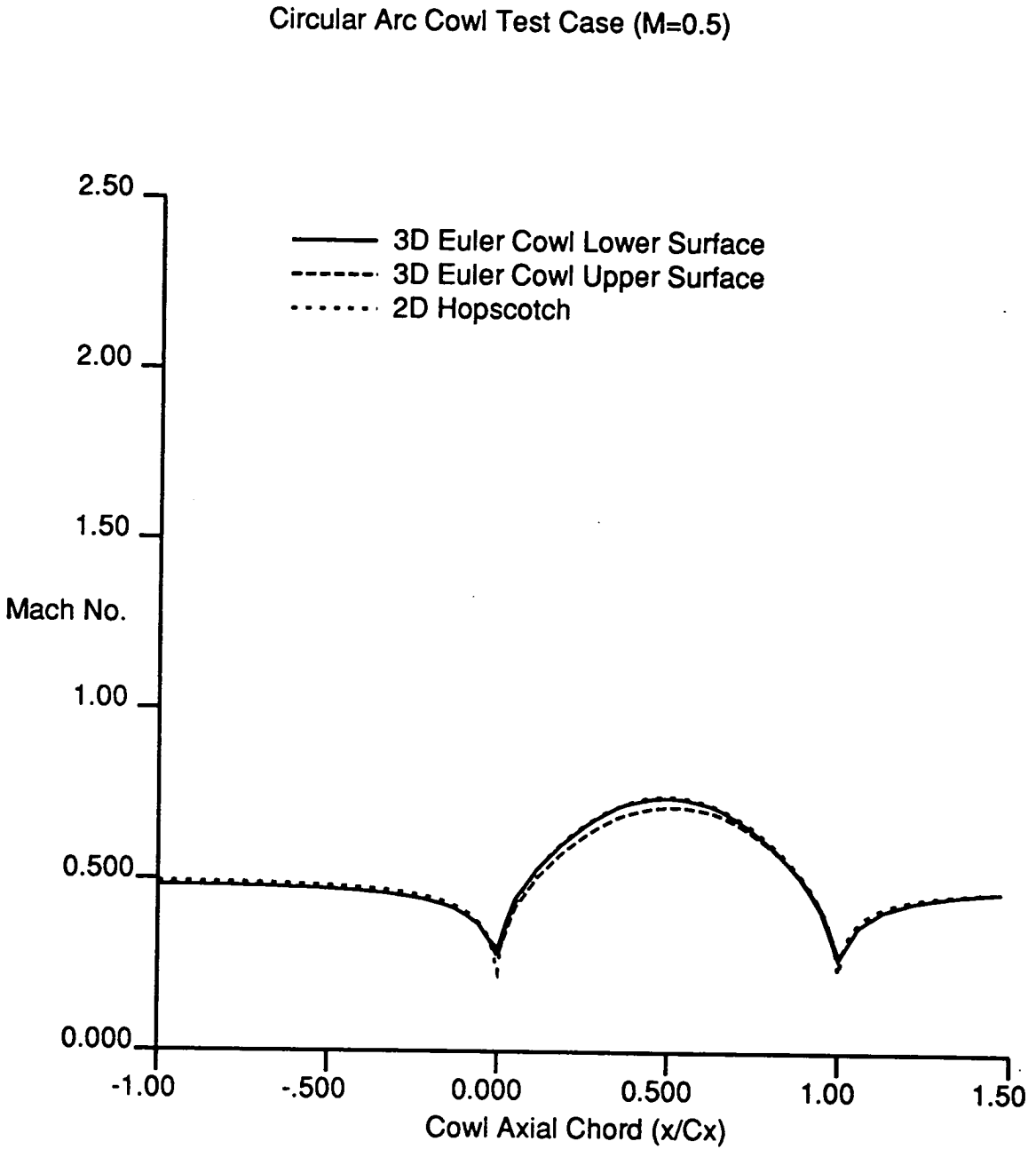

Figure 5.14: Comparison of 2D and 3D H-grid predicted cowl surface grid line Mach number distributions (M=0.5)

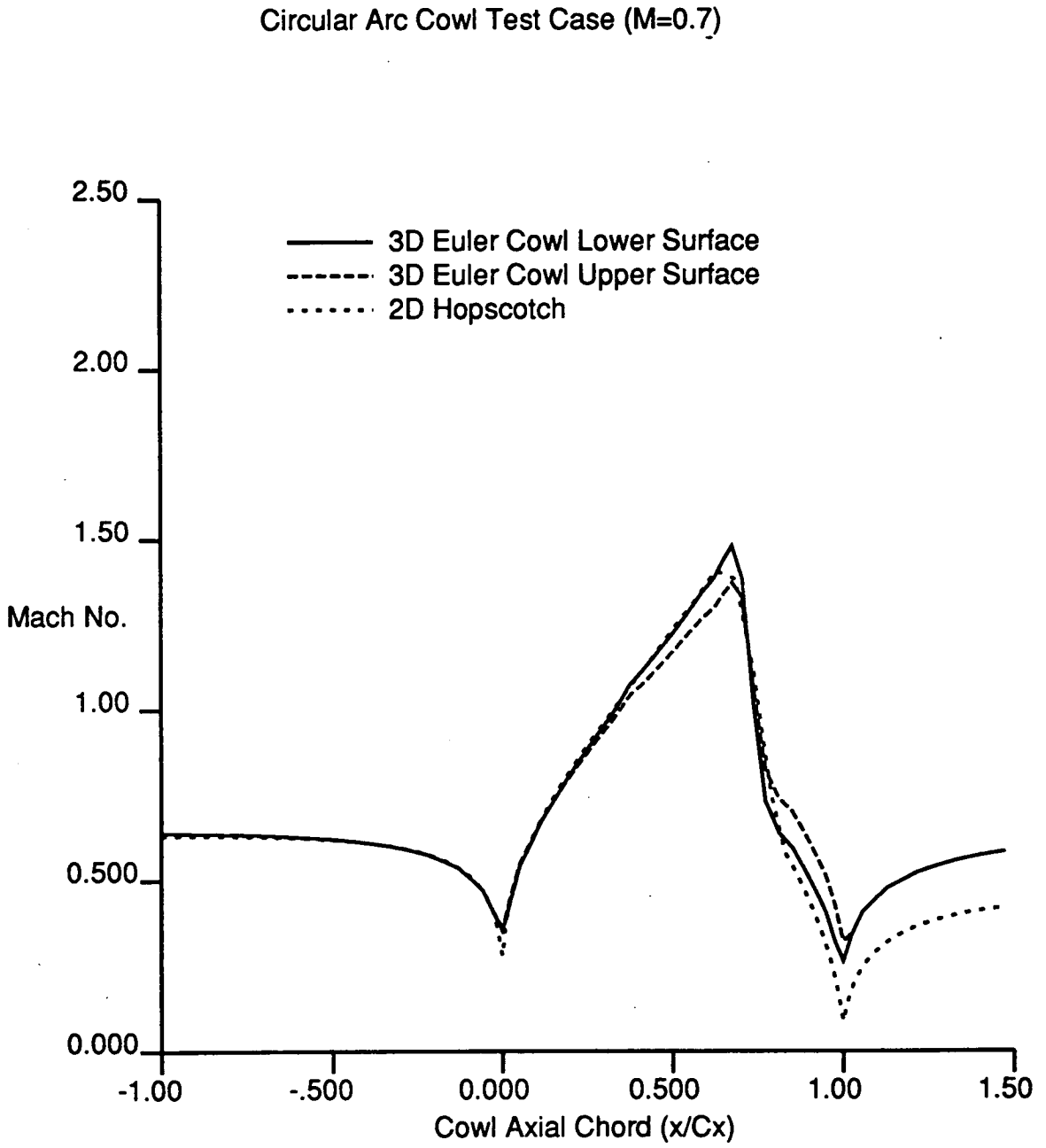

Figure 5.15: Comparison of 2D and 3D H-grid predicted cowl surface grid line Mach number distributions (M=0.7)

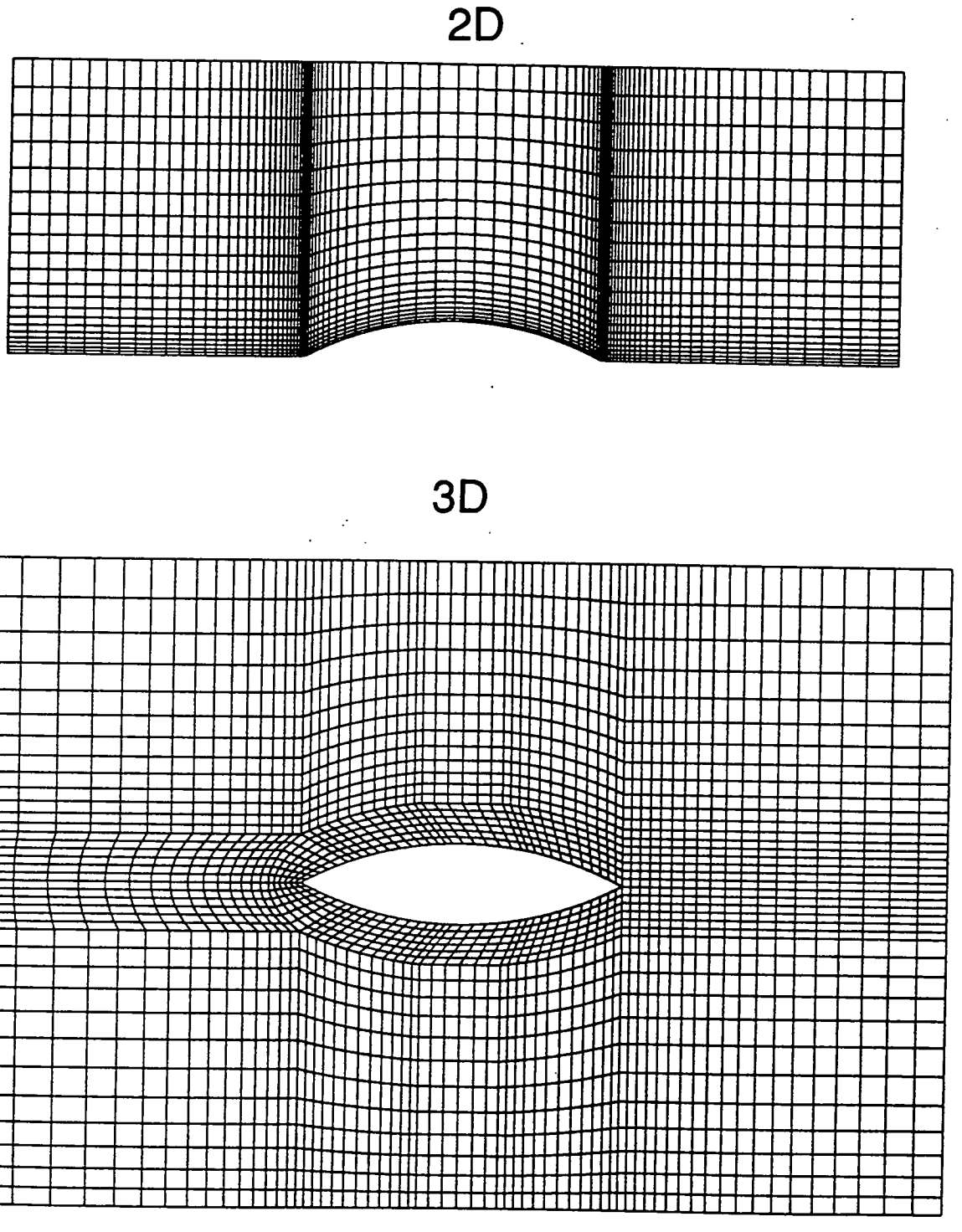

Figure 5.16: Comparison of 91x21 2D grid and axisymmetric plane projection of multiple-block C-grid for the symmetric double circular arc cowl test case

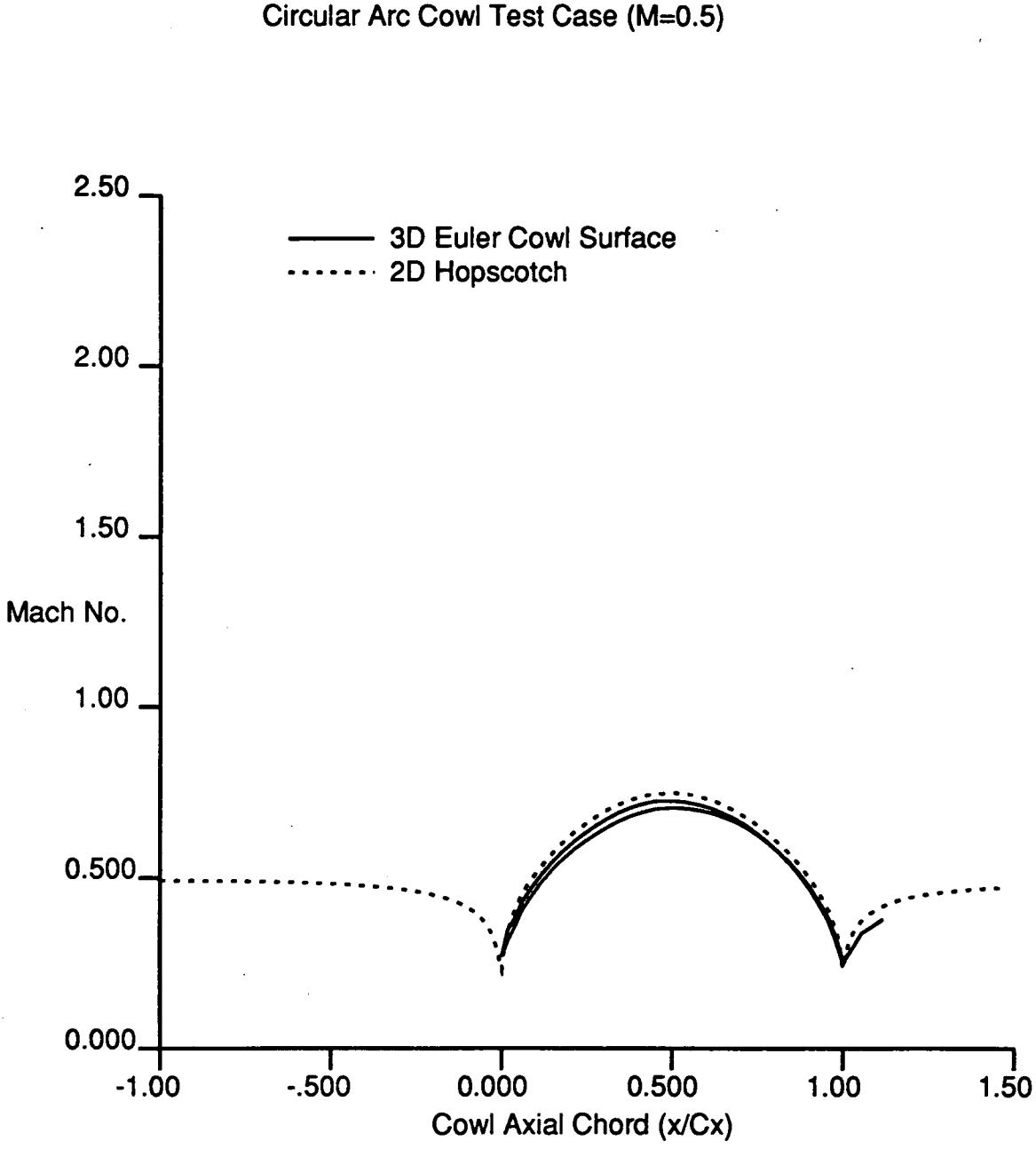

Figure 5.17: Comparison of 2D and 3D multiple-block C-grid predicted cowl surface grid line Mach number distributions (M=0.5)

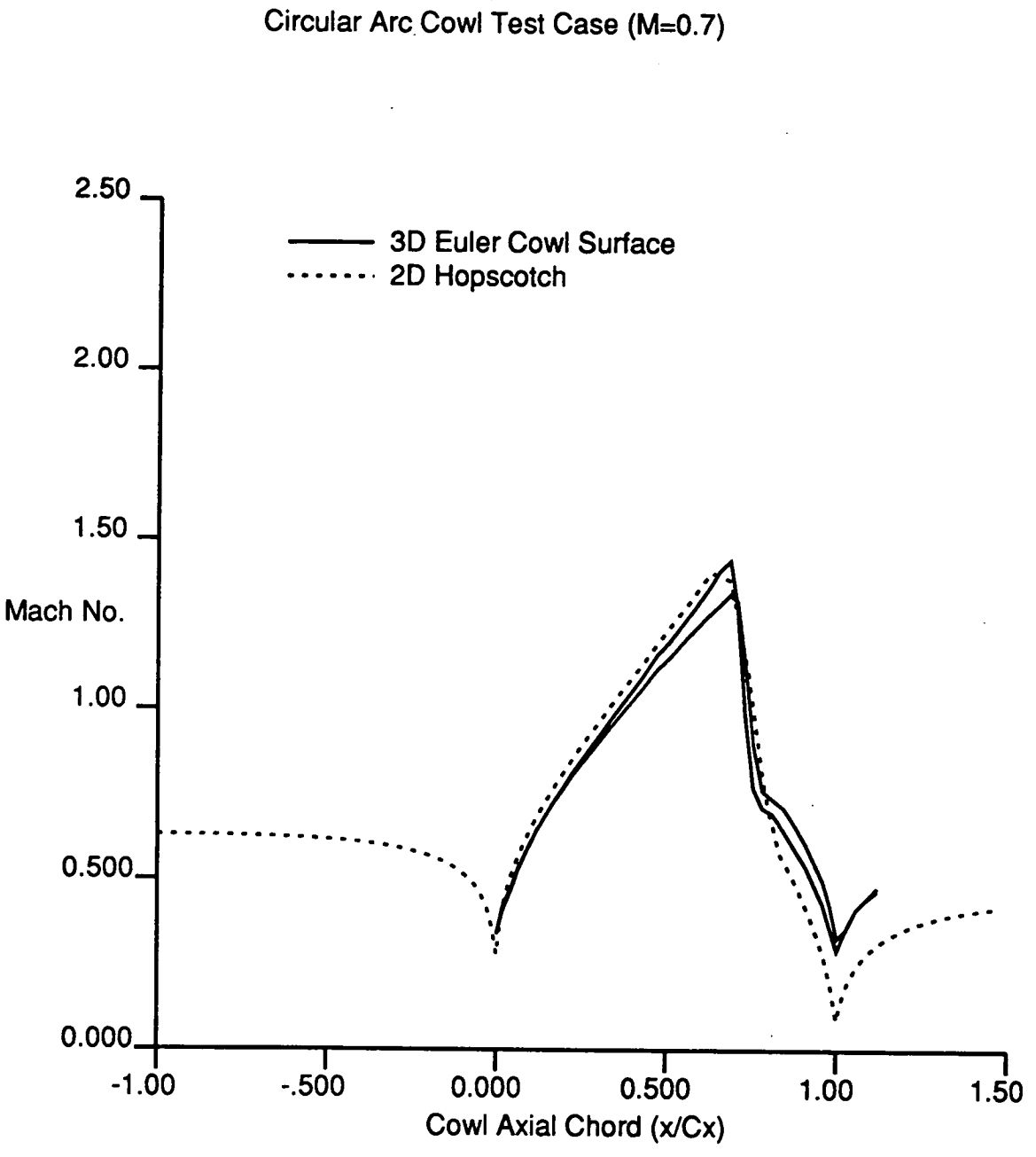

Figure 5.18: Comparison of 2D and 3D multiple-block C-grid predicted cowl surface grid line Mach number distributions (M=0.7)

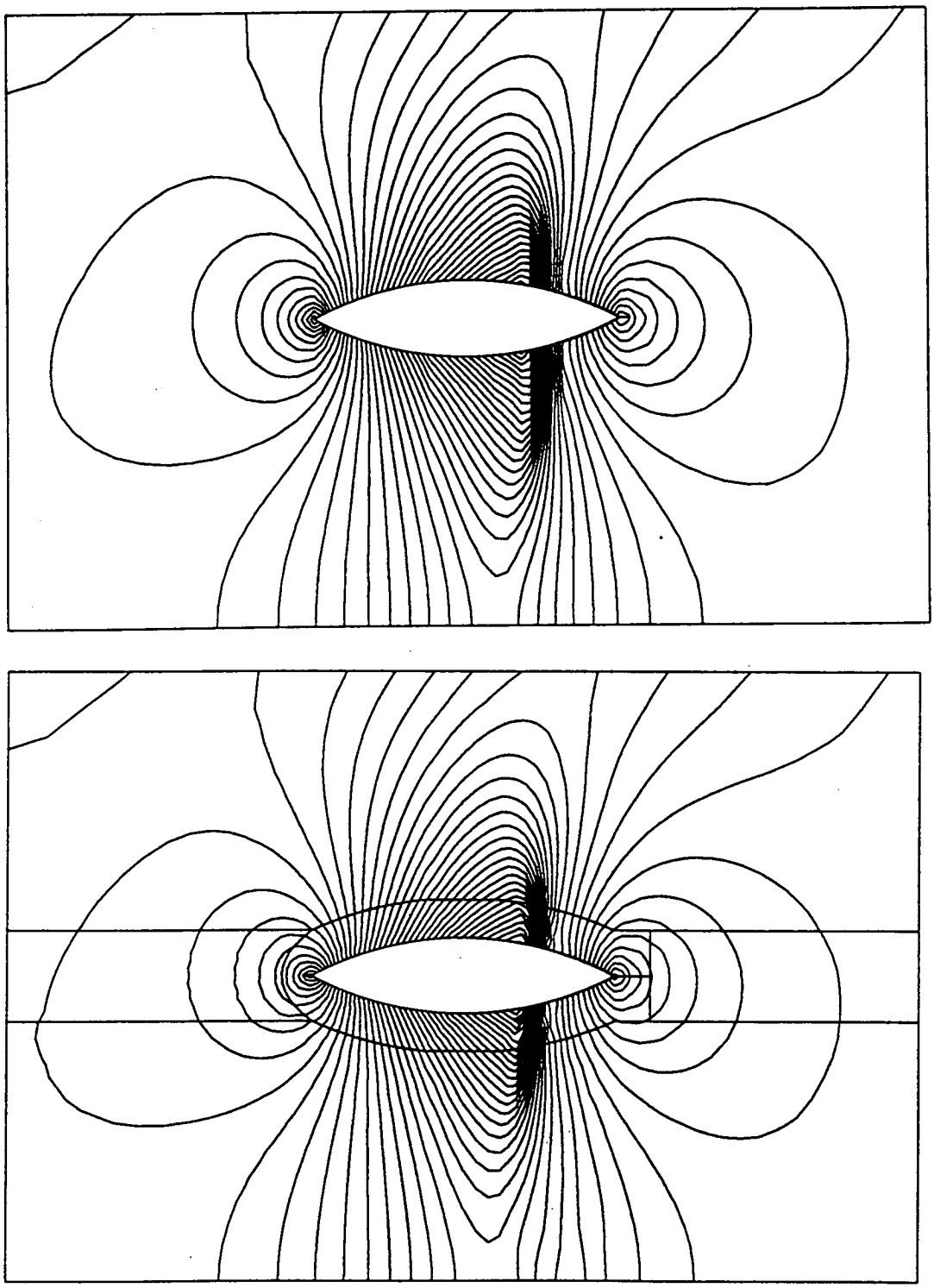

Figure 5.19: Comparison of the predicted static pressure contours for the axisymmetric plane projection of the 3D H-grid (top) and multiple-block C-grid (bottom) Euler analyses of the symmetric double circular arc cowl test case (M=0.7)

case tested was for a true 3/4 blade setting angle of 60.2 degrees, flight Mach number of 0.7, and an advance ratio of 3.06. Predicted results from the 3D Euler code were compared with predicted results from a frequency domain panel code developed for ducted propellers by Williams et al. [25]. A comparison of the predicted airfoil spanwise elemental power coefficient loading distributions is given in Fig. 5.22 for this case. A similar comparison is given for the predicted airfoil spanwise elemental thrust coefficient loading distributions in Fig. 5.23. The predicted power and thrust coefficient loading distributions for the unducted case are also given in Figs. 5.22-5.23 for comparison. Unfortunately, the panel code does not accurately model the hub and cowl contour; however, the loading distributions are largely similar, although the Euler code predicts a somewhat larger aerodynamic loading near the blade tip region. The predicted propfan surface static pressure contours for the 3D Euler results are pictured in Fig. 5.24. The effect of adding the duct to the normally unducted blade is immediately evident in the predicted results. The ducted blade becomes highly loaded at the tip, and generates a rather strong shock which extends to the inner duct surface. The spanwise loading indicates that the addition of the duct results in a 30% increase in thrust and a 25% increase in power.

A second 3D solution was performed for this geometry using the multiple-block C-grid Euler analysis. In this case, the block grid pictured in Fig. 5.25 was utilized. The individual grid blocks contained (69x21x15), (11x9x15), (103x5x15), (12x9x15), and (69x18x15) points, respectively. Again, the predicted results were compared to the frequency-domain panel method of Williams et al. [25]. A comparison of the predicted airfoil spanwise elemental power coefficient loading distributions is given in

Fig. 5.26 for this case. A similar comparison is given for the predicted airfoil spanwise elemental thrust coefficient loading distributions in Fig. 5.27. The results exhibited by the multiple-block C-grid Euler analysis are largely similar to the H-grid Euler analysis results.

5.5 Low Speed Ducted Propeller

The third ducted configuration tested was based on the low speed ducted propeller originally tested by Kruger [26]. Kruger's geometry was based on an axisymmetric elliptical centerbody with an 8-bladed NACA 23009-23012 (hub to tip) section propeller. Data were taken for the static pressure distributions on the centerbody and cowl surfaces.

A 160x41x15 grid was generated for this geometry, as shown in Fig. 5.28. The axisymmetric projection of this grid is given in Fig. 5.29. The case presented corresponds to Kruger's cowl #1, propeller #1, and nacelle #1. The calculation was based on an advance ratio of 0.95 and a flight Mach number of 0.4275. This experimental arrangement was particularly convenient for numerical simulation since the duct was supported separately from the centerbody, and thus mounting struts which might cause aerodynamic interference were not required.

A comparison of the H-grid predicted and experimental cowl surface static pressure coefficient distributions is given in Fig. 5.30. The somewhat jagged appearance of the computational results is due to a lack of smoothness in the coordinates used to define Kruger's cowl geometry (the cowl coordinates were obtained by manually digitizing a drawing of the cowl cross section). In spite of the crudeness of the geometric

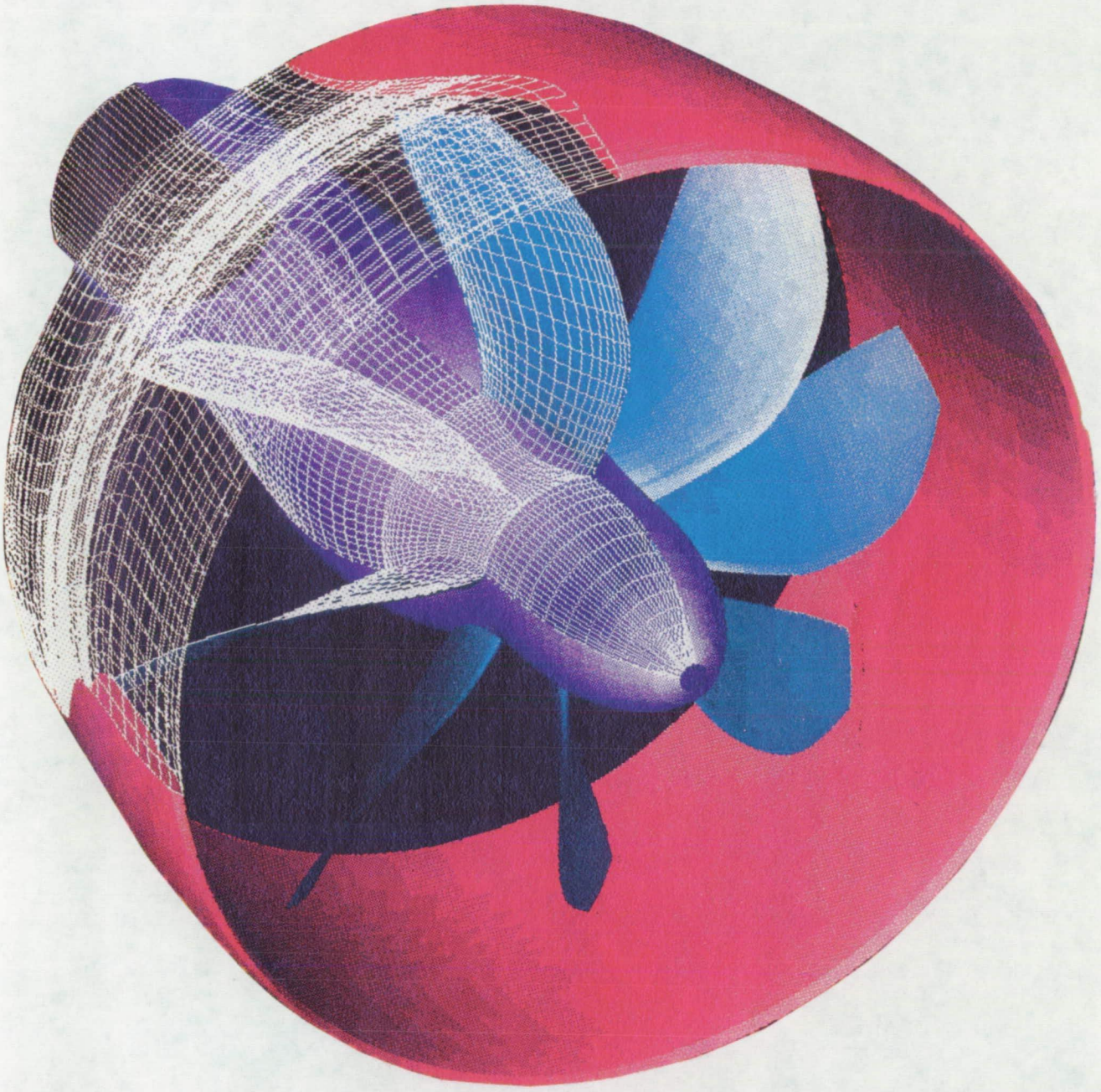

Figure 5.20: Ducted 8-bladed SR7 geometry and 69x45x15 H-grid

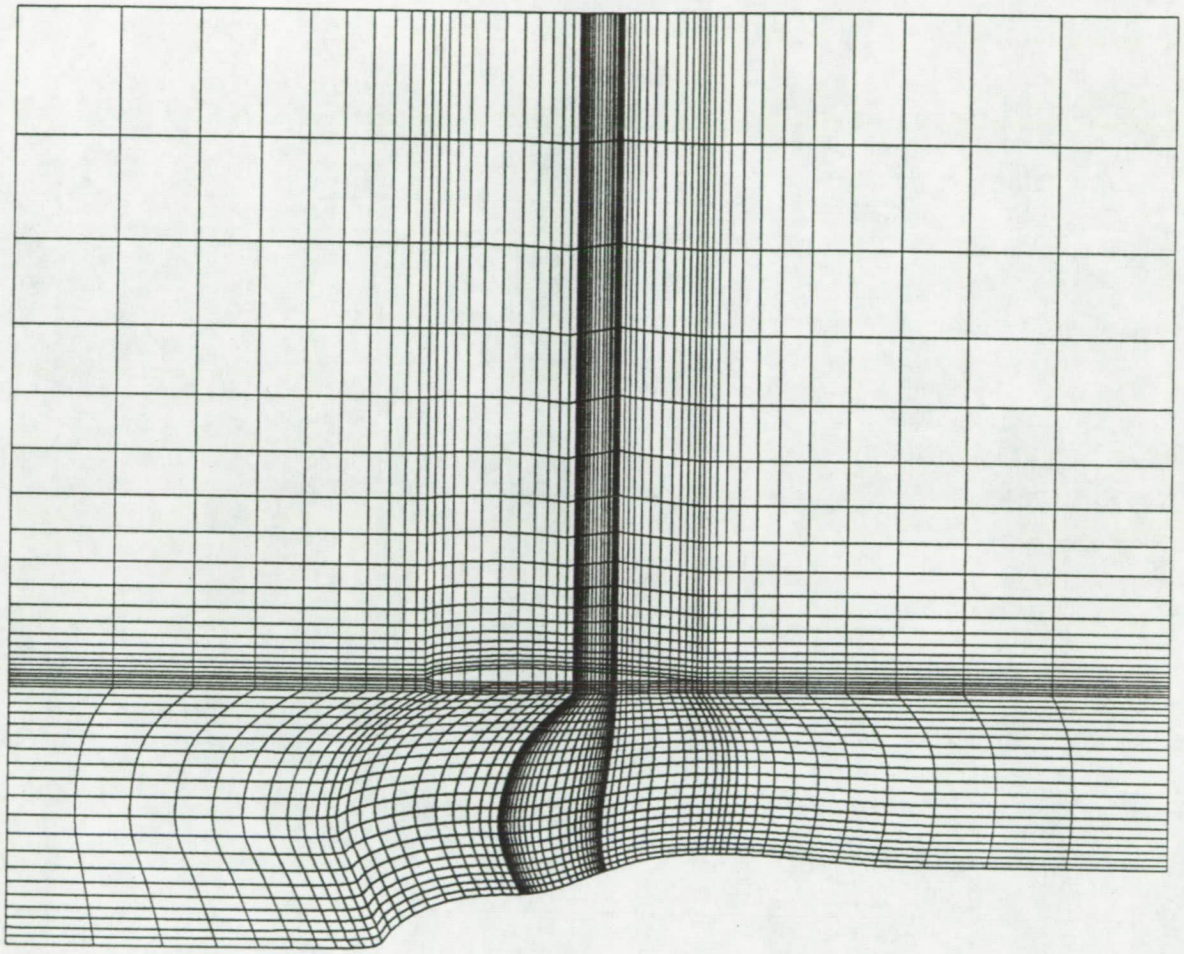

Figure 5.21: Axisymmetric plane projection of 69x45x15 H-grid for ducted SR7 propfan

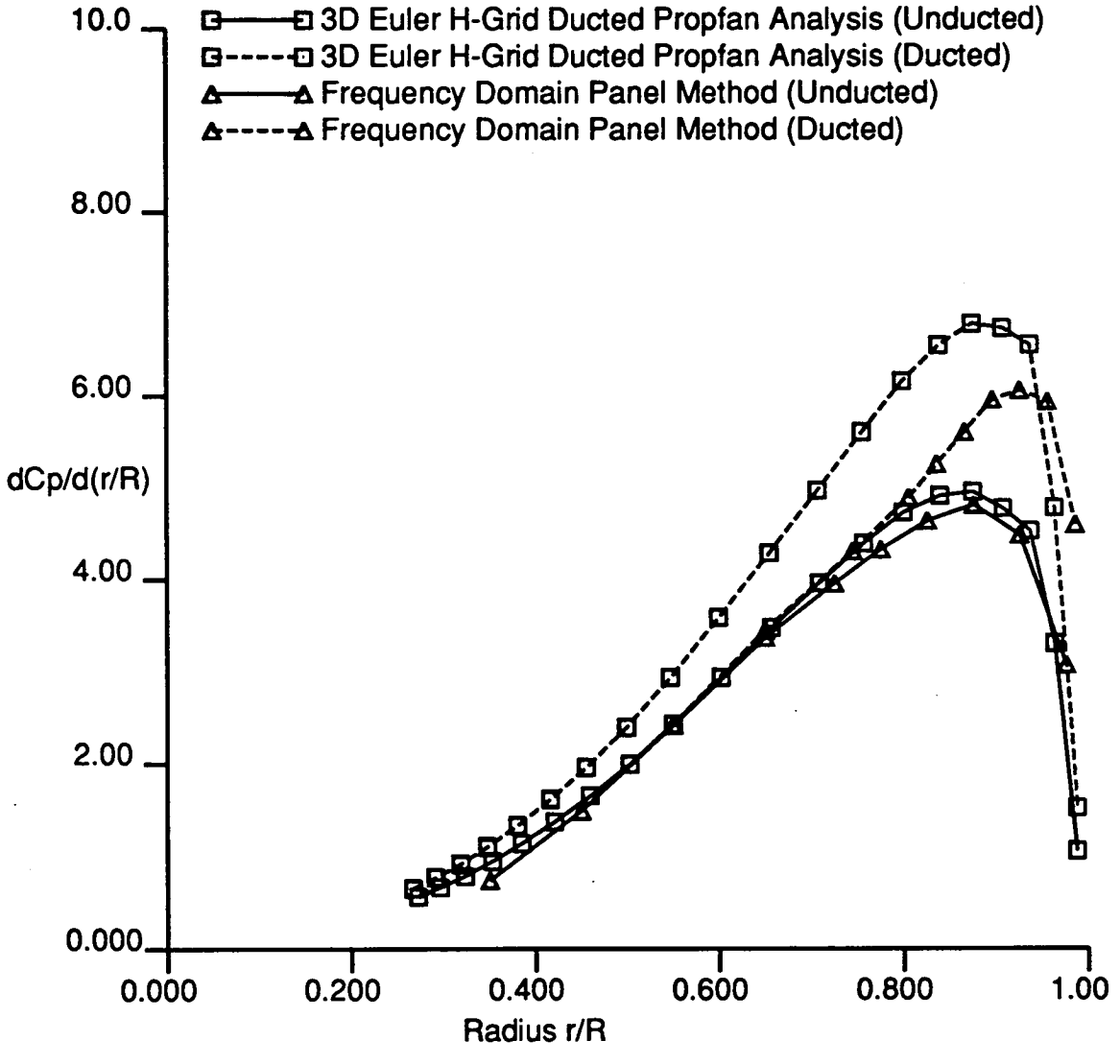

Figure 5.22: Comparison of H-grid predicted elemental blade power coefficient distribution with frequency domain panel method results for ducted 8-bladed SR7

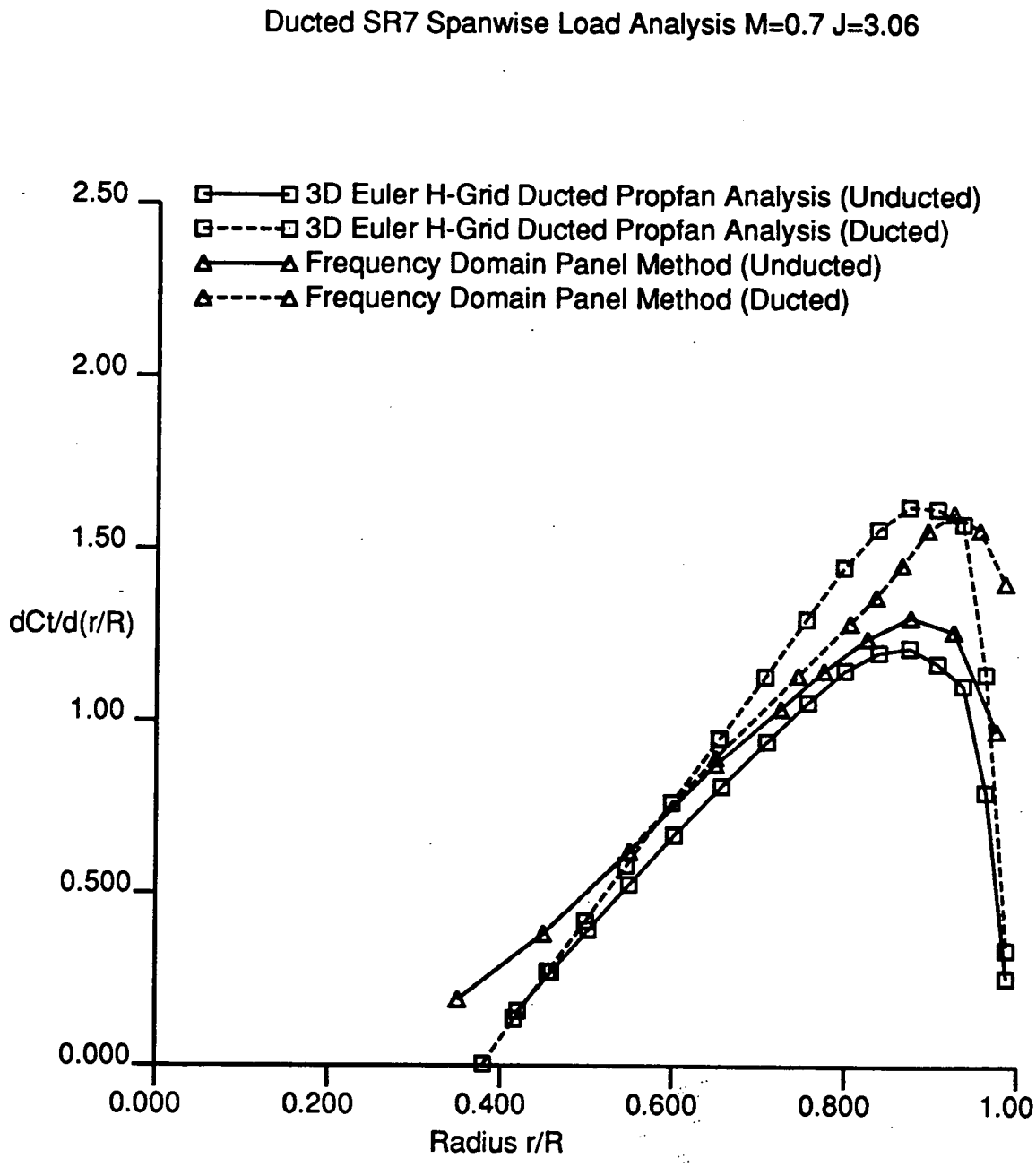

Figure 5.23: Comparison of H-grid predicted blade elemental thrust coefficient distributions with frequency domain panel method results for ducted 8-bladed SR7

Figure 5.24: Predicted H-grid propfan surface static/total pressure ratio contours for ducted SR7

Figure 5.25: Axisymmetric plane projection of multiple-block C-grid for ducted SR7 propfan

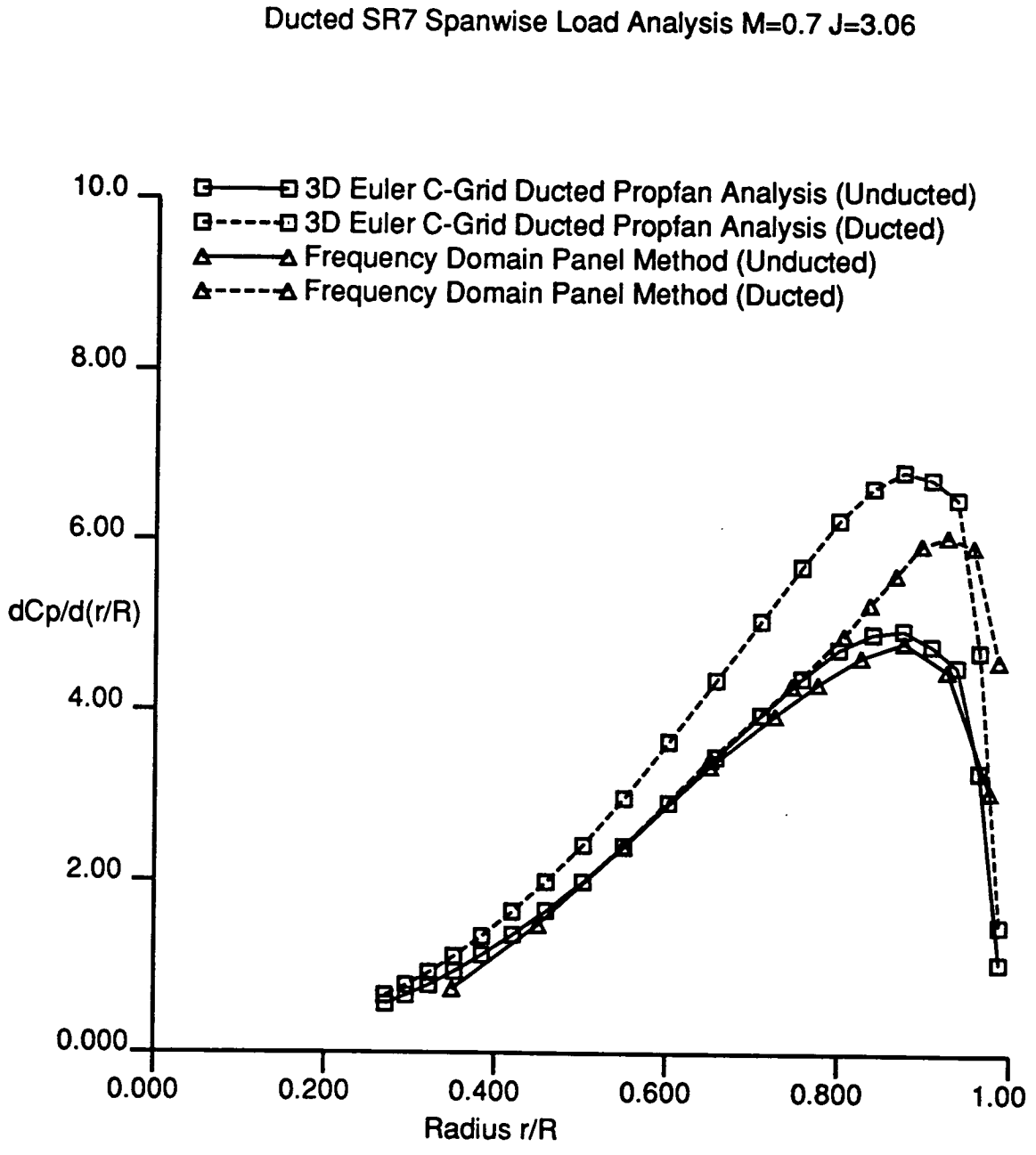

Figure 5.26: Comparison of multiple-block C-grid predicted elemental blade power coefficient distribution with frequency domain panel method results for ducted 8-bladed SR7

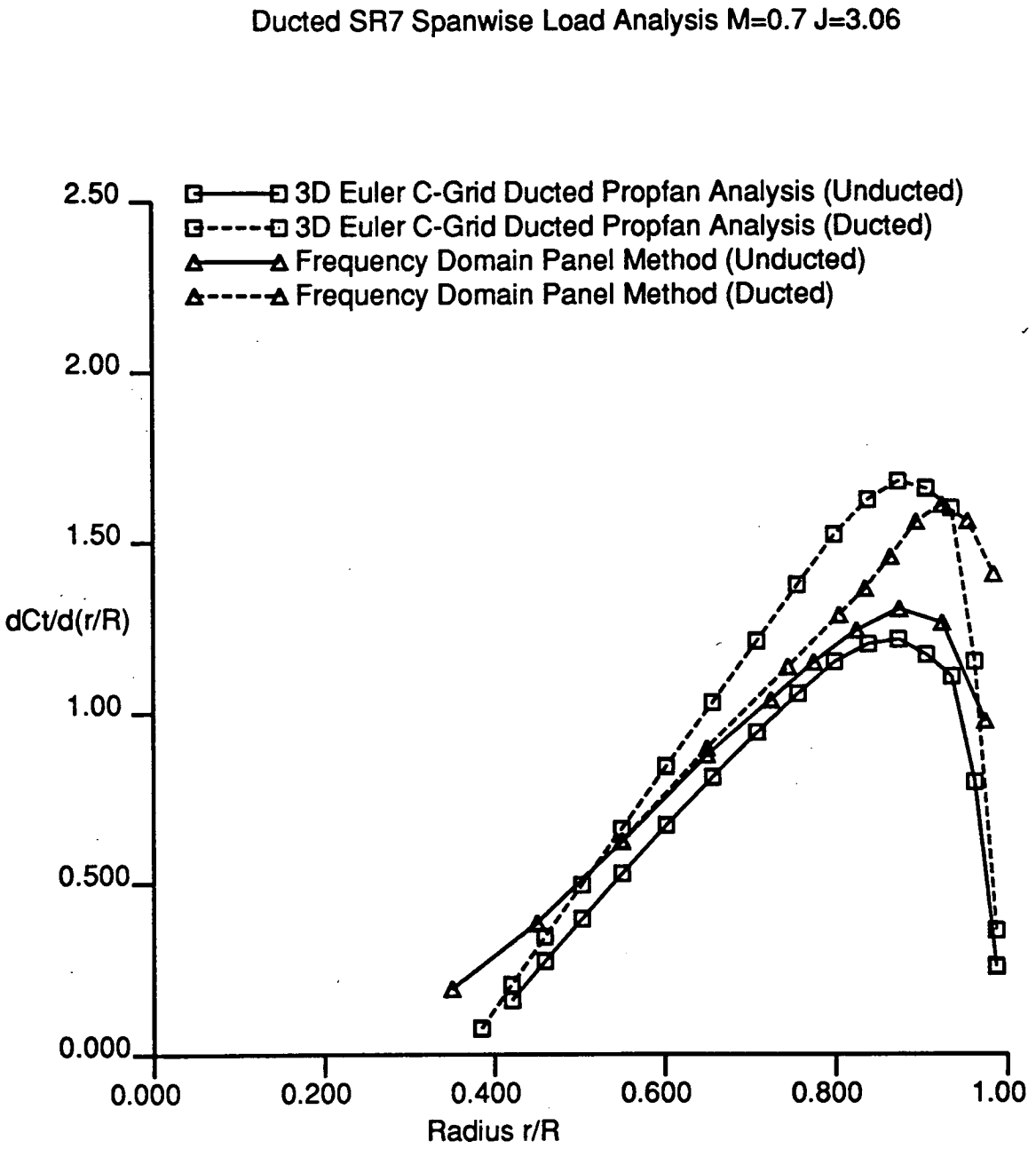

Figure 5.27: Comparison of multiple-block C-grid predicted blade elemental thrust coefficient distributions with frequency domain panel method results for ducted 8-bladed SR7

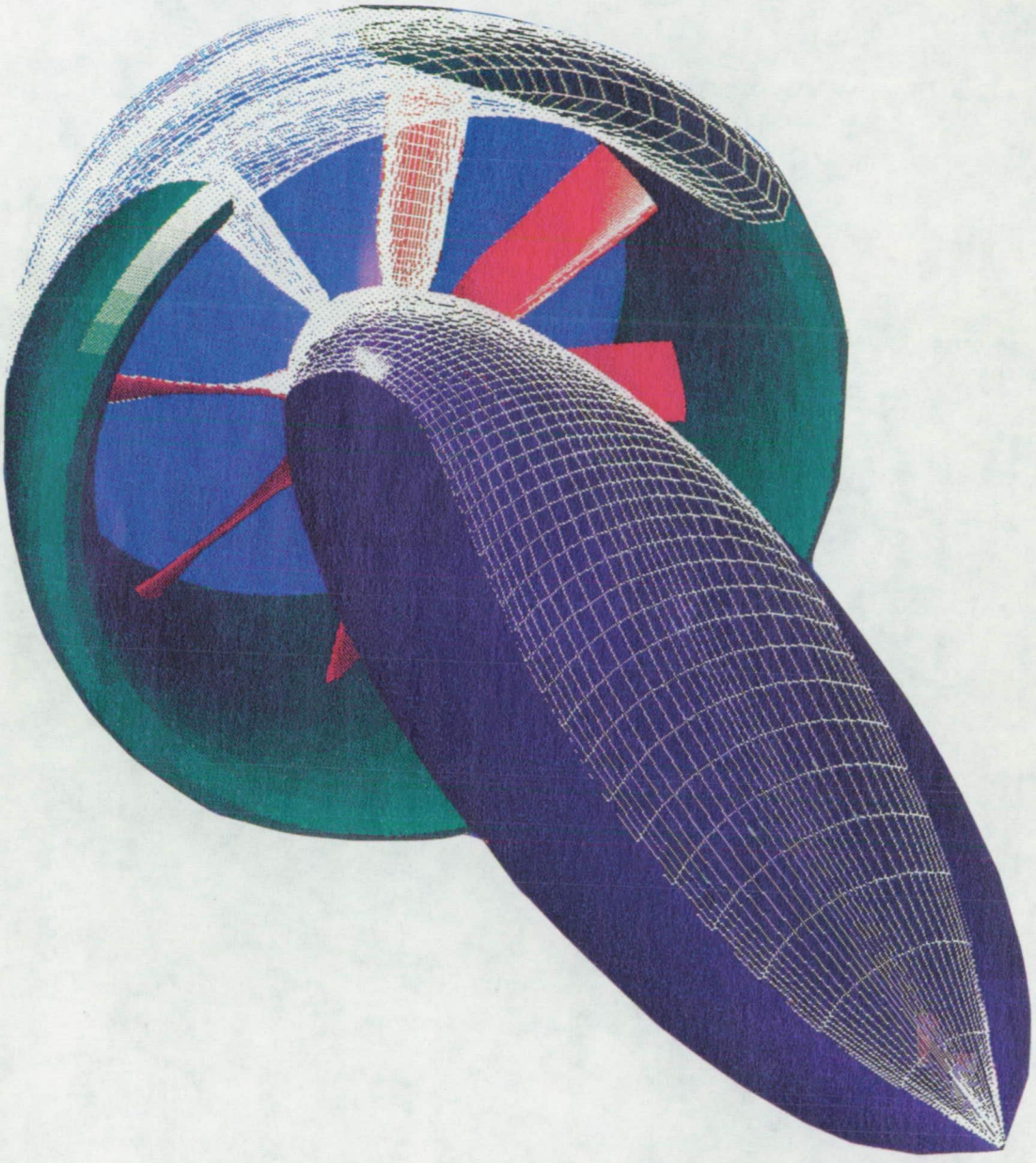

Figure 5.28: Geometry and 127x48x15 grid for Kruger low speed ducted propeller

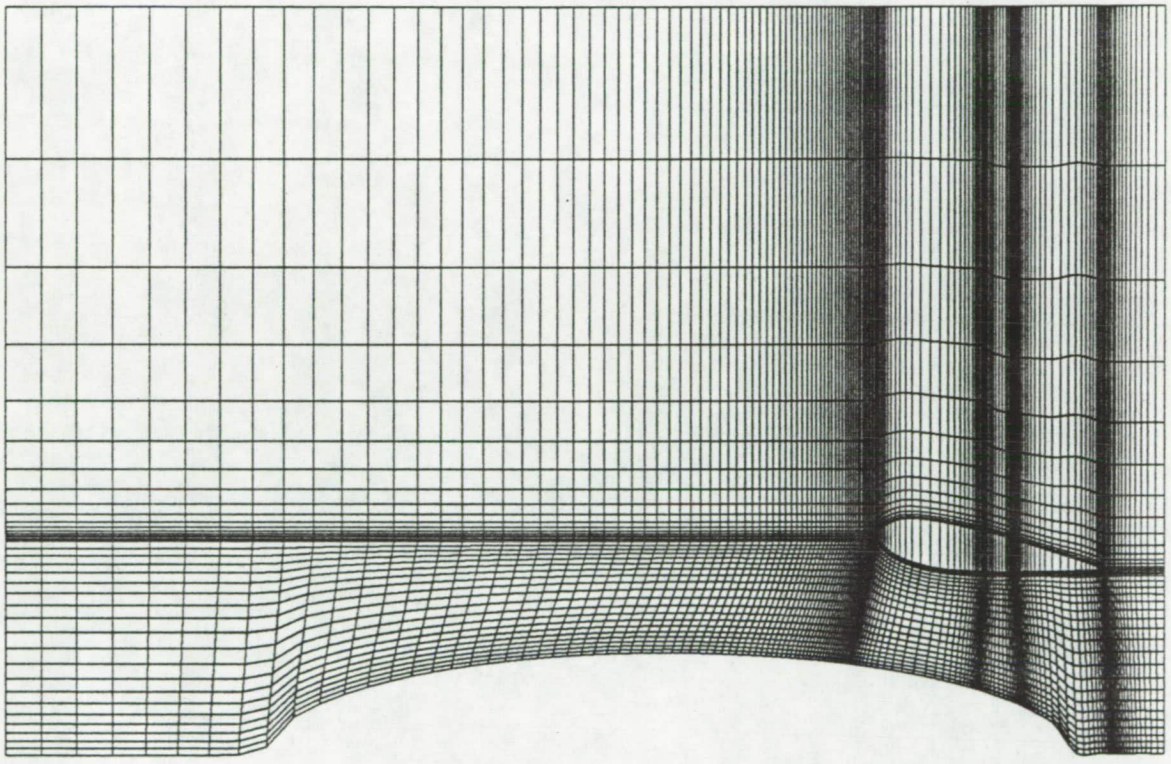

Figure 5.29: Axisymmetric plane projection of 127x48x15 H-grid for Kruger low speed ducted propeller

model, good agreement was obtained with the experimental data.

A second calculation was performed for this case using the 3D multiple-block C-grid Euler analysis. The axisymmetric plane projection of the calculation grid is given in Fig. 5.31. The respective grid block sizes for this calculations were (150x21x15), (65x13x15), (147x7x15), (19x13x15), and (150x15x15). Again, a comparison of the multiple-block C-grid predicted and experimental cowl surface local static pressure coefficient distributions is given in Fig. 5.32. A similar level of agreement was obtained from the multiple-block C-grid calculation, in spite of the geometric uncertainties.

5.6 NASA 1.15 Pressure Ratio Fan

Final calculations were performed for a 1.15 pressure ratio fan stage originally tested at NASA for a wide range of flows [27]-[30]. A description of the geometry is given in Fig. 5.33. This geometry is representative of a 25:1 bypass ratio turbofan engine fan stage. Both single-rotation and counter-rotation calculations were performed for this geometry. For each calculation, it was not possible to exactly match the experimentally measured mass flow through the fan due to the expense of iterating on the three-dimensional solution; therefore, predictions are based on the flight Mach number and estimated fan rotational speed alone. A three-dimensional view of the geometry and grid system overlay are given in Fig. 5.34.

H-grid predictions were based on the 225x52x15 H-grid pictured in the axisymmetric plane projection given in Fig. 5.35. The blades were represented by 23 points in the axial direction and 21 points in the radial direction. Both blade rows are represented in the axisymmetric projection of the grid. Single-rotation calculations were

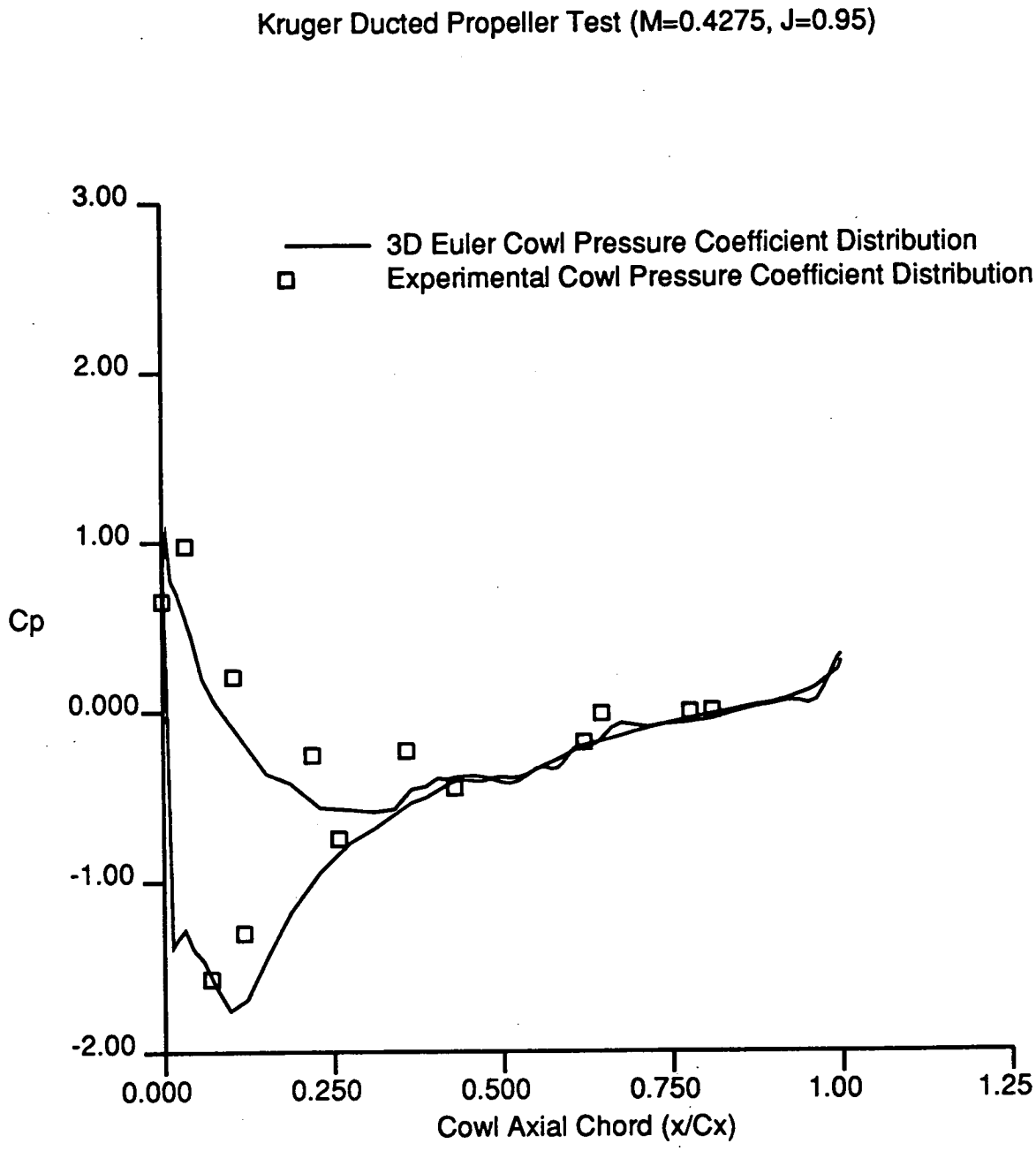

Figure 5.30: Comparison of H-grid predicted and experimental cowl surface static pressure coefficient distributions for Kruger low speed propeller

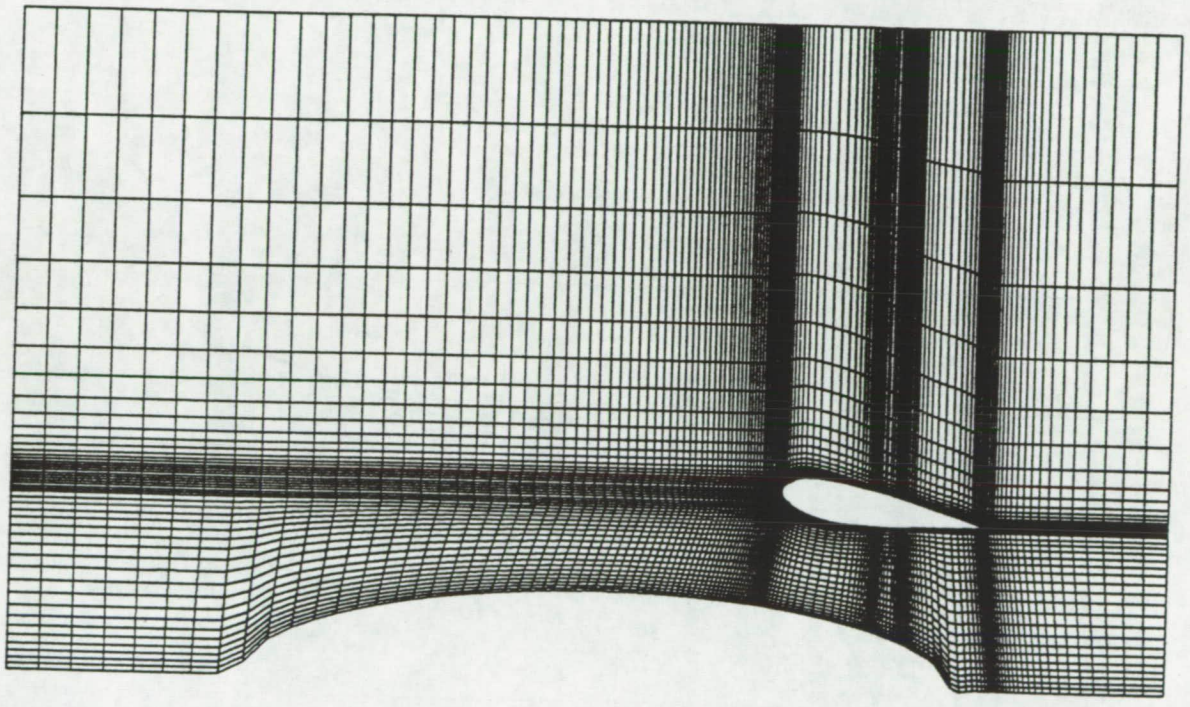

Figure 5.31: Axisymmetric plane projection of multiple-block C-grid for Kruger low speed ducted propeller

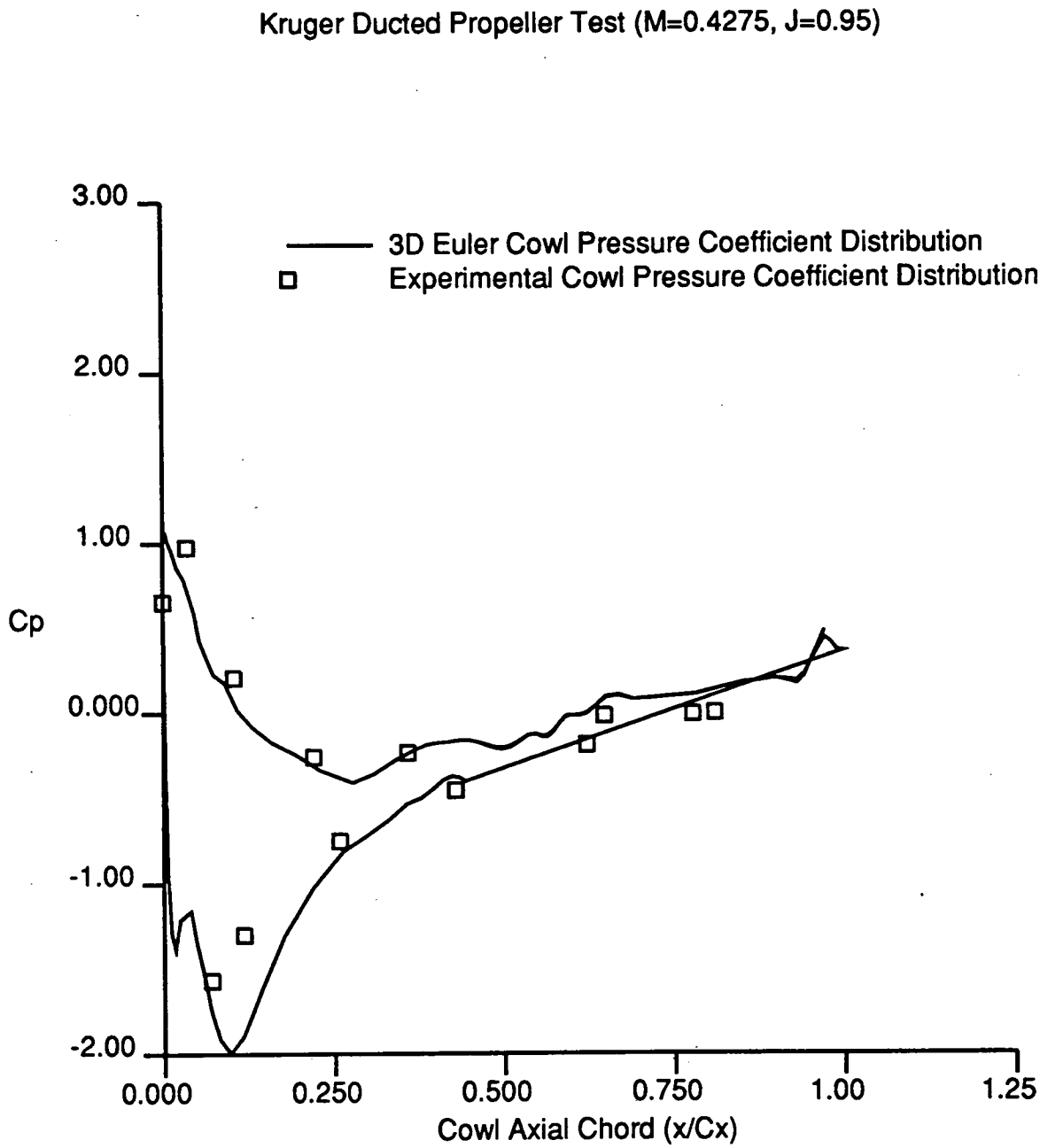

Figure 5.32: Comparison of multiple-block C-grid predicted and experimental cowl surface static pressure coefficient distributions for Kruger low speed propeller

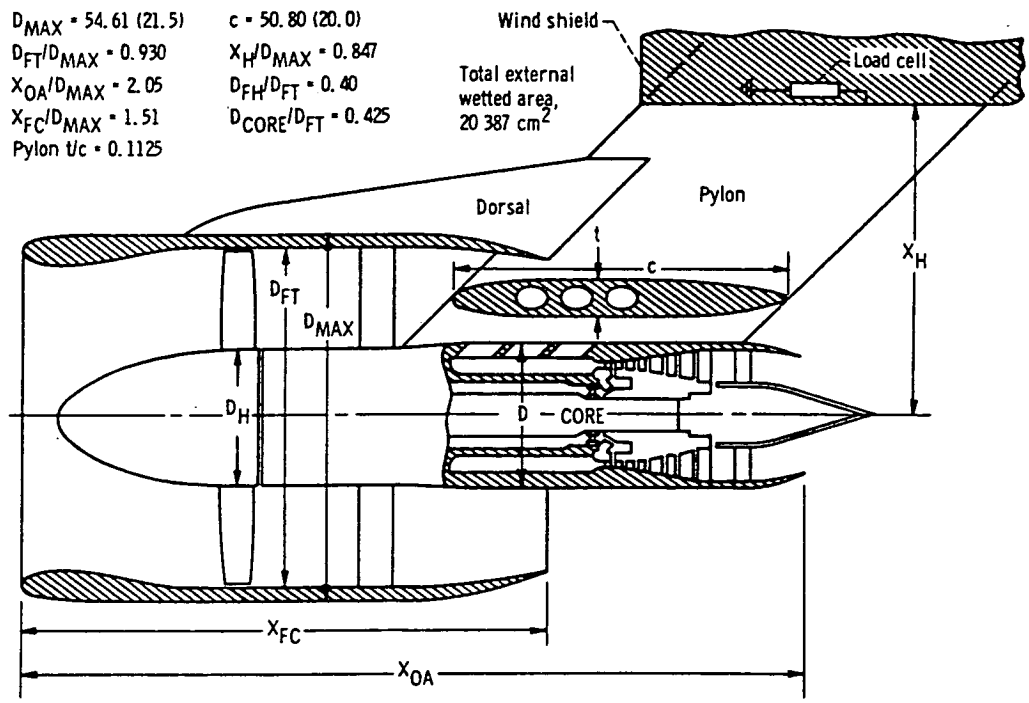

Figure 5.33: NASA 1.15 pressure ratio fan stage geometry (dimensions in cm)

C-2

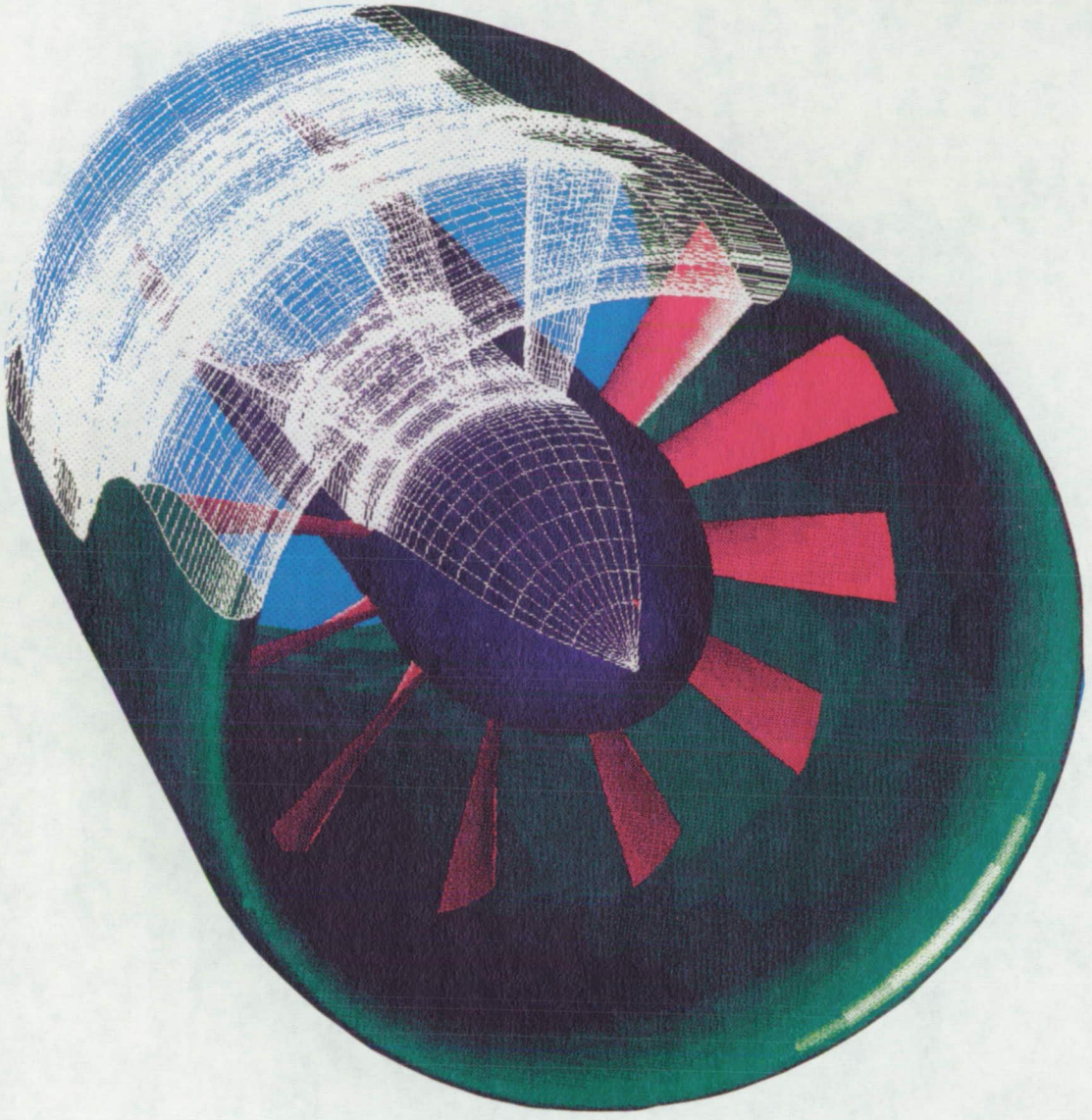

Figure 5.34: NASA 1.15 pressure ratio fan stage and 3D grid overlay

performed by neglecting the thickness of the deswirl vanes.

For the initial calculations, only the single-rotation rotor was modelled. A comparison of predicted and experimental cowl leading edge surface static pressure coefficient distributions for a flight Mach number of 0.75 and an advance ratio (J) of 2.86 for the rotor alone is given in Fig. 5.36. The data are presented in an unwrapped form to expand the critical region of interest at the cowl leading edge. The agreement between prediction and experiment is outstanding. Each of the features of the experimental pressure distribution is well defined by the predicted results. Any discrepancies between experiment and prediction are thought to be due to small differences between the predicted and experimentally measured mass flow rate through the fan or grid inadequacies. A similar comparison of results is given in Fig. 5.37 for a flight Mach number of 0.85 and an advance ratio of 3.23. In this case, good agreement is observed over much of the cowl surface, except for a rather large discrepancy on the outer cowl surface downstream of the leading edge region. Experimental evidence indicates that a flow separation occurs for the outer cowl surface in this case, and the disagreement is a result of the inviscid flow assumption in the present analysis. This would suggest that a viscous flow analysis will ultimately be required for high speed ducted fan design and off-design analysis.

In order to assess the impact of the deswirl vanes on the aerodynamic solution, the 0.75 Mach number solution was repeated for a counter-rotation configuration using the average-passage approach. This demonstration was performed under a no-cost contract amendment to verify the average-passage formulation in the ducted propfan Euler solver. The solution procedure involves iteratively updating representative body

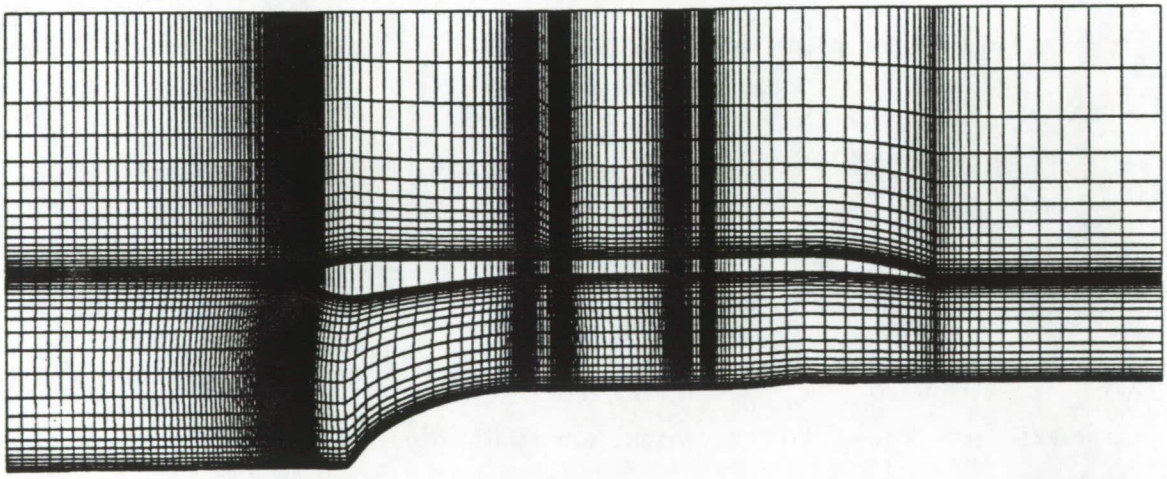

Figure 5.35: Axisymmetric plane projection of NASA 1.15 pressure ratio fan stage 225x52x15 H-grid

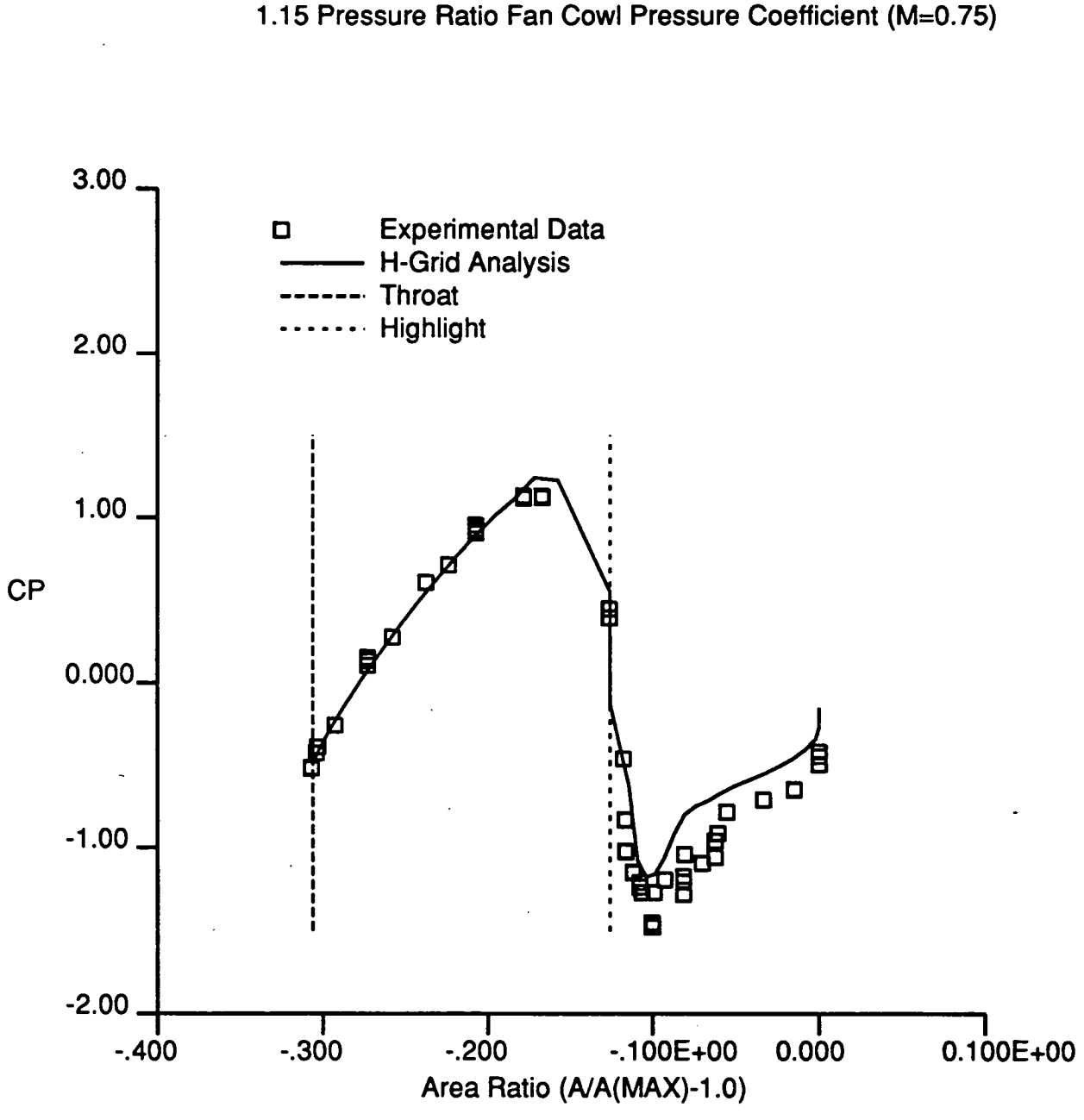

Figure 5.36: Comparison of predicted and experimental cowl leading edge static pressure coefficient distributions for NASA 1.15 pressure ratio fan (H-grid, rotor only, M=0.75)

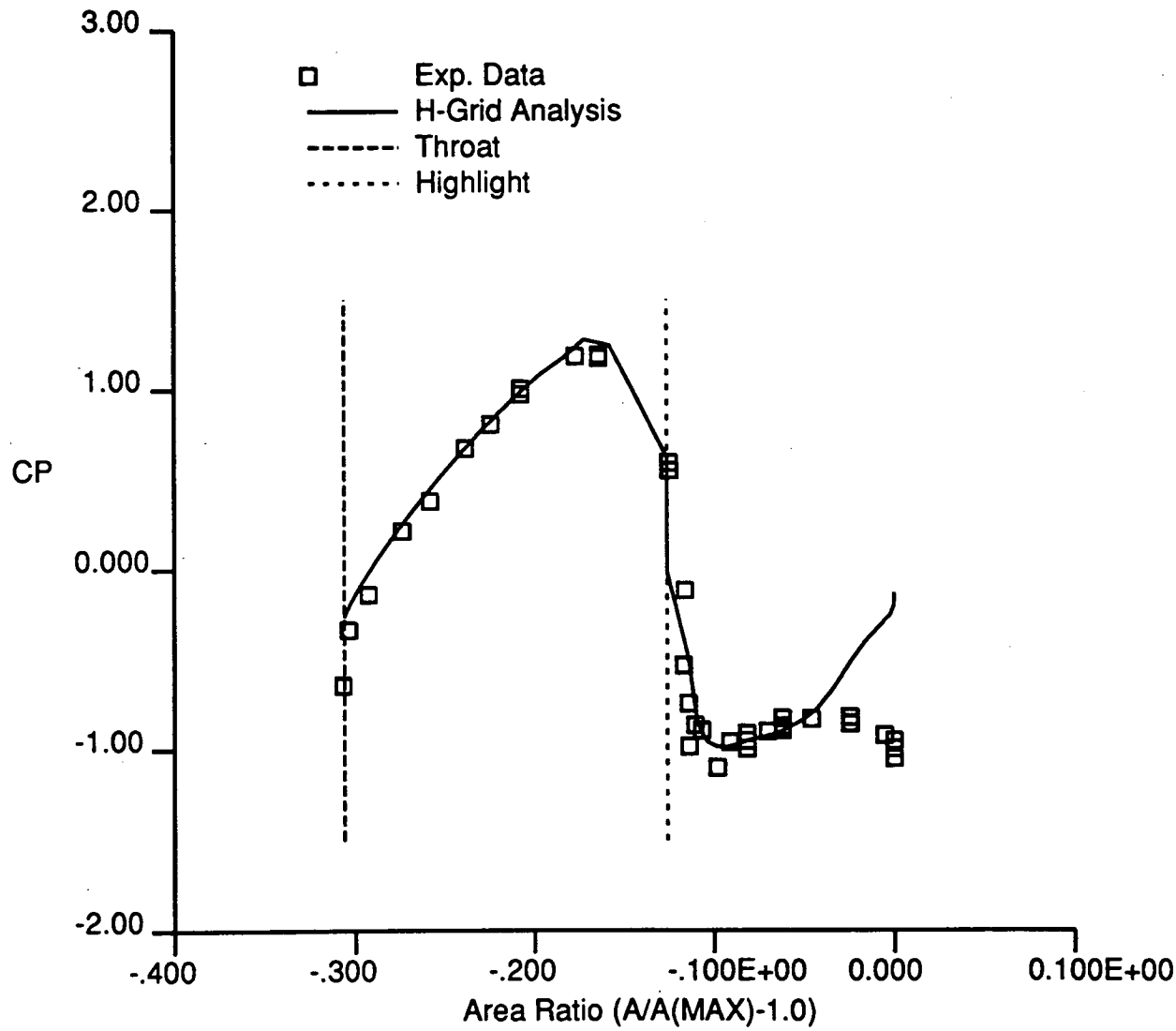

Figure 5.37: Comparison of predicted and experimental cowl leading edge static pressure coefficient distributions for NASA 1.15 pressure ratio fan (H-grid, rotor only, M=0.85)

forces for the adjacent blade in each individual blade row solution. The introduction of the axisymmetric cowl has no bearing on this solution procedure.

Again, the grid pictured in Fig. 5.35 was used although now the thickness of the deswirl vanes is included. A comparison of predicted and experimental data for the cowl leading edge surface static pressure coefficient distributions, nozzle boattail surface static pressure coefficient distributions, and nozzle inlet radial total pressure ratio distributions is given in Fig. 5.38. Again good agreement is obtained for each of these stations, demonstrating the capability of accurately simulating the aerodynamics of a complete ducted fan engine configuration.

An illustration of the predicted fan surface static pressure ratio contours for this calculation is given in Fig. 5.39. The extreme flow gradients at the cowl leading edge and the aerodynamic interaction between the blade tips and cowl inner surface are well displayed in the predicted contours.

The single-rotation fan geometry flowfield was also calculated using the multiple-block C-grid Euler solver. Predictions were based on the multiple-block grid pictured in Fig. 5.40. Grid block sizes were generated to be compatible with the total number of points used in the H-grid calculation, with block sizes of (172x25x15), (68x17x15), (193x9x15), (17x17x15), and (172x21x15), respectively. A comparison of the predicted and experimental cowl leading edge surface static pressure ratios is given in Fig. 5.41 for a Mach number of 0.75 and an advance ratio of 2.86. Again, excellent agreement between experiment and calculation is observed. The embedded C-grid block permits a large number of grid points in the region of the cowl leading edge without incurring an excessive number of points in the remainder of the flowfield. The

NASA 1.15 PRESSURE RATIO FAN PREDICTION M=0.75

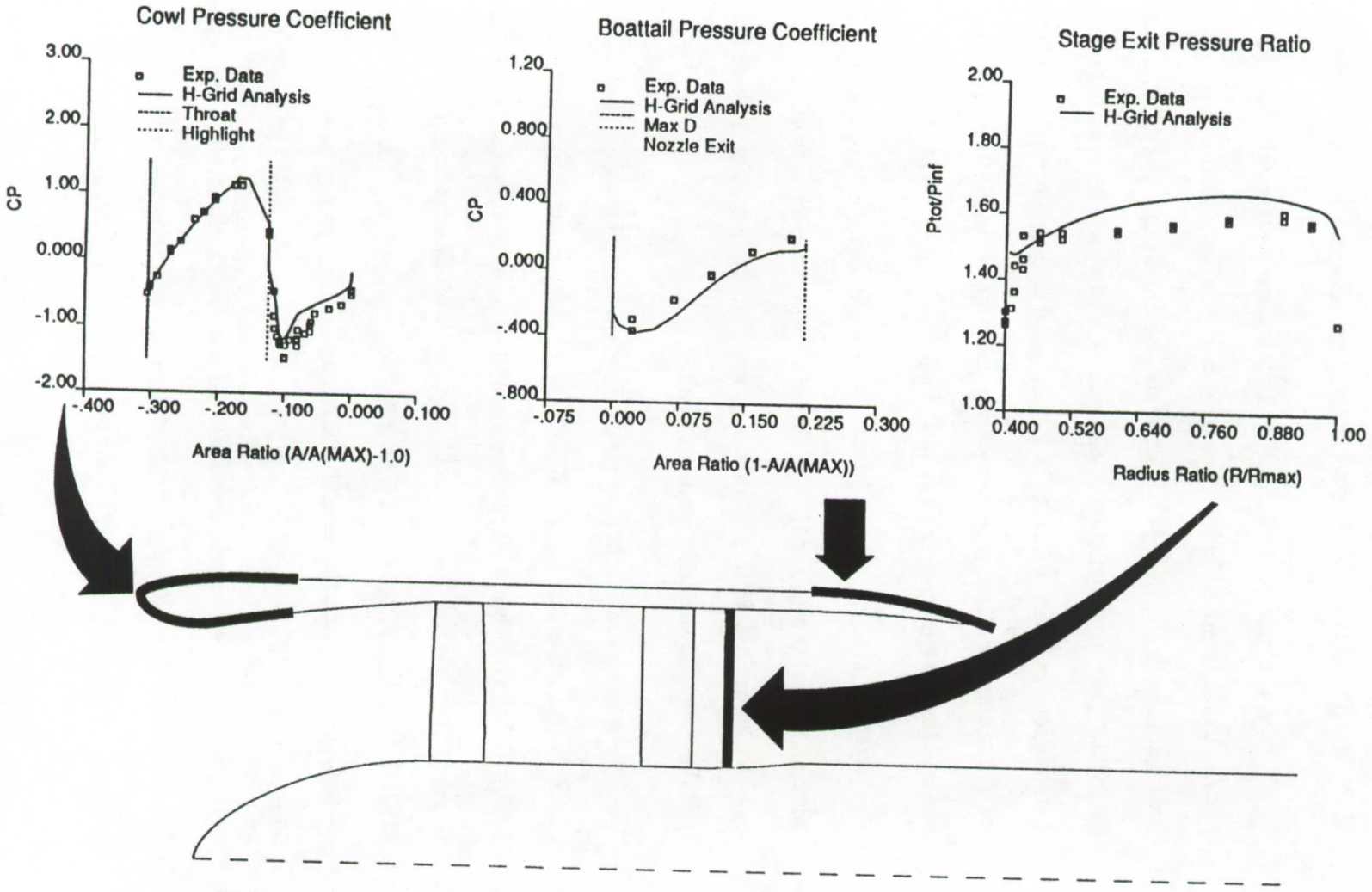

Figure 5.38: Comparison of predicted and experimental pressure data for NASA 1.15 pressure ratio fan stage (H-grid, full stage, M=0.75)

Figure 5.39: Predicted surface static pressure ratio contours for NASA 1.15 pressure ratio fan stage (H-grid, full stage, M=0.75)

high shear associated with the H-grid in this region is also eliminated. The solution was found to have a smooth continuous transition across block boundaries, and a relatively rapid convergence (1500 iterations) was achieved.

A second calculation was performed for the C-grid algorithm at a Mach number of 0.85. A comparison of the predicted and experimental cowl leading edge surface static pressure coefficient distributions is given in Fig. 5.42. Again, excellent agreement is observed over most of the cowl surface, except near the downstream portion of the cowl outer surface. This is again thought to be due to an experimental flow separation, although the deviation is less pronounced in this case. The C-grid results do not differ significantly from the H-grid results for either of the cases examined, although a detailed grid resolution study has not been performed. In addition, the H-grid calculation was performed with a relatively large number of grid points about the cowl leading edge to enhance the accuracy in this critical region. As the number of grid points decreases, the C-grid analysis will likely be superior.

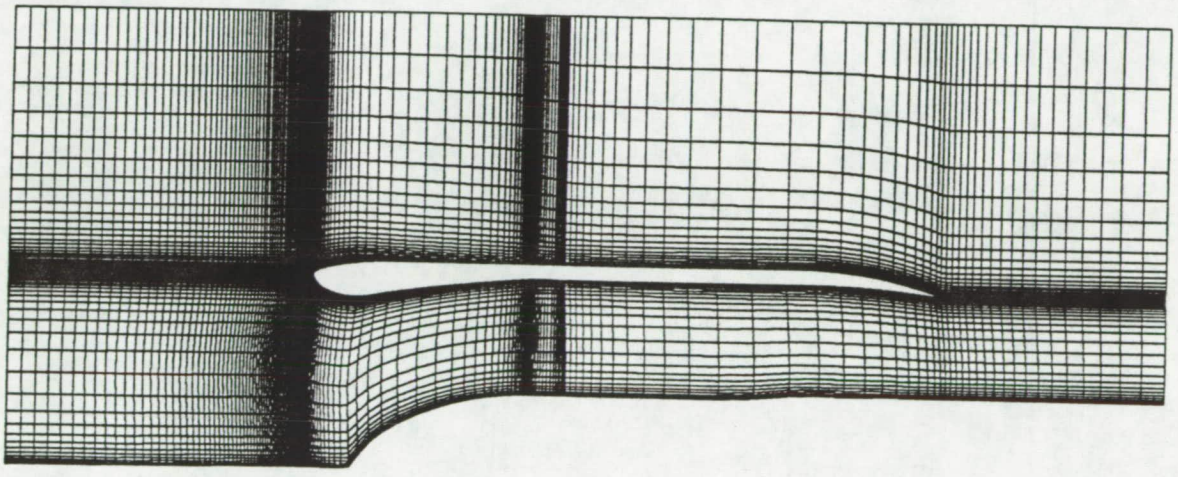

Figure 5.40: Multiple-block C-grid for NASA 1.15 pressure ratio fan stage (rotor only)

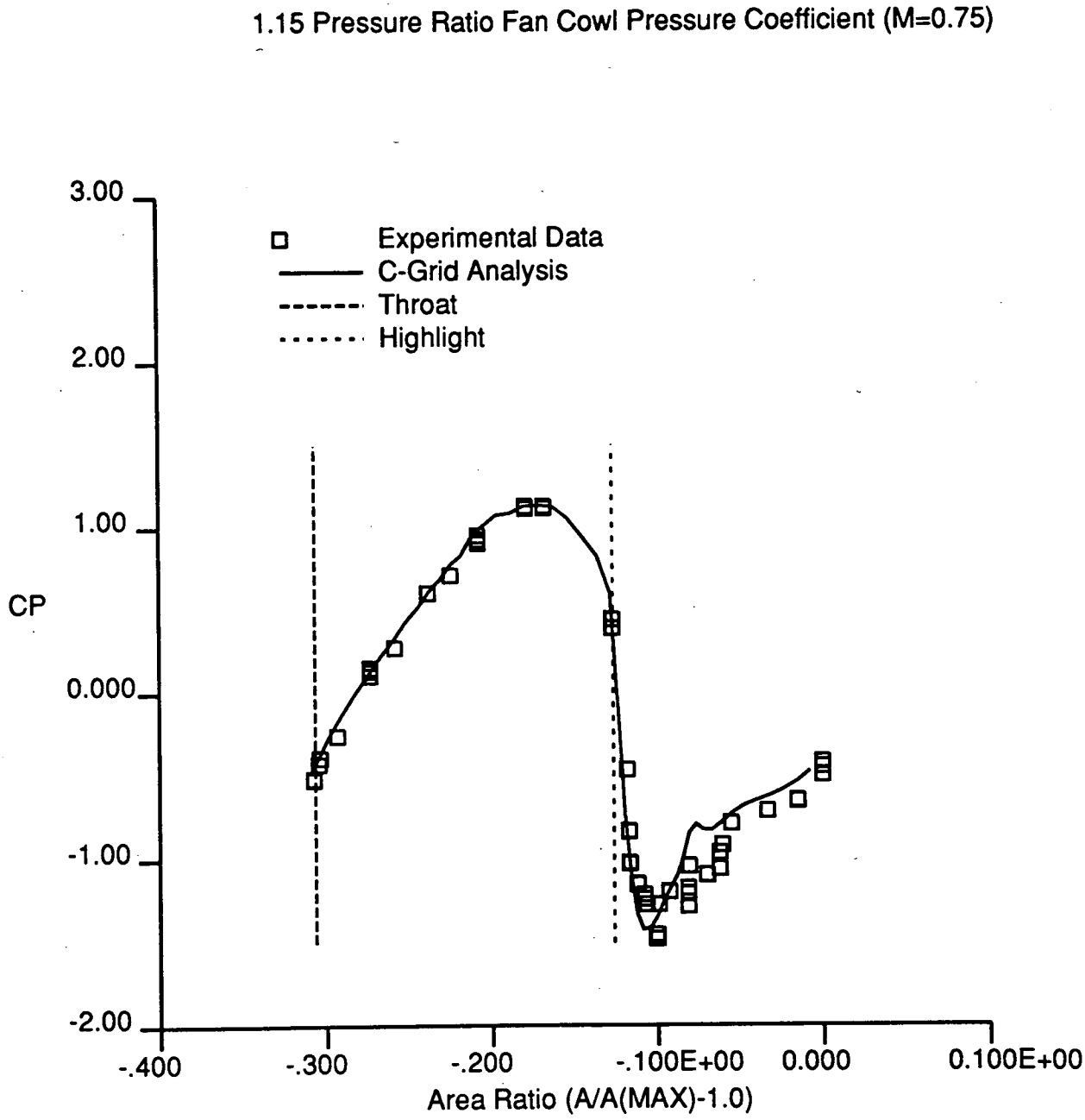

Figure 5.41: Comparison of predicted cowl leading edge static pressure coefficient distributions for NASA 1.15 pressure ratio fan stage (C-grid, rotor only, M=0.75)

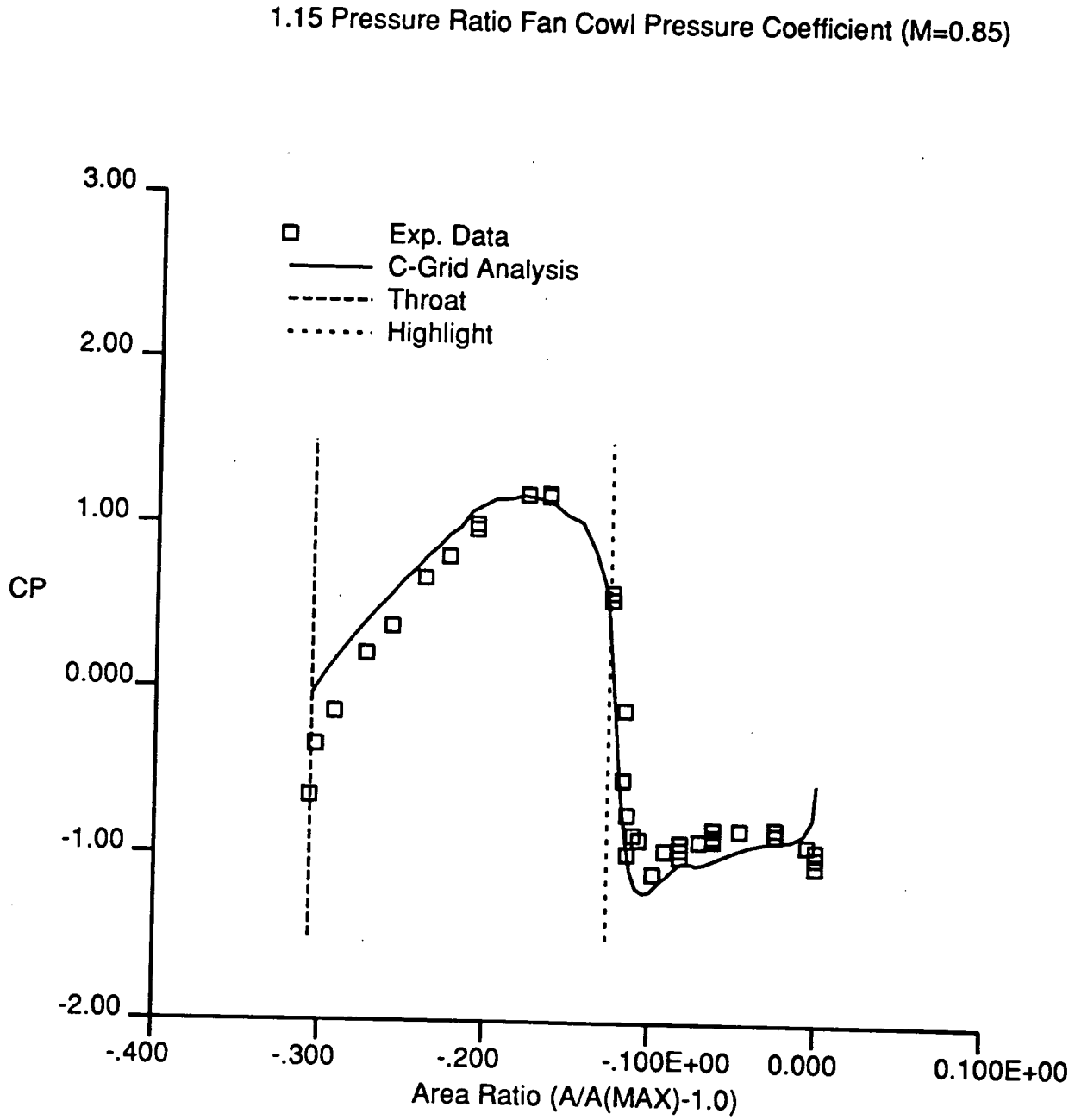

Figure 5.42: Comparison of predicted cowl leading edge static pressure coefficient distributions for NASA 1.15 pressure ratio fan stage (C-grid, rotor only, M=0.85)

6. CONCLUSIONS

A three-dimensional Euler analysis and grid generation scheme have been developed for the numerical analysis of ducted propfan flowfields. Both H-grid and multiple-block C-grid solution structures have been examined. The analysis has been verified through comparisons with experimental results from both a low speed ducted propeller and a high speed 1.15 pressure ratio fan stage for both single-rotation and counter-rotation configurations. At least one case was observed which indicated that a viscous flow analysis might improve the accuracy of the predictions. A comparison of the predicted results for both the H-grid and multiple-block C-grid analysis did not display significant differences, although as the number of grid points decreases, the C-grid analysis will likely be better. The capability of accurately simulating the aerodynamics about a complete ducted fan propulsor system has been demonstrated.

Clearly the largest obstacle in accurately predicting propfan flowfields of any kind is in the specification of the deflected airfoil shape. Calculations for the SR7 clearly displayed how even small errors in the blade setting angle could drastically change the predicted results. A second obstacle encountered in this study was a lack of experimental data for ducted fans which prevented a lengthy verification study for a range of geometries and flow conditions.

REFERENCES

[1] Barton, J. M., Yamamoto, O., and Bober, L. J., "Euler Analysis of Transonic Propeller Flows," *AIAA Journal*, Vol. 3, June 1987, pp. 277-282.

[2] Usab, W. J., Lee, A. K., and Sullivan, J. P., "A Comparison of Numerical Simulation and Experimental Measurements of Flow through Propellers," AIAA Paper 88-0367, 1988.

[3] Celestina, M. L., Mulac, R. A., and Adamczyk, J. J., "A Numerical Simulation of the Inviscid Flow Through a Counterrotating Propeller," ASME Paper 86-GT-136, 1986.

[4] Whitfield, D. L., Swafford, T. W., Janus, J. M., Mulac, R. A., and Belk, D. M., "Three-Dimensional Unsteady Euler Solutions for Propfans and Counter-Rotating Propfans in Transonic Flow," AIAA Paper 87-1197, 1987.

[5] Saito, S., Kobayashi, H., Nakamura, Y., and Matsuo, Y., "Predicted Flow Field Around the Advanced Propeller at Take-Off," AIAA Paper 88-3151, 1988.

[6] Matsuo, Y., Arakawa, C., Saito, S., and Kobayashi, H., "Navier-Stokes Computations for Flowfield of an Advanced Turboprop," AIAA Paper 88-3094, 1988.

[7] Kobayawa, M., and Hatano, I., "Flow Field around a Propeller by Navier-Stokes Equation Analysis," AIAA Paper 88-3150, 1988.

[8] Sacks, A. H., and Burnell, J. A., "Ducted Propellers–A Critical Review," *Progress in Aeronautical Sciences Vol III*, Pergamon Press Inc., New York, 1962, pp. 87-135.

[9] Groeneweg, J. F., and Bober, L. J., "NASA Advanced Propeller Research," NASA TM 101361, 1988.

[10] Walatka, P. P., and Buning, P. G., "PLOT3D User's Manual,", rough draft for NASA TM, 1988.

[11] Mulac, R. A., "A Multistage Mesh Generator for Solving the Average-Passage Equation System," NASA CR 179539, 1988.

[12] Adamczyk, J. J., Celestina, M. L., Beach, T. A., and Barnett, M., "Simulation of Three-Dimensional Viscous Flow Within a Multistage Turbine," ASME Paper 89-GT-152, 1989.

[13] Brackbill, J. B., and Saltzman, J. S., "Adaptive Zoning for Singular Problems in Two Dimensions," *Journal of Computational Physics*, 46, 342-368, 1982.

[14] Thompson, J. F., "Elliptic Grid Generation," *Numerical Grid Generation* (Edited by Joe Thompson), Elsevier Science Publishing Co., 1982.

[15] Adamczyk, J. J., "Model Equation for Simulating Flows in Multistage Turbomachinery," ASME Paper 85-GT-226, 1985.

[16] Adamczyk, J. J., Mulac, R. A., and Celestina, M. L., "A Model for Closing the Inviscid Form of the Average-Passage Equation System," ASME Paper 86-GT-227, 1986.

[17] Hung, C. M., and Kordulla, W., "A Time-Split Finite Volume Algorithm for Three-Dimensional Flow-Field Simulation," AIAA Paper 83-1957, 1983.

[18] Jameson, A., Schmidt, W., and Turkel, E., "Numerical Solutions of the Euler Equations by Finite Volume Methods Using Runge-Kutta Time-Stepping Schemes," AIAA Paper 81-1259, 1981.

[19] Hollanders, H., Lerat, A., and Peyret, R., "Three-Dimensional Calculation of Transonic Viscous Flows by an Implicit Method," *AIAA Journal*, 23, pp. 1670-1678, 1985.

[20] Jameson, A., and Baker, T. J., "Solution of the Euler Equations for Complex Configurations," AIAA Paper 83-1929, 1983.

[21] Jorgensen, P. C. E., and Chima, R. V., "An Unconditionally Stable Runge-Kutta Method for Unsteady Flows," NASA TM 101347, 1989.

[22] Stefko, G. L., Rose, G. E., and Podboy, G. G., "Wind Tunnel Performance Results of an Aeroelstically Scaled 2/9 Model of the PTA Flight Test Propfan," NASA TM 89917, 1987.

[23] Bushnell, P., "Measurement of the Steady Surface Pressure on a Single Rotation Large Scale Advanced Prop-Fan Blade at Mach Numbers from 0.03 to 0.78," NASA CR 182124, 1988.

[24] Hall, E. J., "Simulation of Time-Dependent Compressible Viscous Flows Using Central and Upwind-Biased Finite-Difference Techniques," Ph.D. dissertation, Iowa State University, 1989.

[25] Williams, M. H., Cho, J., and Dalton, W. N., "Unsteady Aerodynamic Analysis of Ducted Fans," (to appear in the *AIAA Journal of Propulsion and Power*).

[26] Kruger, W., "On Wind Tunnel Tests and Computations Concerning the Problem of Shrouded Propellers," NACA TM 1202, 1949.

[27] Steffen, F. W., "Cruise Performance of an Isolated 1.15 Pressure Ratio Turbofan Propulsion Simulator at Mach Numbers from 0.6 to 0.85," NASA TM X-3064, 1974.

[28] Wesoky, H. L., Abbott, J. M., Albers, J. A., and Dietrich, D. A., "Low-Speed Wind Tunnel Tests of a 50.8 Centimeter (20-in.) 1.15 Pressure Ratio Fan Engine Model," NASA TM X-3062, 1974.

[29] Wesoky, F. L., and Steffen, F. W., "Wind Tunnel Tests of a 20 in. Diameter 1.15 Pressure Ratio Fan Engine Model," NASA TM X-71445, 1973.

[30] Osborn, W. M., and Steinke, R. J., "Performance of a 1.15 Pressure-Ratio Axial-Flow Fan Stage with a Blade Tip Solidity of 0.5," NASA TM X-3052, 1974.

APPENDIX A. GRID GENERATOR OPERATING INSTRUCTIONS

A.1 Introduction

Grid generation for both the H-grid and C-grid Euler analyses is performed by a single program with identical input formats. The grid generation source program is written in FORTRAN 77, and has been used successfully on Cray UNICOS and IBM VM/CMS mainframe computer systems, as well as Silicon Graphics 4D workstations using a UNIX operating system. Array dimensions in the programs are specified by a PARAMETER statement in the MAIN routine. The PARAMETER statement appears as:

PARAMETER(IJX=100, KX=15, NX=2)

and appears in every subroutine. Another important parameter, PRECIS, is based on the precision of the host computer and is determined internally.

The individual variables in the PARAMETER statement are defined as:

IJX Used to determine the maximum number of points in the axial direction

KX The maximum number of points in the circumferential direction

NX The maximum number of blade rows

Array storage is determined through a variable IXT which is defined as $IXT = (2NX + 1)IJX$. The parameter IXT then determines the maximum number of

points in the axial direction. Several rules for storage must be observed for proper operation of the code. Storage is assigned under the assumption that $IJX > KX$. The parameter NX must be greater than or equal to the number of blade rows. For multiple-block C-grid generation, KX must be greater than or equal to $JMAX + 1$ ($JMAX$ is an input parameter described below). The first step in any grid generation sequence should be to estimate the size of the grid to be generated and to make sure that adequate array storage is provided for the anticipated grid. Unusual results can occur when an array size is exceeded, and many unexplained errors can be traced to inadequate array dimensions.

The grid generation code can be used for either ducted or unducted, single- or counter-rotation propfans systems in the H-grid mode, and ducted single-rotation propellers in the C-grid mode. An option is provided to arbitrarily adjust the 3/4 radius blade setting angle without modifying the blade geometry parameters. This assumes that the pitch change axis is perpendicular to the axis of rotation, and only a solid body rotation can occur (no deflections). This procedure is somewhat limited by the airfoil cross section coordinate distribution due to the requirement of maintaining the index of the true leading and trailing edge points.

The program produces plotting output suitable for viewing using the PLOT3D graphics software package developed at the NASA Ames Research Center. This software permits workstation grid generation and processing before invoking the flow solver. PLOT3D output is written to FORTRAN unit 4 for H-grid generation, while the C-grid version writes individual block grid information to units 41-45 for the five-block architecture. Additional PLOT3D outputs can be generated for debugging

purposes by small changes in the input. Some PostScript output is also available on FORTRAN unit 15, although this is primarily for analyzing the quality of the cowl C-grid in the multiblock grid generation.

The input/output files used by the grid generation codes are described in the first section below. This section is then followed by a more general section which describes the function of the individual subroutines in the computer program.

Geometric data may be input in either dimensional, or nondimensional form. However, each component must be defined in a consistent (either dimensional or nondimensional) manner. The final grid coordinates will be nondimensionalized by the maximum propeller diameter.

A.2 Input/Output File Description

An example input data file is shown in Fig. A.1. A brief description of the variables used in the data file is given below.

VARIABLE	DESCRIPTION
TITLE	An 80 character title for the mesh generation.
NBLROW	Number of blade rows: for C-grids, this must be 1, for H-grids, this must be less than or equal to PARAMETER NX.
IGEOM	Internal/external geometry parameter: if = 1, internal flow (e.g. compressor, turbine), if = 2, external flow (e.g. propfan, ducted propfan).

```
+TITLE-----------------------------------------------------------------
 GENERIC DUCTED PROPFAN
+NBLROW--++IGEOM---++ITHETA--++IWRITE--++NCOWL---++JMAX----++IORTH---++IDEBUG--
         1         2         2         2         1         5         1
+NINPLS--++NEXPLS--++NBLPTZ--++NBLPTR--++NBLPTT--++CITER---++ISOLVE--++--------
         1         1        15        15         7        50         0
+ZINLET--++ZEXIT---++CFACLE--++CFACTE--++DFACLE--++DFACTE--++--------++--------
  -0.50000   1.09000      0.02      0.02       1.0       1.0
+RATIN---++RATEX---++RATBB---++RATBLZ--++RATBLR--++RATBLT--++RATTOB--++--------
   1.32000   1.32000   1.20000   1.200000   1.1000   1.05000   1.36000
*****************************************************************************
+NHUB----++NTIP----++--------++--------++--------++--------++--------++--------
        53         2
+ZHUB,RHUB+--------++--------++--------++--------++--------++--------++--------
 -80.00000 -20.00000  -0.45000  -0.40000  -0.37000  -0.35000  -0.33600  -0.3300
  -0.32685  -0.32336  -0.31773  -0.31097  -0.30302  -0.29383  -0.28285  -0.2579
  -0.22232  -0.18130  -0.13606  -0.09774  -0.07757  -0.07042  -0.06853  -0.0618
  -0.05049  -0.03837  -0.02810  -0.01930  -0.01181  -0.00522   0.00080   0.0065
   0.01215   0.01808   0.02469   0.03237   0.04148   0.05238   0.06434   0.0731
   0.07788   0.07965   0.09454   0.11764   0.15665   0.21074   0.27769   0.3549
   0.43958   0.58799   0.75179   0.92019   1.09000
   0.00200   0.00200   0.00200   0.00200   0.00260   0.00400   0.00600   0.0080
   0.01000   0.01300   0.02177   0.03076   0.03877   0.04635   0.05436   0.0687
   0.08364   0.09408   0.09971   0.10164   0.10204   0.10239   0.10251   0.1030
   0.10421   0.10611   0.10819   0.11031   0.11257   0.11463   0.11653   0.1183
   0.12065   0.12307   0.12572   0.12874   0.13223   0.13630   0.14061   0.1436
   0.14530   0.14590   0.15081   0.15819   0.16767   0.17458   0.17754   0.1748
   0.16806   0.15661   0.15465   0.15465   0.15465
+ZTIP,RTIP+--------++--------++--------++--------++--------++--------++--------
  -10.0000  10.000
   1.7000    1.700
*****************************************************************************
+NSHR----++NSHRIN--++NSHROU--++NPBCAB--++--------++--------++--------++--------
        75         7         7         3
+ZSHR,RSHR+--------++--------++--------++--------++--------++--------++--------
  0.250000  0.249464  0.247860  0.245194  0.241480  0.236734  0.230970  0.22422
  0.216504  0.207864  0.198340  0.187960  0.176774 -0.164834 -0.176774 -0.1879
 -0.198340 -0.207864 -0.216504 -0.224220 -0.230970 -0.236734 -0.241480 -0.2451
 -0.247860 -0.249464 -0.250000 -0.249464 -0.247860 -0.245194 -0.241480 -0.2367
 -0.230970 -0.224220 -0.216504 -0.207864 -0.198340 -0.187960 -0.176774 -0.1648
 -0.152190 -0.138894 -0.125000 -0.110570 -0.095670 -0.080360 -0.064706 -0.0487
 -0.032630 -0.016350  0.000000  0.016350  0.032630  0.048774  0.064706  0.0803
  0.095670  0.110570  0.125000  0.138894  0.152190  0.164834  0.176774  0.1879
  0.198340  0.207864  0.216504  0.224220  0.230970  0.236734  0.241480  0.2451
  0.247860  0.249464  0.250000
  0.410000  0.410010  0.410040  0.410067  0.410083  0.410075  0.410047  0.4100
  0.409958  0.409910  0.409857  0.409797  0.409725  0.404410  0.404362  0.4043
  0.404480  0.404638  0.404887  0.405247  0.405617  0.406077  0.406807  0.4074
  0.408125  0.408895  0.410000  0.410750  0.411665  0.413025  0.414677  0.4161
  0.417597  0.419175  0.420660  0.422092  0.423482  0.424795  0.426020  0.4271
```

Figure A.1: Sample input data file for grid generation

```
  0.428175  0.429077  0.429845  0.430467  0.430922  0.431187  0.431250  0.431113
  0.430775  0.430250  0.429552  0.428700  0.427725  0.426660  0.425538  0.424382
  0.423212  0.422045  0.420887  0.419752  0.418655  0.417597  0.416587  0.415635
  0.414738  0.413900  0.413117  0.412395  0.411742  0.411178  0.410720  0.410382
  0.410162  0.410040  0.410000
*************************************************************************
+NBLD----++NBLCRC--++NPPRC---++IPCH----++ZPCA----++THPCA---++BETA----++--------+
        6         8        21         1       0.0       0.0      60.2
+ZBLA,RBLA,THBLA,TTBLA-------++--------++--------++--------++--------++--------+
  -0.07042  -0.06259  -0.05477  -0.04699  -0.03924  -0.03153  -0.02386  -0.01628
  -0.00878  -0.00130   0.00619   0.01346   0.02074   0.02804   0.03535   0.04269
   0.05004   0.05742   0.06481   0.07222   0.07965
  -0.07840  -0.07040  -0.06241  -0.05443  -0.04648  -0.03857  -0.03070  -0.02287
  -0.01513  -0.00745   0.00021   0.00786   0.01530   0.02277   0.03026   0.03777
   0.04530   0.05285   0.06041   0.06800   0.07560
  -0.08927  -0.08096  -0.07266  -0.06436  -0.05608  -0.04782  -0.03959  -0.03140
  -0.02326  -0.01519  -0.00719   0.00081   0.00875   0.01654   0.02436   0.03219
   0.04005   0.04792   0.05581   0.06372   0.07164
  -0.10222  -0.09346  -0.08470  -0.07594  -0.06718  -0.05844  -0.04971  -0.04101
  -0.03235  -0.02372  -0.01517  -0.00667   0.00183   0.01025   0.01855   0.02690
   0.03526   0.04363   0.05203   0.06043   0.06886
  -0.11092  -0.10175  -0.09257  -0.08339  -0.07421  -0.06504  -0.05588  -0.04674
  -0.03762  -0.02853  -0.01948  -0.01050  -0.00152   0.00741   0.01626   0.02510
   0.03396   0.04283   0.05172   0.06062   0.06953
  -0.10567  -0.09655  -0.08743  -0.07831  -0.06919  -0.06008  -0.05097  -0.04189
  -0.03281  -0.02376  -0.01475  -0.00577   0.00321   0.01214   0.02102   0.02992
   0.03883   0.04775   0.05668   0.06562   0.07457
  -0.08982  -0.08126  -0.07270  -0.06414  -0.05558  -0.04704  -0.03850  -0.02997
  -0.02145  -0.01295  -0.00447   0.00401   0.01246   0.02089   0.02933   0.03777
   0.04622   0.05468   0.06314   0.07160   0.08007
  -0.06358  -0.05613  -0.04869  -0.04125  -0.03381  -0.02638  -0.01895  -0.01153
  -0.00411   0.00330   0.01070   0.01810   0.02549   0.03289   0.04029   0.04769
   0.05509   0.06249   0.06990   0.07731   0.08472
   0.10239   0.10294   0.10369   0.10469   0.10595   0.10746   0.10915   0.11119
   0.11351   0.11588   0.11825   0.12120   0.12414   0.12704   0.12989   0.13269
   0.13544   0.13813   0.14078   0.14337   0.14590
   0.11840   0.11876   0.11930   0.12005   0.12104   0.12229   0.12378   0.12550
   0.12754   0.12983   0.13216   0.13456   0.13753   0.14041   0.14325   0.14603
   0.14877   0.15145   0.15409   0.15666   0.15919
   0.14224   0.14233   0.14263   0.14312   0.14379   0.14471   0.14589   0.14732
   0.14897   0.15095   0.15319   0.15546   0.15789   0.16079   0.16361   0.16639
   0.16910   0.17176   0.17438   0.17693   0.17943
   0.17874   0.17901   0.17911   0.17927   0.17967   0.18025   0.18105   0.18213
   0.18345   0.18499   0.18689   0.18902   0.19118   0.19357   0.19638   0.19906
   0.20169   0.20427   0.20679   0.20926   0.21167
   0.22445   0.22475   0.22492   0.22504   0.22525   0.22562   0.22620   0.22701
   0.22805   0.22934   0.23084   0.23273   0.23467   0.23678   0.23921   0.24169
   0.24409   0.24644   0.24874   0.25098   0.25317
   0.27612   0.27636   0.27645   0.27653   0.27679   0.27718   0.27773   0.27849
   0.27945   0.28059   0.28199   0.28357   0.28518   0.28704   0.28914   0.29112
```

Figure A.1: Sample input data file for grid generation (continued)

```
 0.29306   0.29497   0.29683   0.29863   0.30040
 0.32968   0.32972   0.32988   0.33011   0.33045   0.33092   0.33153   0.3322
 0.33312   0.33418   0.33533   0.33651   0.33789   0.33939   0.34084   0.3422
 0.34365   0.34500   0.34632   0.34761   0.34886
 0.38143   0.38163   0.38192   0.38227   0.38269   0.38317   0.38374   0.3844
 0.38513   0.38585   0.38668   0.38761   0.38851   0.38940   0.39028   0.3911
 0.39196   0.39278   0.39357   0.39436   0.39512
-0.22623  -0.11448  -0.06580  -0.00593   0.03783   0.07747   0.11208   0.1384
 0.15770   0.17116   0.17992   0.18148   0.18524   0.18762   0.18808   0.1867
 0.18416   0.18144   0.17914   0.17788   0.17801
-0.22180  -0.14123  -0.10573  -0.06270  -0.02902   0.00160   0.03009   0.0550
 0.07632   0.09372   0.10771   0.11843   0.12448   0.12892   0.13273   0.1371
 0.14188   0.14653   0.15096   0.15519   0.15910
-0.21743  -0.16069  -0.13115  -0.09805  -0.07011  -0.04451  -0.02039   0.0015
 0.02138   0.03888   0.05401   0.06720   0.07870   0.08821   0.09698   0.1050
 0.11278   0.12067   0.12867   0.13656   0.14430
-0.22009  -0.17785  -0.15193  -0.12440  -0.09990  -0.07691  -0.05491  -0.0343
-0.01496   0.00299   0.01943   0.03450   0.04855   0.06161   0.07367   0.0853
 0.09651   0.10748   0.11820   0.12866   0.13889
-0.22349  -0.18910  -0.16466  -0.13966  -0.11662  -0.09455  -0.07318  -0.0527
-0.03311  -0.01442   0.00338   0.02025   0.03646   0.05204   0.06701   0.0815
 0.09562   0.10941   0.12280   0.13576   0.14805
-0.19509  -0.16591  -0.14364  -0.12121  -0.09998  -0.07939  -0.05926  -0.0396
-0.02054  -0.00199   0.01598   0.03346   0.05037   0.06683   0.08275   0.0982
 0.11322   0.12781   0.14191   0.15547   0.16812
-0.15033  -0.12553  -0.10575  -0.08594  -0.06705  -0.04864  -0.03057  -0.0128
 0.00442   0.02140   0.03806   0.05435   0.07034   0.08590   0.10119   0.1161
 0.13073   0.14494   0.15867   0.17184   0.18402
-0.09282  -0.07252  -0.05588  -0.03926  -0.02329  -0.00766   0.00771   0.0227
 0.03766   0.05229   0.06671   0.08089   0.09482   0.10855   0.12203   0.1352
 0.14816   0.16076   0.17300   0.18478   0.19570
-0.22623  -0.25766  -0.25881  -0.25715  -0.25046  -0.24091  -0.22859  -0.2118
-0.19041  -0.16474  -0.13510  -0.10277  -0.07418  -0.04316  -0.01028   0.0242
 0.05918   0.09269   0.12376   0.15196   0.17801
-0.22180  -0.23798  -0.22938  -0.22032  -0.20653  -0.19103  -0.17463  -0.1569
-0.13762  -0.11651  -0.09377  -0.06880  -0.04048  -0.01104   0.01729   0.0430
 0.06803   0.09214   0.11529   0.13745   0.15910
-0.21743  -0.22212  -0.20847  -0.19620  -0.18074  -0.16395  -0.14652  -0.1281
-0.10906  -0.08898  -0.06796  -0.04625  -0.02392  -0.00143   0.02083   0.0427
 0.06427   0.08517   0.10544   0.12510   0.14430
-0.22009  -0.21557  -0.19920  -0.18427  -0.16738  -0.14978  -0.13197  -0.1137
-0.09505  -0.07598  -0.05637  -0.03634  -0.01600   0.00444   0.02471   0.0448
 0.06456   0.08392   0.10277   0.12103   0.13890
-0.22349  -0.21227  -0.19376  -0.17620  -0.15761  -0.13876  -0.11988  -0.1008
-0.08176  -0.06255  -0.04321  -0.02382  -0.00435   0.01505   0.03434   0.0535
 0.07264   0.09166   0.11059   0.12936   0.14805
-0.19509  -0.18096  -0.16248  -0.14470  -0.12627  -0.10775  -0.08929  -0.0707
-0.05226  -0.03375  -0.01518   0.00331   0.02187   0.04033   0.05875   0.0771
 0.09554   0.11384   0.13209   0.15024   0.16813
-0.15032  -0.13572  -0.11844  -0.10164  -0.08457  -0.06750  -0.05050  -0.0335
```

Figure A.1: Sample input data file for grid generation (continued)

```
-0.01658   0.00034   0.01715   0.03399   0.05071   0.06742   0.08415   0.10087
 0.11762   0.13434   0.15109   0.16771   0.18402
-0.09282  -0.07935  -0.06428  -0.04962  -0.03484  -0.02008  -0.00543   0.00917
 0.02374   0.03826   0.05271   0.06713   0.08149   0.09586   0.11021   0.12457
 0.13894   0.15326   0.16758   0.18182   0.19570
```

Figure A.1: Sample input data file for grid generation (continued)

ITHETA Theta input format for blade definitions:

if = 1, a mean camber line and tangential thickness are to be input,

if = 2, surface theta coordinates are to be input.

IWRITE Mesh write to disk format (not used in this version).

NCOWL Cowl geometry parameter:

if = 0 no cowl, no cowl geometry is read,

if = 1 generate an H-grid for the ducted geometry (cowl geometry is read),

if = 2 generate a multiple-block C-grid for the ducted geometry (cowl geometry is read).

JMAX Defines the number of grid lines from the blade to the outer boundary of the axisymmetric projection of the C-grid block.

(must be $\leq$ PARAMETER KX).

IORTH C-grid orthogonality control parameter:

if = 0, cowl surface points for a C-grid are based on arc length interpolation,

if = 1, cowl surface points for a C-grid are adjusted for orthogonality.

IDEBUG Debugging parameter:

if = 0 no extra debugging plots,

if = 1 several extra PLOT3D data sets are produced for debugging.

NINPLS Number of additional constant spacing inlet planes added to grid.

NEXPLS Number of additional constant spacing exit planes added to grid.

NBLPTZ Number of points on the airfoil in the axial direction

(this must be an odd number).

NBLPTR Number of points on the airfoil in the radial direction (this must be an odd number).

NBLPTT Number of points between airfoils in the circumferential direction (this must be an odd number $\leq$ PARAMETER KX).

NCITER Number of iterations for the C-grid solver.
if = 0 C-grid is generated using the algebraic solver.

ISOLVE C-grid generation algorithm control parameter:
if = 0 C-grid is generated using the Poisson solver.
if = 1 C-grid is generated using the variational solver.

ZINLET Axial location of the initial inlet boundary plane (before constant spacing inlet planes are added).

ZEXIT Axial location of the initial exit boundary plane (before constant spacing exit planes are added).

CFACLE Factor which determines the axial extent of the C-grid upstream of the cowl leading edge (multiplied by cowl axial chord).

CFACTE Factor which determines the axial extent of the C-grid downstream of the cowl trailing edge (multiplied by cowl axial chord).

DFACLE Factor which determines the radial width of the C-grid upstream of the cowl leading edge (if ≥ 1, then larger than tip gap, if ≤ 1, then smaller than tip

gap).

DFACTE Factor which determines the radial width of the C-grid downstream of the cowl trailing edge (if ≥ 1, then larger than tip gap, if ≤ 1, then smaller than tip gap).

RATIN Maximum axial ratio of cells in the inlet region (must be > 1).

RATEX Maximum axial ratio of cells in the exit region (must be > 1).

RATBB Maximum axial ratio of cells between blade rows (must be > 1).

RATBLZ Maximum axial ratio of cells on blades (must be ≥ 1).

RATBLR Maximum radial ratio of cells on blades (must be ≥ 1).

RATBLT Maximum circumferential ratio of cells blade to blade (must be ≥ 1).

RATTOB Maximum radial ratio of cells from tip (unducted H-grids) or the cowl upper surface (ducted H-grids) or the C-grid upper boundary (ducted C-grids) to the outer boundary (must be > 1).

NHUB Number of X,R hub coordinate input pairs to be read.

NTIP Number of X,R outer boundary coordinate pairs to be read.

XHUB,RHUB Hub coordinates.
All of the hub axial coordinates are given first (8 per line), followed separately by the radial coordinates. The number of points input is determined by NHUB.

XTIP,RTIP Outer boundary coordinates.
All of the outer axial coordinates are given first (8 per line, followed separately by the radial coordinates. The number of points input is determined by NTIP.

The following 5 variables are used only for a ducted geometry. They should be deleted for an unducted case.

NSHR Number of X,R cowl coordinate input pairs to be read.

NSHRIN Number of axial grid lines between first blade row leading edge and cowl leading edge. (this must be an odd number).

NSHROU Number of axial grid lines between last blade row trailing edge and cowl trailing edge. (this must be an odd number).

NPBCAB Number of radial grid lines between lower cowl surface and blade tip.

XSHR,RSHR Cowl coordinates. The coordinates are input in a wraparound fashion beginning at the trailing edge and proceeding in the clockwise direction. The trailing edge point must be duplicated as the last coordinate.

All of the cowl axial coordinates are given first (8 per
line), followed separately by the radial coordinates.
The number of points input is determined by NSHR.

The remaining variables define the propfan blades themselves. The blades are defined by radial slices with identical axial and radial coordinates on each side of the airfoil. The slices are given from the hub to the tip. The tip cross section must be specified in a manner which provides some clearance between the tip of the blade and the cowl lower surface, even if the two parts are actually mated. The 8 variables which follow are duplicated for each blade row when more than one row is considered.

NBLA Number of blades in this blade row.

NBLCRC Number of radial cross section used to define the blade.

NPPRC Number of axial points per radial cross section used to
define the blade.

IPCH Pitch change trigger:
if = 0 no pitch change is performed,
if = 1 the pitch change variables ZPCA, THPCA, and BETA
are read in and the blade setting angle is adjusted
to the value specified by BETA.

ZPCA Axial location of the blade pitch change axis.
The pitch change axis is assumed perpendicular to
the axis of rotation.

THPCA Circumferential position of the blade pitch change axis.
The pitch change axis is assumed perpendicular to

the axis of rotation.

BETA Absolute 3/4 radius blade setting angle. (Measured positive from the plane of rotation. The blade setting angle reference plane is the same for either positive or negative rotation [see Fig. A.2]).

ZBLA,RBLA,

THBLA,TTBLA Blade coordinates.

Each of the blade axial coordinates is given first (8 per line) for each cross section, cross sections are given from hub to tip) followed by all the radial coordinates. The blade circumferential coordinates are given next, and may be in two different formats depending on the variable ITHETA. The preferred format is ITHETA=2, where the actual tangential surface coordinates are given for the surfaces ordered in the counter-clockwise direction (for a positive rotation, this would be the suction surface first, then the pressure surface).

The grid generation system produces two primary types of output files: the standard output and the grid or grids (depending on whether a C-grid or H-grid is being produced) themselves. A description of these files is given in Table A.1.

A typical H-grid generated from the sample data set given in Fig. A.1 is shown in Fig. A.3. The blade tip gap has been expanded to illustrate the grid in this region.

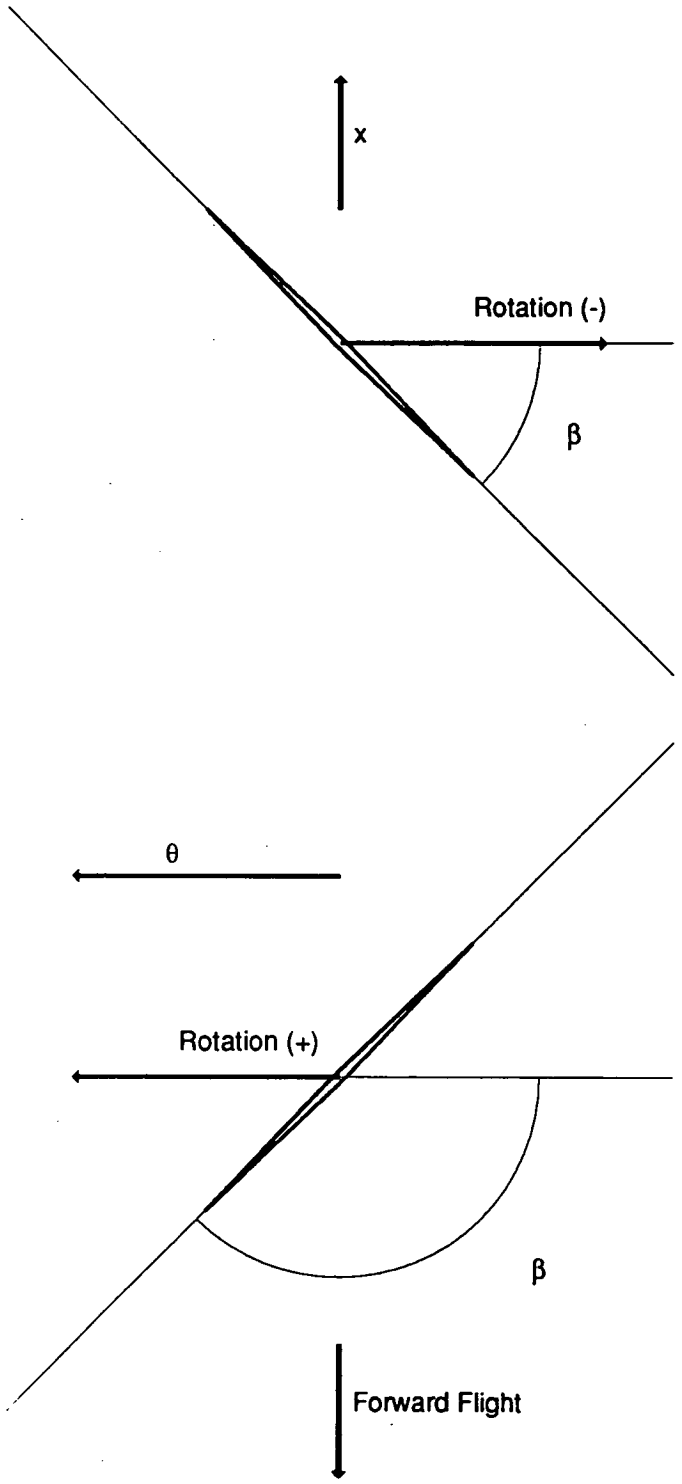

Figure A.2: Blade setting angle reference plane description

Table A.1: Description of input/output files and UNIX-based filenames for H-grid generation

Name	Lu No.	Description
fort.4	4	Unformatted grid data set for first blade row. This may be viewed using PLOT3D, or used directly as input for the aerodynamic analysis.
fort.14	14	Unformatted grid data set for second blade row.
fort.24	24	Unformatted grid data set for third blade row (etc.).
fort.98	98	Geometry and input for grid generator.
fort.99	99	Standard output from grid generator.

The C-grid generation scheme utilizes the same input and standard output files, but produces a number of additional files which are described in Table A.2.

A typical C-grid generated from the sample input data file given in Fig. A.1 modified by the condition $NCOWL = 2$ is shown in Fig. A.4.

A.3 Subroutine Description

A list of the grid generation program subroutines and their functions is given below for reference. A skeleton program flowchart is illustrated in Fig. A.5.

SUBROUTINE	DESCRIPTION
CHGRID	Main calling routine.
ALPHM	Plotting routine - specifically for alphanumeric labels, etc.
CCOWL	Routine for setting up and constructing C-grid boundaries.
CGRID	Routine for determining C-grid interior point distribution.

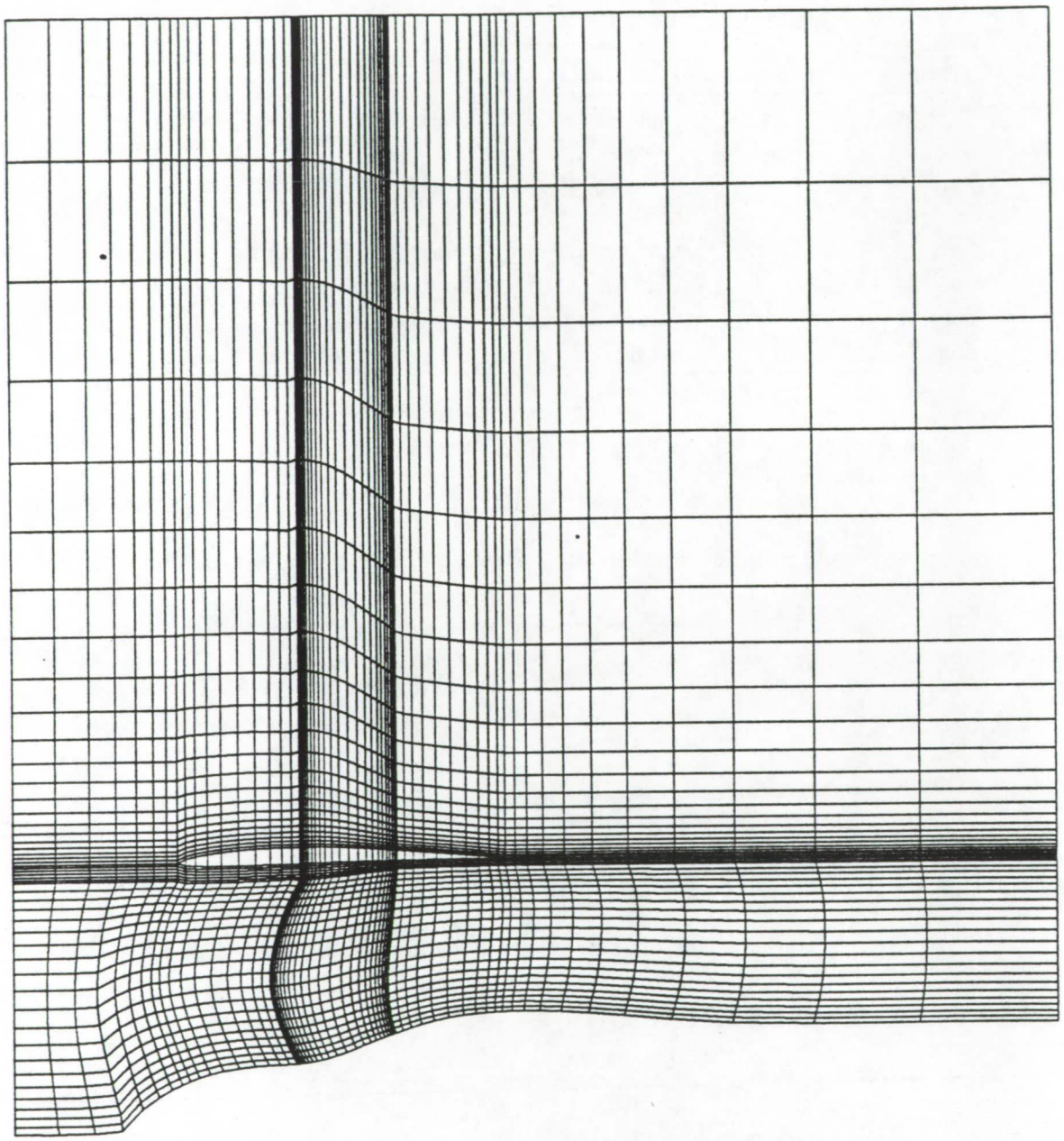

Figure A.3: Sample grid based on H-grid generation

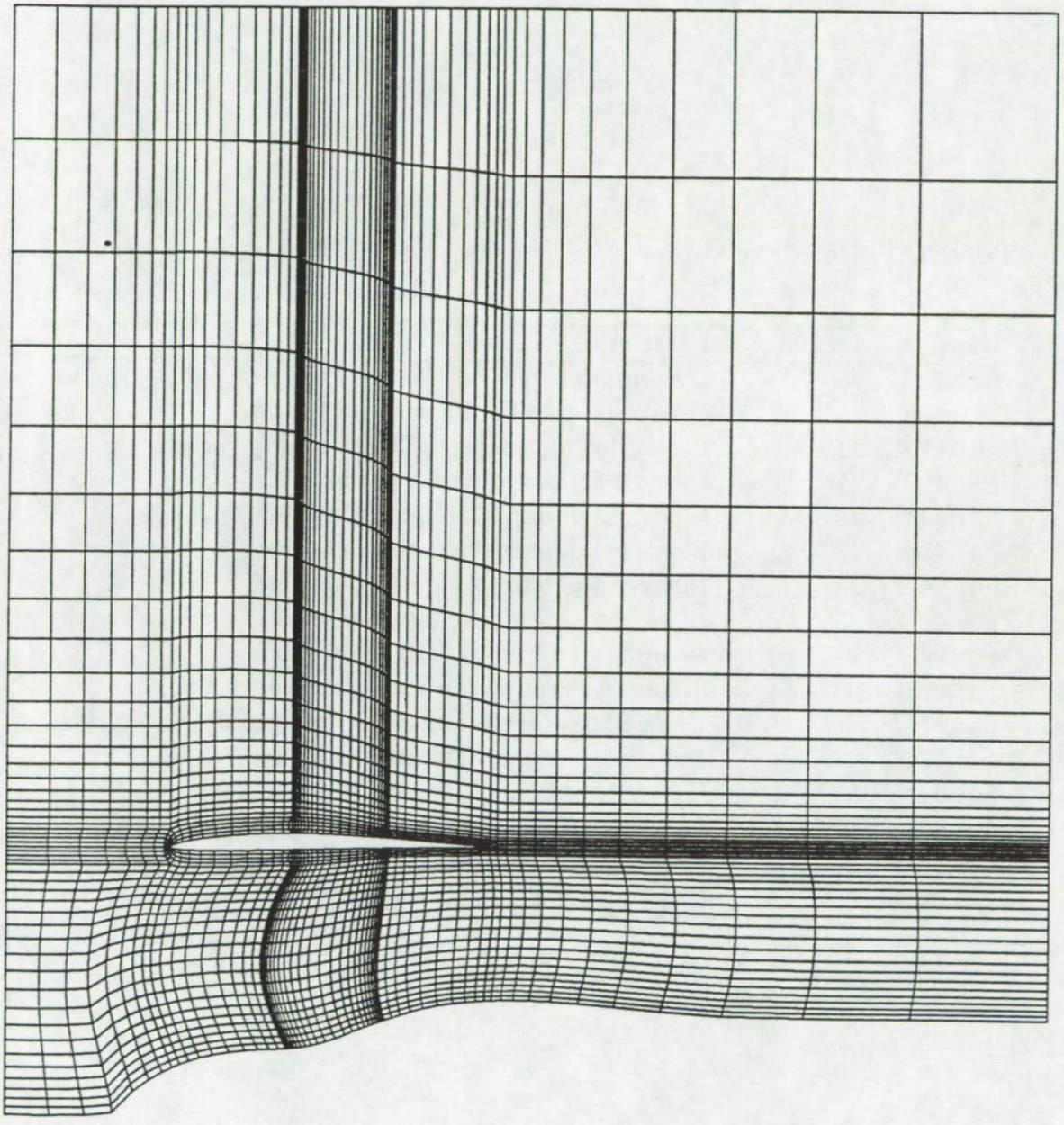

Figure A.4: Sample grid based on multiple-block C-grid generation

Table A.2: Description of input/output files and UNIX-based filenames for C-grid generation

Name	Lu No.	Description
fort.4	4	Unformatted grid data set of axisymmetric projection of coupled grid blocks without C-grid.
fort.15	41	PostScript plot data of C-grid quality.
fort.41	41	Block #1 unformatted grid data set.
fort.42	42	Block #2 unformatted grid data set.
fort.43	43	Block #3 unformatted grid data set.
fort.44	44	Block #4 unformatted grid data set.
fort.45	45	Block #5 unformatted grid data set.
fort.98	98	Geometry and input for grid generator.
fort.99	99	Standard output from grid generator.
fort.17	17	Unformatted grid data set for debugging.
fort.27	27	Unformatted grid data set for debugging.
fort.37	37	Unformatted grid data set for debugging.
fort.47	47	Unformatted grid data set for debugging.
fort.57	57	Unformatted grid data set for debugging.
fort.67	67	Unformatted grid data set for debugging.

COWEX	Routine which determines the outer boundary of the exit region.
COWIN	Routine which determines the outer boundary of the inlet region.
CURPLT	Plotting routine - specifically for plotting data as curves.
END	Plotting routine - specifically for ending a plot.
ERROR	Routine for internal evaluation of potential input data or grid errors.
EULER	Variational-based interior point solver for C-grids.
GENBB	Routine for generating grid point distribution between blades.
GENBL	Routine for determining blade grid point distribution.
GENIN	Routine for determining inlet region grid point distribution.
GUESS	Routine for generating an initial guess for C-grid interior point grid generation scheme.
INRSCT	Spline-based routine for determining the intersection of two curves.
INTERP	Polynomial-based interpolation routine.
METRIC	Routine for determining metric terms in C-grid generation.
NUMBER	Plotting routine - specifically for plotting numbers.
NUMPTS	Routine for determining the number of grid lines required for a specified grid cell ratio in a given region.
POISON	Poisson-based interior point solver for C-grid.
POLFIT	Polynomial-based interpolation routine.
PRINT0	Output routine for grid generation.
SCALE	Plotting routine - specifically for generating scales.

SPLINT	Cubic spline polynomial interpolation routine.
START	Plotting routine - specifically for initiating a plot.
WEIGHT	Grid point weighting routine for variational grid generation.
ZCOWL	Routine for generating H-grids about cowls.

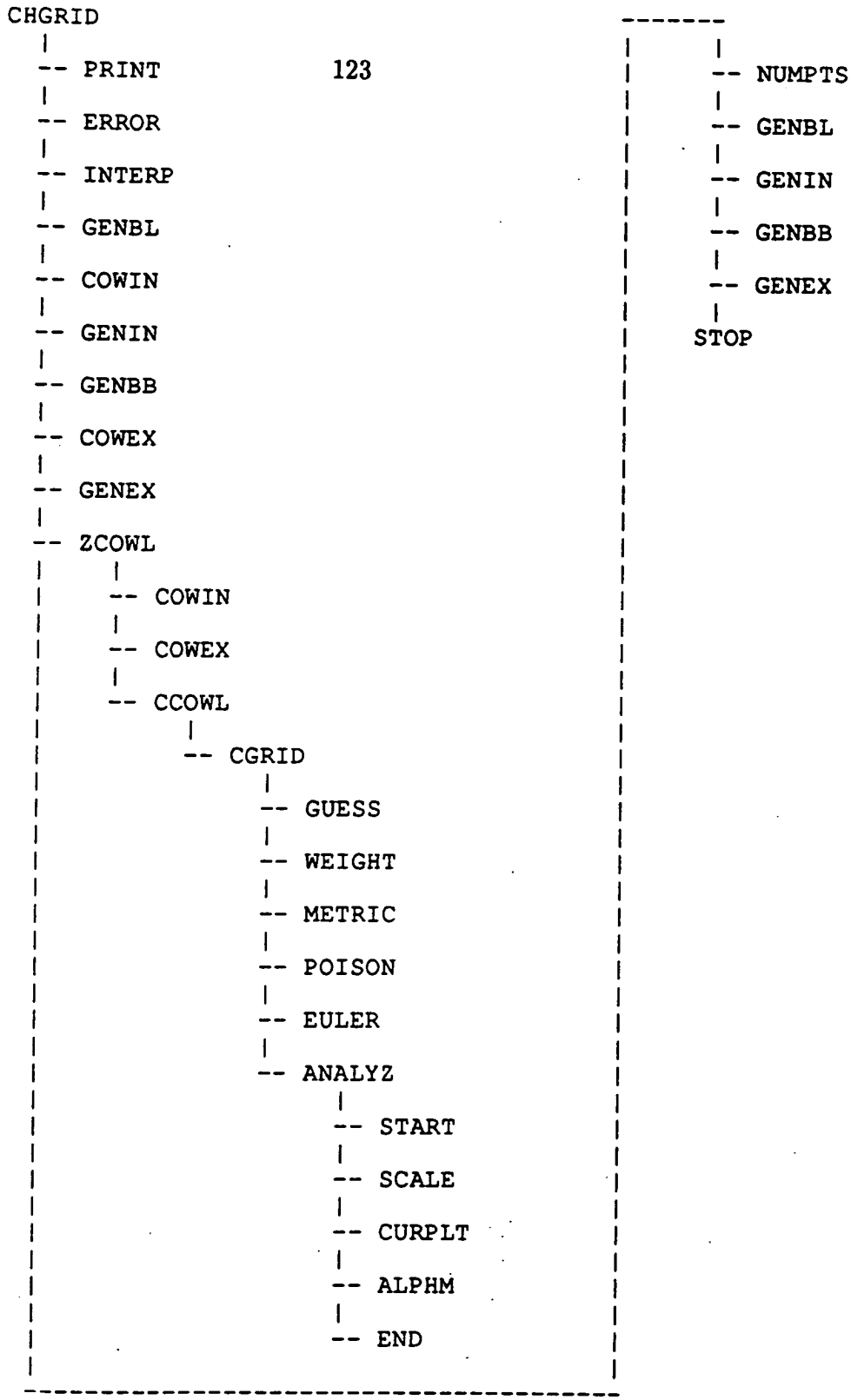

Figure A.5: Program flowchart for ducted propfan analysis grid generation

APPENDIX B. 3D EULER SOLVER OPERATING INSTRUCTIONS

B.1 Introduction

This appendix contains the computer program User's Manual for the 3D Euler ducted propfan aerodynamic analysis. Again, as in the grid generation, both an H-grid and a multiple-block C-grid solution scheme have been developed for the analysis of ducted propfans. In this case, separate programs are used for each of these analyses, although a number of similarities exist for the operation of each code. The H-grid flow solver can also be used as is for the analysis of unducted propfans. The H-grid version also has the capability of analyzing counter-rotating ducted propfans using the average-passage system of equations.

The flow solver source programs are written in FORTRAN 77, and have been used successfully on Cray UNICOS and IBM VM/CMS mainframe computer systems as well as Silicon Graphics 4D workstations using a UNIX operating system. Array dimensions in the programs are specified by a PARAMETER statement in each code. The H-grid analysis parameters are specified in the statement:

```
PARAMETER( IMX=125, JMX=25, KMX=16 )
```

which appears in every subroutine.

The H-grid Euler analysis PARAMETER variables are defined as:

IMX Number of axial grid lines + 1

JMX Number of radial grid lines + 1

KMX Number of circumferential grid lines + 1

The C-grid Euler analysis code uses several PARAMETER statements all in the main routine given as:

```
PARAMETER( NBLKS = 5 )
PARAMETER( IMX1=125, JMX1=25, KMX1=16 )
PARAMETER( IMX2=125, JMX2=25, KMX2=16 )
PARAMETER( IMX3=125, JMX3=25, KMX3=16 )
PARAMETER( IMX4=125, JMX4=25, KMX4=16 )
PARAMETER( IMX5=125, JMX5=25, KMX5=16 )
```

The C-grid Euler analysis PARAMETER variables are defined as:

NBLKS Number of grid blocks (this need not be changed)

IMX1 Number of axial grid lines in block # 1 + 1

IMX2 Number of axial grid lines in block # 2 + 1

IMX3 Number of axial grid lines in block # 3 + 1

IMX4 Number of axial grid lines in block # 4 + 1

IMX5 Number of axial grid lines in block # 5 + 1

JMX1 Number of radial grid lines in block # 1 + 1

JMX2 Number of radial grid lines in block # 2 + 1

JMX3 Number of radial grid lines in block # 3 + 1

JMX4 Number of radial grid lines in block # 4 + 1

JMX5 Number of radial grid lines in block # 5 + 1

KMX1 Number of circumferential grid lines in block # 1 + 1

KMX2 Number of circumferential grid lines in block # 2 + 1

KMX3 Number of circumferential grid lines in block # 3 + 1

KMX4 Number of circumferential grid lines in block # 4 + 1

KMX5 Number of circumferential grid lines in block # 5 + 1

The requirement that the PARAMETER variables be 1 element larger than the grid dimensions results from the use of phantom points outside the computational domain to impose the numerical boundary conditions.

An important requirement here is that the first array dimension must be larger than the second and third array dimensions. This is based on the dimensioning scheme used for certain temporary variables in the code. This condition therefore imposes some limitations on the grid sizes that may be run without modifying the code. Under certain conditions, it may also be required that the second grid dimension be larger than the third.

Approximate computational storage and CPU requirements can be estimated for either the H-grid or C-grid Euler codes from the following formulas:

$$\text{CPU sec} \approx 4.0x10^{-5}(\#\text{ grid points})(\#\text{ iterations})$$

$$\text{Memory Mw} \approx 2.7x10^{-5}(\#\text{ grid points})$$

These formulas are valid for a Cray-II computer operating under the UNICOS environment and the cf77 compiler.

The programs produce plotting output suitable for viewing using the PLOT3D graphics software package developed at the NASA Ames Research Center. PLOT3D output is written to FORTRAN unit 9 for the H-grid solver, while the C-grid version

writes individual block grid information to units 91-95 for the five-block architecture.

B.2 Input/Output Files

An example input data file for the H-grid and multiple-block C-grid 3D Euler solvers is shown in Fig. B.1. A brief description of the form of the data file follows. It should be noted that the H-grid Euler solver was developed from an existing 3D Euler code with a number of acceleration features including axisymmetric averaging, reduced solution domain, grid coarsening and grid refinement. Many of the input variables listed below deal with controlling these functions. Due to the nature of the analysis for ducted propfans, however, several of these algorithms are not enabled. Therefore, a description of the controlling variables is provided for reference only, and should not be considered functional in the present analysis.

VARIABLE	DESCRIPTION
MACH	Freestream Mach number.
GAMMA	Specific heat ratio (c_p/c_v).
PEXIT	Freestream static pressure. This is applied at the outer exit boundary and integrated radially inward for propellers (DUCT=0.0), or applied at the hub and integrated radially outward for compressors (DUCT=1.0) to satisfy radial equilibrium.
OMEGA	Nondimensional rotational speed (this value will be adjusted to match the advance ratio when ADVR $\neq$ 0.0).

```
+--MACH--++-GAMMA--++-PEXIT--++-OMEGA--++--ADVR--++--DUCT--++-COWL---+
    0.8000    1.4000   0.65602    0.0000   -3.0600       0.0       1.0
+--CFL---++--VIS2--++--VIS4--++--QFIL--++---BC---++-BLDROW-++-DTAXI--+
      -5.5      2.00     1.000    0.0000    0.0000       1.0      0.80
+-FNCMAX-++--REST--++--SAVE--++-FISTEP-++-FNPRNT-++-ROWMAX-++-FPRAXI-+
     720.0       1.0       1.0       1.0       1.0       1.0       0.0
+-REFINI-++-REFINJ-++-REFINK-++--EPSX--++--EPSY--++--EPSZ--++-FPRBF--+
       1.0       1.0       1.0      2.00      2.00      2.00       0.0
+-RFINII-++-RFINJJ-++-RFINKK-++--FAXI--++-FAXIMX-++-FR3DMX-++--FTURB-+
       1.0       1.0       1.0       0.0   99999.0       0.0    0020.0
+-FAXIS--++-FAXIE--++-FSTART-++-FEXIT--++-JBASE--++-OMEGS1-++-OMEGS2-+
     -10.0      -9.0      5.00      4.00       1.0    0.0000    0.0000
```

Figure B.1: Sample input data file for ducted propfan 3D Euler solver

ADVR Advance ratio ($J = U/nD$):

if = 0.0, rotational speed is determined by OMEGA.

DUCT Internal flow duct option:

if = 0.0, external flow options are utilized (propeller),

if = 1.0, an internal flow is assumed (compressor). No slip boundary conditions are applied at the outer boundary rather than the characteristic far field condition.

COWL Cowl geometry trigger:

if = 0.0, an unducted geometry is assumed,

if = 1.0, duct boundary conditions are applied (only meaningful for H-grid flow solver).

CFL Time step parameter:

if ≤ 0 then this is the CFL number used to determine the calculation time step for local time stepping,

if > 0.0 then this is the CFL number used to determine the calculation time step without local time stepping.

VIS2 Second order damping coefficient (≈ 2.0) (divided by 4 in the code)

VIS4 Fourth order damping coefficient (≈ 1.0) (divided by 64 in the code)

QFIL Not active in this version (0.0).

BC Exit boundary condition trigger:

if = 0.0, characteristic boundary condition based on P_{tot} is used,

if = 1.0, characteristic boundary condition based on mass flow is used.

BLDROW Blade row parameter. This value determines which blade row is being calculated during a multiple blade row solution. For single blade row calculations, this should be = 1.0.

DTAXI Not active in this version.

FNCMAX Maximum number of time steps to be performed.

REST Restart option parameter:

if = −1.0 a restart file and body force file are read,

if = 0.0 no restart file, initialize variables in code,

if = 1.0 a restart file is read.

SAVE Save restart file option parameter:

if = −1.0 restart files and body source terms are output at the end of a run,

if = 0.0 no restart file is output at the end of the run,

if = 1.0 a restart file is output at the end of the run.

FISTEP Not active in this version (= 1.0).

FNPRNT Not active in this version (= 0.0).

ROWMAX Maximum number of blade rows in the current solution. For single rotation, = 1.0. For multiple blade rows, this parameter indicates that additional grids and

body source terms are to be read.

FPRAXI Print axisymmetric solution,

if = 0.0 axisymmetric solution is not printed,

if = 1.0 axisymmetric solution is printed.

REFINI Grid-coarsening trigger, not active in this version (1.0).

REFINJ Grid-coarsening trigger, not active in this version (1.0).

REFINK Grid-coarsening trigger, not active in this version (1.0).

EPSX Implicit residual smoothing coefficient in the axial direction ($\approx$ 2.0 is a typical value).

EPSY Implicit residual smoothing coefficient in the radial direction ($\approx$ 2.0 is a typical value).

EPSZ Implicit residual smoothing coefficient in the circumferential direction ($\approx$ 2.0 is a typical value).

FPRBF Print trigger for body forces:

if = 0.0, body forces are not printed,

if = 1.0, body forces are printed.

RFINII Fine mesh conversion, not active in this version (1.0).

RFINJJ Fine mesh conversion, not active in this version (1.0).

RFINKK Fine mesh conversion, not active in this version (1.0).

FAXI Number of axisymmetric solutions, not active in this version (0.0).

FAXIMX Number of 3D passes before axisymmetric solutions, not active in this version (99999.0).

FR3DMX Number of reduced domain 3D passes, not active in this version (0.0).

FTURB	Not active in this version (0.0).
FAXIS	Not active in this version (0.0).
FAXIE	Not active in this version (0.0).
FSTART	Not active in this version (0.0).
FEXIT	Not active in this version (0.0).
JBASE	Not active in this version (0.0).
OMEGS1	Not active in this version (0.0).
OMEGS2	Not active in this version (0.0).

The Euler solver system produces three primary types of output files: the standard output, plot output, and restart files. A list and description of each of these files is given in Table B.1 for the H-grid Euler analysis and Table B.2 for the C-grid Euler analysis.

B.3 H-grid Euler Solver Subroutine Description

A list of the 3D H-grid Euler solver program subroutines and their functions is given below for reference. A skeleton program flowchart is illustrated in Fig. B.2.

SUBROUTINE	DESCRIPTION
HPRO3D	Main calling routine.
BAXI	Calculates axisymmetric flow quantities.
BAXI2D	Calculates axisymmetric flow quantities for 2D solution.
BAXIA	Axisymmetric flow averaging routine.
BCCL	Boundary condition routine for cowl lower surface.

Table B.1: Description of input/output files and UNIX-based filenames for H-grid Euler solver

Name	Lu No.	Description
fort.1	1	New restart file output for first blade row.
fort.2	2	Old restart file input for first blade row.
fort.3	3	Old body force output for first blade row.
fort.4	4	Unformatted grid data set for first blade row. This may be viewed using PLOT3D, or used directly as input for the aerodynamic analysis.
fort.5	5	Main program input data file (may be redirected).
fort.6	6	Main program output data file (may be redirected).
fort.9	9	Unformatted flow data set. This may be viewed using PLOT3D.
fort.11	11	New body force output for current blade row.
fort.12	12	Old restart file for second blade row.
fort.22	22	Old restart file for third blade row (etc.).
fort.13	13	Old body force output for second blade row.
fort.23	23	Old body force output for third blade row (etc.).
fort.14	14	Unformatted grid data set for second blade row.
fort.24	24	Unformatted grid data set for third blade row (etc.).

Table B.2: Description of input/output files and UNIX-based filenames for multiple-block C-grid Euler solver

Name	Lu No.	Description
fort.11	11	New restart file output for block #1.
fort.12	12	New restart file output for block #2.
fort.13	13	New restart file output for block #3.
fort.14	14	New restart file output for block #4.
fort.15	15	New restart file output for block #5.
fort.21	21	Old restart file input for block #1.
fort.22	22	Old restart file input for block #2.
fort.23	23	Old restart file input for block #3.
fort.24	24	Old restart file input for block #4.
fort.25	25	Old restart file input for block #5.
fort.41	41	Block #1 unformatted grid data set.
fort.42	42	Block #2 unformatted grid data set.
fort.43	43	Block #3 unformatted grid data set.
fort.44	44	Block #4 unformatted grid data set.
fort.45	45	Block #5 unformatted grid data set.
fort.51	51	Main program input data file for block #1.
fort.52	52	Main program input data file for block #2.
fort.53	53	Main program input data file for block #3.
fort.54	54	Main program input data file for block #4.
fort.55	55	Main program input data file for block #5.
fort.6	6	Main program output data file (may be redirected).
fort.61	61	Block #1 printed output file.
fort.62	62	Block #2 printed output file.
fort.63	63	Block #3 printed output file.
fort.64	64	Block #4 printed output file.
fort.65	65	Block #5 printed output file.
fort.91	91	Unformatted flow plot data set for block #1.
fort.92	92	Unformatted flow plot data set for block #2.
fort.93	93	Unformatted flow plot data set for block #3.
fort.94	94	Unformatted flow plot data set for block #4.
fort.95	95	Unformatted flow plot data set for block #5.
		All unformatted grid and flow plot data sets may be viewed using PLOT3.

BCCU	Boundary condition routine for cowl upper surface.
BCEXT	Boundary condition routine for exit cells.
BCINL	Boundary condition routine for inlet cells.
BCJ	Boundary condition routine for j=constant surfaces (hub and outer boundaries).
BCJ2	Boundary condition routine for j=constant surfaces (hub and outer boundaries for 2D solution).
BCK	Boundary condition routine for the blade surfaces.
BCWAL2	Axisymmetric boundary conditions at the exit for the 2D solution.
BCWALL	Boundary condition routine for periodic cells.
BFORCE	Routine for calculating body force terms using the axisymmetric equations.
BFREAD	Routine to read in body force terms for all adjacent blade rows.
ERROR	Convergence-checking routine for Runge-Kutta solver (not used for propfans).
ERROR2	Convergence-checking routine for 2D Runge-Kutta solver.
ERROR3	Convergence-checking routine for reduced domain 3D solution.
ERRORP	Convergence-checking routine for Runge-Kutta solver for propfan calculations.
EULER	Runge-Kutta solver.

EULER2	2D Runge-Kutta solver.
EULER3	Reduced domain Runge-Kutta solver.
FILTE2	2D artificial dissipation routine.
FILTE3	Reduced domain artificial dissipation routine.
FILTER	Artificial dissipation routine.
FIXUP	Routine to correct boundary cells before output averaging is performed.
GRIDG	Routine to read and set up the grid.
INITA	Routine to initialize flowfield with axisymmetric solution.
INITB	Routine to replace flowfield with latest axisymmetric solution.
INPUT	Routine to read in input data and set up reference values.
METRI2	Routine to calculate cell volumes and surface normals for 2D solution.
METRIC	Routine to calculate cell volumes and surface normals.
OP2D	Routine to calculate axisymmetric residual of axisymmetric flow variables.
OUTPUT	Routine to print output and save restart files.
PTCALC	Routine to determine inlet total pressure profile.
REFIN	Routine to refine a 3D solution.
REFIN2	Routine to refine a 2D solution.
REFIN3	Routine to refine a reduced domain 3D solution.
RESID	Implicit residual smoothing routine.
RESID2	2D implicit residual smoothing routine.

RUNGE	Runge-Kutta flux calculation routine.
RUNGE2	2D Runge-Kutta flux calculation routine.
STEP	Routine to determine time step.
STEP2	Routine to determine time step for 2D solution.
TEST2D	Routine to calculate the axisymmetric average of the residuals of the 3D flowfield.
VOLUX	Routine to calculate an individual cell volume.
VOLUX2	Routine to calculate an individual 2D cell volume.

B.4 Multiple-Block C-Grid Euler Solver Subroutine Description

A list of the multiple-block C-grid 3D Euler solver program subroutines and their functions is given below for reference. A skeleton program flowchart is illustrated in Fig. B.3 for the multiple-block C-grid 3D Euler solvers.

SUBROUTINE	DESCRIPTION
CPRO3D	Main calling routine.
BCI12	Boundary condition routine between block 1 and 2.
BCI13	Boundary condition routine between blocks 1 and 3.
BCI14	Boundary condition routine between blocks 1 and 4.
BCI23	Boundary condition routine between blocks 2 and 3.
BCI25	Boundary condition routine between blocks 2 and 5.
BCI33	Boundary condition routine along C-grid branch cut.
BCI34	Boundary condition routine between blocks 3 and 4.

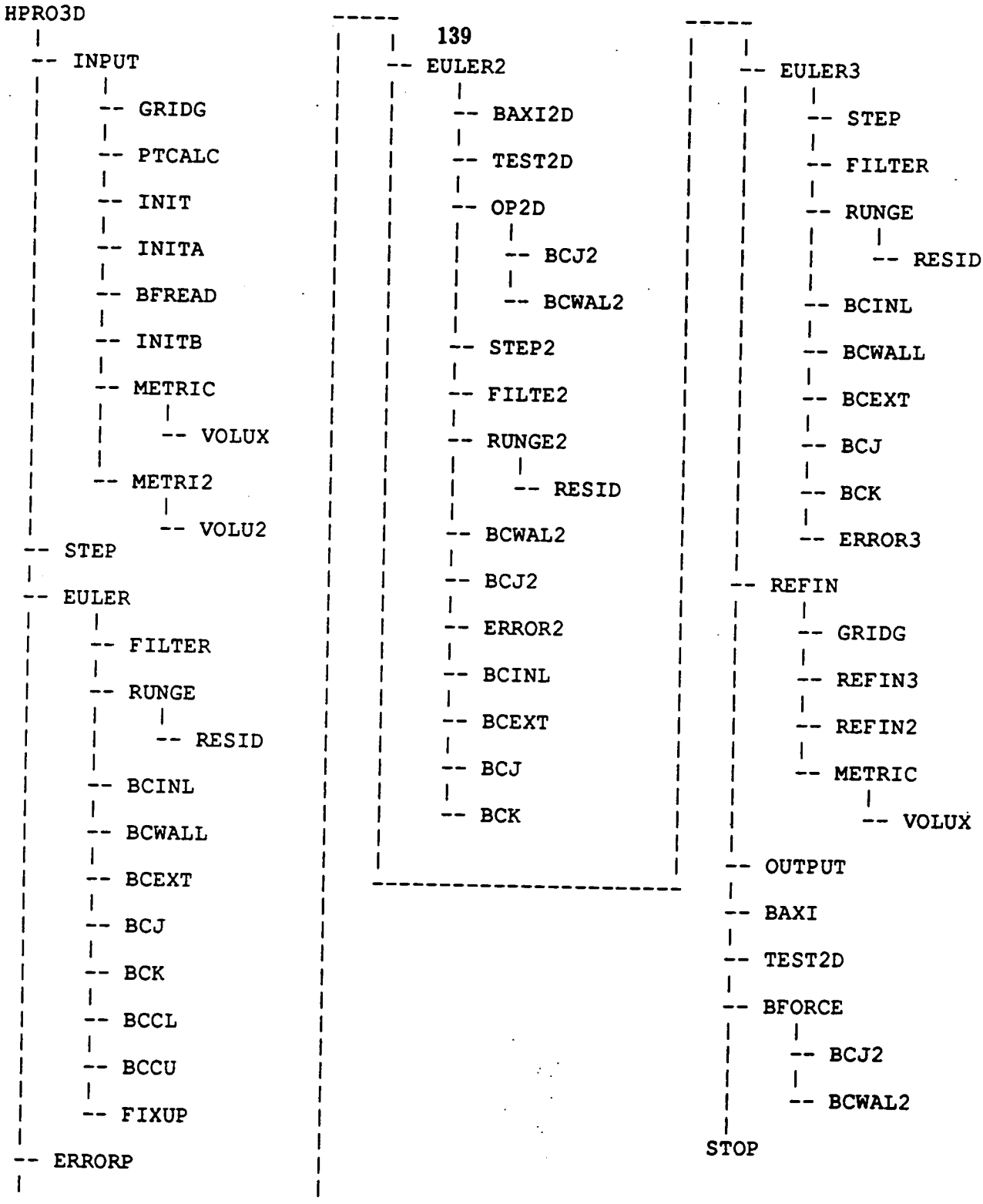

Figure B.2: Program flowchart for ducted propfan analysis H-grid Euler solver

BCI35	Boundary condition routine between blocks 3 and 5.
BCI45	Boundary condition routine between blocks 4 and 5.
BCINL	Boundary condition routine for inlet cells.
BCJ	Boundary condition routine for j=constant surfaces (hub and outer boundaries).
BCK	Boundary condition routine for the blade surfaces.
BCPER	Boundary condition routine for periodic cells.
ERRORP	Convergence-checking routine for Runge-Kutta solver for propfan calculations.
EULER	Runge-Kutta solver.
FILTER	Artificial dissipation routine.
FIXUP	Routine to correct boundary cells before output averaging is performed.
GRIDG	Routine to read and set up the grid.
INIT	Routine to initialize solution.
INPUT	Routine to read in input data and set up reference values.
METRIC	Routine to calculate cell volumes and surface normals.
OUTPUT	Routine to print output and save restart files.
PTCALC	Routine to determine inlet total pressure profile.
REFIN	Routine to refine a 3D solution.
RESID	Implicit residual smoothing routine.
RUNGE	Runge-Kutta flux calculation routine.
STEP	Routine to determine time step.

VOLUX Routine to calculate an individual cell volume.

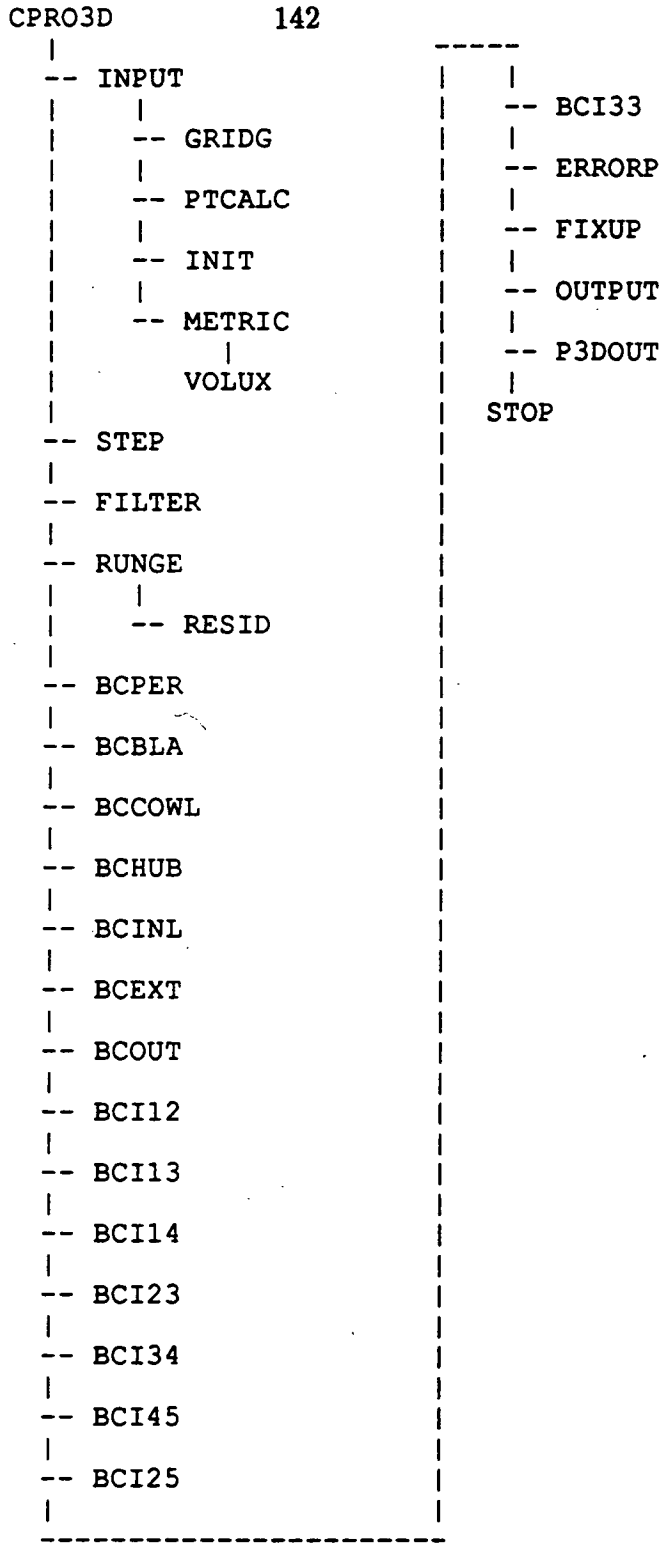

Figure B.3: Program flowchart for ducted propfan analysis multiple-block C-grid Euler solver

NASA
National Aeronautics and Space Administration

Report Documentation Page

1. Report No.	2. Government Accession No.	3. Recipient's Catalog No.
NASA CR-185217		

4. Title and Subtitle

Investigation of Advanced Counterrotation Blade Configuration Concepts for High Speed Turboprop Systems, Task 1--Ducted Propfan Analysis

5. Report Date
April 1990

6. Performing Organization Code

7. Author(s)

Edward J. Hall
Robert A. Delaney
James L. Bettner

8. Performing Organization Report No.
EDR 14622

10. Work Unit No.
505-62-4D

9. Performing Organization Name and Address

Allison Gas Turbine Division of
General Motors Corporation
P.O. Box 420
Indianapolis, IN 46206-0420

11. Contract or Grant No.
NAS3-25270

13. Type of Report and Period Covered
Contractor Report
Final

12. Sponsoring Agency Name and Address

National Aeronautics and Space Administration
Lewis Research Center
Cleveland, OH 44135-3191

14. Sponsoring Agency Code

15. Supplementary Notes

Prepared in cooperation with NASA Project Manager C. J. Miller, NASA Lewis Research Center, Cleveland, OH

16. Abstract This report summarizes the progress of contract NAS3-25270, Task 1--Ducted Propfan Analysis. The time-dependent three-dimensional Euler equations of gas dynamics have been solved numerically to study the steady compressible transonic flow about ducted propfan propulsion systems. Aerodynamic calculations were based on a four-stage Runge-Kutta time-marching finite volume solution technique with added numerical dissipation. An implicit residual smoothing operator was used to aid convergence. Two calculation grids were employed in this study. The first grid utilized an H-type mesh network with a branch cut opening to represent the axisymmetric cowl. The second grid utilized a multiple-block mesh system with a C-type grid about the cowl. The individual blocks were numerically coupled in the Euler solver. Grid systems were generated by a combined algebraic/elliptic algorithm developed specifically for ducted propfans. The Euler analyses were applied for the calculation of both unducted and ducted propfan flows, and predicted results were compared with experimental data for several cases. The three-dimensional Euler analyses displayed exceptional accuracy, although predicted performance was very sensitive to geometric deflections. Both solution schemes were very robust and demonstrated nearly equal efficiency and accuracy, although the multiple-block C-grid formulation provided somewhat better resolution of the cowl leading edge region.

17. Key Words (Suggested by Author(s))	18. Distribution Statement
Turbofans Propfans Ducted propfans Euler	Unclassified-Unlimited

19. Security Classif. (of this report)	20. Security Classif. (of this page)	21. No. of pages	22. Price
Unclassified	Unclassified	159	A08